University of South-Eastern Norway

www.usn.no

FMH606 Master's Thesis 2022

Process Technology

Modeling and simulations of hydrogen flow in a maritime fuel cell system

Stian Valand

Faculty of Technology, Natural sciences and Maritime Sciences
Campus Porsgrunn

University of South-Eastern Norway

www.usn.no

Course: FMH606 Master's Thesis, 2022

Title: Modelling and simulations of hydrogen flow in a maritime fuel cell system

Number of pages: 132, inclusive appendices.

Keywords: Hydrogen, leak, finite difference, fuel gas systems, dynamic modeling.

Student:	Stian Valand
Supervisor:	Knut Vågsæther
	Andre Vagner Gaathaug
	Prasanna Welahettige
External partner:	**Corvus Energy**
	H2NOR

University of South-Eastern Norway

www.usn.no

Summary: The climate change challenge is one of today's greatest challenges, and the need to reduce emissions is more significant than ever. Hydrogen can be a potential zero-carbon fuel, and together with a maritime fuel cell system, there is a great potential to reduce emissions from the maritime sector.

As hydrogen has a very low energy density per volume, there are mainly two ways of utilizing hydrogen as a fuel. Either by liquefying- or by compressing the gas. This study is primarily focused on a compressed gas system. The main aim of this study is to develop a transient numerical model of a fuel cell supply system. But the study will also consider a general literature review on fuel gas supply systems, a simple design proposal of a hydrogen fuel supply system, and a review of equations of state relevant to the numerical model.

There is yet no specific complete framework published covering the design of maritime fuel cell systems. According to DNV, the IGF-Code is the most representable standard to be used as guidelines. The IGF-Code does not consider piping for hydrogen gas, which the standard ASME B31.12 does, however, not from a maritime perspective. Therefore, a simple strength calculation considering the fuel supply pipelines for a "base case" vessel has been performed with both the IGF-Code and the ASME B31.12-2011. The results indicate that the IGF-Code has a more conservative approach for design pressures up to 53 MPa, while ASME B31.12-2011 is found to be the most conservative standard for pressures above 53 MPa.

The one-dimensional dynamic leak flow model has been developed by implementing a finite difference 2^{nd}-order accurate centered FLIC scheme for solving the set of non-linear hyperbolic governing equations. The model considers the effects of friction, minor losses, and heat losses, which are implemented as source terms by source-terms splitting. Modeling of the leakage flow has been performed using isentropic relations and the assumption of sonic flow through the leakage orifice. Two flux limiters, Superbee and Minbee, were implemented. Superbee showed an oscillatory tendency, probably caused by the implemented source terms. The Minbee limiter showed stable behavior but is said to be more diffusive. The simple and well-performing Abel-Noble EOS has been implemented in the model, but the design pressure in this study is 10 bar, and the results from the simulations indicate that the ideal gas law would have been a sufficient choice.

The results obtained from the dynamic leak flow model indicate that the pressure drop from the rarefaction wave is larger downstream of the leak location than the same distance from the leakage location upstream. This is identified to occur due to the implemented source terms in the model. If the ratio between the leak orifice diameter and the pipe diameter exceeds 0.2, the calculated leakage mass flow rate is larger than the calculated inlet mass flow in the pipeline. This is probably possible initially as the pipeline's volume is filled with hydrogen, and the leaking hydrogen can come from both downstream and upstream of the point of leakage. The implemented dynamic leak flow model seems to estimate reasonable results for the pipeline gas flow and leakage.

Preface

This master thesis marks the end of a three-year part-time study in Process Technology at the University of South-Eastern Norway.

I would like to thank my supervisors, Professor Knut Vågsæther, Associate Professor Andre Vagner Gaathaug, and Postdoctoral Fellow Prasanna Welahettige, for your outstanding support and guidance. You have shared your knowledge with enthusiasm, and I really appreciate the hours you have spent on supervising this project.

It has been three challenging years balancing family life as a parent, a full-time job, and part-time studies. This would not have been possible without my amazing, extremely patient, and caring wife taking care of our son Odin while I was studying.

I would also like to thank my parents and my in-laws for their great support and help with the daily tasks at home when I was occupied by my studies.

Askøy, 01.06.2022

Stian Valand

Contents

Nomenclature

A	Cross-sectional area	[m^2]
A_o	Leakage orifice area	[m^2]
a	Wave-speed	[m/s]
b	Abel-Noble co-volume constant	[m^3/kg]
C	Speed of sound	[m/s]
c	Corrosion allowance	[mm]
CFL	Courant-Friedrich-Lewy number	[-]
c_p	Specific heat capacity, constant pressure	[J/ (kg·K)]
CPR	Critical pressure ratio	[-]
c_v	Specific heat capacity, constant volume	[J/ (kg·K)]
D	Diameter	[m]
D_o	Leak orifice diameter	[m]
E	Total Energy	[J]
e	Internal energy	[J/(kg·s)]
f	Darcy-Weisbach friction factor	[-]
F_b	Allowance for bending	[-]
F_d	Design factor	[-]
F_e	Longitudinal joint factor	[-]
F_M	Material performance factor	[-]
F_T	Temperature derating factor	[-]
F_{tol}	Negative manufacturing tolerance	[%]
g	Gravitational constant	[m/s^2]

HHV	Higher heating value	[kJ/kg]
h	Convective heat transfer coefficient	[W/(m^2·K)]
K	Minor losses K-factor	[-]
L	Length	[m]
M	Molecular weight	[kg/mole]
Ma	Mach number	[-]
M_l	Mass flux through leakage	[kg/(m^2·s)]
$\dot{m}$	Mass flow rate	[kg/s]
N	Number of moles in the gas	[mole]
n	Coefficient used for Dittus-Boelter equation	[-]
OD	Outer diameter	[m]
p	Pressure	[Pa]
P	Design pressure	[Pa]
p_a	Atmospheric pressure	[Pa]
p_c	Critical pressure	[Pa]
q	Heat flux	[W/m^2]
q_c	Released heat energy	[W]
q_r	Heat transfer	[W]
R	Specific gas constant	[J/(kg·K)]
R_u	Universal gas constant	[J/(kg·K)]
R_e	Yield strength	[MPa]
R_m	Tensile strength	[MPa]
Re	Reynolds number	[-]
r	Slope strength	[-]

r_{1-3}	Internal pipe radius for a composite system	[m]
r_b	Mean radius of a bend	[mm]
S	Specified minimum yield strength	[MPa]
sf	Safety factor	[-]
T	Temperature	[K]
T_a	Ambient temperature	[K]
T_c	Critical temperature	[K]
T_g	Gas temperature	[K]
T_s	Surface temperature	[K]
t	Time	[s]
t_{w0}	Theoretical minimum wall thickness	[mm]
t_w	Minimum wall thickness	[mm]
U	Overall heat transfer coefficient	[W/(m^2·K)]
u	Velocity	[m/s]
V	Volume	[m^3]
x	Spatial distance	[m]
Z	Compressibility factor	[-]

Greek letters

ρ	Density	[kg/m^3]
γ	The ratio of the specific heats	[-]
μ	Viscosity	[Pa·s]
σ_s	Allowable stress	[MPa]

ϵ	Internal pipe roughness	[-]
τ_n	Shear stress normal to the direction *n*	[Pa]
λ	Thermal conductivity	[W/(m·K)]
ω	Eccentric factor	[-]
η	Efficiency	[-]
Δp	Pressure drop	[Pa]
ΔT	Temperature difference	[K]
Δx	Spatial domain discretization length	[m]
Δt	Time domain discretization length (time step)	[s]

Substances

CO_2	Carbon dioxide
CGH_2	Compressed hydrogen gas
CH_4	Methane
H_2	Hydrogen
LH_2	Liquified Hydrogen
LNG	Liquified natural gas
LPG	Liquified petroleum gas
NO_x	Nitrogen oxides

1 Introduction

The world's average temperature is increasing, and the climate change challenge is one of today's greatest challenges. The last decade, 2010 -2019, was the warmest decade ever recorded, and the concentration of carbon dioxide (CO_2) and other greenhouse gases (GHG) in the atmosphere was at its highest levels ever in 2019 [1]. There is a need for measures to cope with the climate change, and one such measure is the Paris Agreement of 2015, which aims to keep the global average temperature rise well below 2 ℃ through global cooperation [1]. The International Energy Agency (IEA) [2] points out that international cooperation between all governments is of great importance if net-zero emissions are to be achieved by 2050. To accomplish the goal of net-zero emissions, low-emissions fuels instead of fossil fuels are a promising alternative. Of the total emissions from the energy sector, international shipping was responsible for about 2.5% of the total CO_2 emissions in 2020 [2]. In order to reduce emissions, the International Maritime Organization (IMO) started to regulate maritime shipping by adopting policies in 2018. These policies target efficiency improvements for ships and fleets, and the Initial Greenhouse Gas Strategy aims to reduce carbon emissions by 70 % by 2050, compared to 2008 [2].

To reduce the emissions from the maritime sector, alternative and zero-carbon fuels must be considered. Liquified Natural Gas (LNG) is already a mature technology. It has the potential to reduce GHG emissions by up to 23% and nitrogen oxides (NO_x) emissions by up to 80% compared to heavy fuel oil (HFO) [3]. Another possible carbon-free fuel that can reduce emissions significantly is hydrogen (H_2). It is the lightest of all the chemical elements, having an atomic mass of only 1.0079. Hydrogen can be liquified at a temperature of - 253 ℃ and has a higher heating value of 141 800 kJ/kg [4]. Such amount of energy per mass corresponds to approximately 2.5 kg of natural gas, 2.75 kg of oil, or 3.5 - 3.7 kg of coal [4]. Therefore, hydrogen is a promising fuel to replace oil and gas. However, due to the hydrogens' low energy density per volume, one needs large volumes of hydrogen to replace fossil fuels. The density of hydrogen at ambient temperature and pressure is only 0.09 kg/m^3. To increase the density of hydrogen, the gas can either be pressurized or liquified [4]. The utilization of hydrogen as a fuel in the maritime industry, together with a fuel cell system, is a field of increasing attention and investment.

Det Norske Veritas (DNV) [5] points out that hydrogen has some unique properties. Being the lightest of all atoms makes it challenging to contain without any leakages, and its relatively high speed of sound leads to larger leak flow rates. Hydrogen can embrittle materials that would have been safe to use with LNG, and there is a considerable fire hazard due to hydrogen's wide flammability range, which is 4 – 75 % concentration in air at standard conditions [6]. Land-based industries and transport, submarines, and the space industry have utilized H_2 for several years, but the experience and competence with hydrogen in the maritime sector are limited [6]. According to DNV's Handbook for hydrogen-fueled vessels, a higher level of safety requirements must be considered when land-based technology shall be applied for maritime use [6].

The properties of H_2 make it a challenging fuel regarding safety. Therefore, research on how to design and operate an H_2-based fuel gas system in a safe matter is an important field of work. A hydrogen gas leak could have severe consequences for a maritime vessel.

Fuel cells for maritime vessels have been demonstrated since the early 2000s [7]. The world's first liquified hydrogen-powered ferry was the MF Hydra, engineered by LMG Marin AS and drifted by the Norwegian ferry company Norled [8]. There are several ongoing projects on maritime fuel cells. One of them is the H2NOR project [9], a collaboration between Corvus Energy, Equinor, Norled, Wilhelmsen, LMG Marin, NCE Maritime CleanTech cluster, and the University of South-Eastern Norway (USN). The project is led and coordinated by Corvus Energy. It aims to develop and produce modularized and cost-effective Proton Exchange Membrane Fuel Cells (PEMFC) with Fuel cells delivered from Toyota. The fuel cell system is planned to be modularized, marine certified and commercialized from 2024 [9]. The fuel cell system received its *"Approval in Principle"* in April 2022 [10].

This study is made as a part of the H2NOR project. The research group belonging to USN is in the progress of building a physical pipe leak flow model of a maritime fuel cell supply system. An understanding of hydrogen's behavior due to a leak or change in demand is needed for improved piping design and safety measures. The main objective of this study is to develop a one-dimensional transient numerical model of the physical model for simulating the flow behavior of hydrogen gas and the effects of a possible leak in a hydrogen fuel cell supply system.

1.1 Objective

The objectives of this study are defined as follows:

- Literature review of maritime fuel gas systems, with the main focus on fuel storage and supply systems that can possibly be adapted for a maritime fuel cell system.
- A design of a fuel supply system that includes a schematic diagram of a maritime fuel cell system.
- Develop a transient one-dimensional pipe flow model that shall consider the effects of a sudden leak in the system.
- A literature review of relevant Equations of State for the hydrogen pipeline flow.

1.2 Scope

The report will be divided into two separate parts, but the main aim of this study is to develop a one-dimensional transient leak flow model.

The first part will consider a general literature review of maritime fuel gas systems, focusing on the fuel supply systems which can possibly be adapted for a maritime fuel cell system with hydrogen as a maritime fuel. The literature review will be limited to mainly considering fuel storage and fuel pipelines, and considerations for the design of pipelines carrying hydrogen. A design proposal of a simplified compressed hydrogen fuel gas supply system will be performed. The design will contain a simple pipe strength calculation by following two available standards for hydrogen pipelines and a comparison of the results between the two

standards. The proposed hydrogen fuel supply system design will be visualized with a simplified P&ID, including schematics covering the fuel supply from the storage tank to the fuel cell module.

The second part will cover the development of a transient one-dimensional dynamic leak flow model. The main aim of the dynamic leak flow model is to model the physical model that is in the progress of being built at the USN and simulate the flow of hydrogen gas in the fuel cell supply pipeline. The model should be able to simulate the effects that occur to the hydrogen flow from a leak in the pipeline. In particular, the model should be able to capture the rarefaction waves that occur from the leakage. The model shall also consider natural effects that will occur in a pipeline, e.g., friction. Part two will start with a literature review covering the most known Equations of State and some of the previous work regarding equations of state with hydrogen as the fluid. Then relevant theory for pipe flow, pipe leakage, and finite difference methods will be presented. The literature review in the second part will make the basis for choosing the equation of state for the one-dimensional model.

1.3 Outline of the report

As mentioned in the scope, the report will be divided into two separate parts.

Chapter 2 – Part One:

Chapter 2.1 contains the general literature review performed on maritime fuel gas systems.

Chapter 2.2 covers the relevant theory for designing hydrogen fuel pipelines, a pipe strength calculation, and a suggested P&ID for a hydrogen fuel supply system for a maritime fuel cell system.

Chapter 2.3 summarizes and commenting the work performed in chapters 2.1 and 2.2.

Chapter 3 - Part Two:

Chapter 3.1 contains the literature review on relevant equations of state for the dynamic leak flow model to be developed.

Chapter 3.2 gives an overview of the relevant theory used to develop the model.

Chapter 3.3 covers the relevant theory of finite difference methods and introduces the finite difference schemes used to develop the dynamic leak flow model.

Chapter 3.4 describes the development of the dynamic leak flow model.

Chapter 3.5 contains a validation of the developed model.

Chapter 3.6 presents the results and findings from the simulations obtained by the dynamic leak flow model.

Chapter 3.7 discusses the results and addresses the identified uncertainties with the model.

Chapter 3.8 contains the conclusion of Part Two.

2 Part One

Part one of this study will cover a general literature review on maritime fuel gas systems with a focus on published work on fuel supply systems, with the aim of presenting general theory of systems that possibly can be adapted for a maritime fuel cell system. A simple pipe strength calculation of a hydrogen fuel supply system and a comparison of the results between the IGF-Code and the ASME B31.12-2011 will be performed. Further, a simplified process and instrumentation diagram (P&ID) for a hydrogen fuel supply piping system will be proposed.

2.1 Maritime fuel gas systems, literature Review

In principle, there are two kinds of fuel gas systems: liquified fuel gas- and compressed fuel gas systems. This section will briefly introduce the most relevant standards and guidelines for hydrogen storage and pipeline systems, liquified fuel gas- and compressed fuel gas systems, and a brief introduction to energy conversion systems.

2.1.1 Applicable standards and guidelines for hydrogen as a fuel

This section will briefly introduce the most relevant standards and guidelines for designing hydrogen fuel supply storage- and pipeline systems.

No complete framework has been published regarding hydrogen storage and pipelines for a maritime fuel cell system. However, since hydrogen has been used for industrial purposes for a long time, different standards have been established that regulate the application of hydrogen as a fuel in the land-based industry and transport sector. For maritime applications, the standards published by the American Society of Mechanical Engineering (ASME) and the American Petroleum Institute (API) are commonly utilized. The ASME B31.12 covers hydrogen piping and material combability. ASME B31.12 is an example of a standard that, according to DNV, can be used as guidelines for designing the hydrogen piping for Fuel Cell supply systems [6].

According to DNV [6], the International Code of Safety for Ship Using Gases or Other Low-flashpoint Fuels (IGF – Code) is the main international code applicable to hydrogen-fueled vessels. These vessels shall comply with the convention Safety Of Life At Sea (SOLAS) of 1974, which regulates the minimum safety standards for ship construction, equipment, and operation [11]. The IGF-code is applicable for cargo ships with a gross tonnage of 500 or more and passenger vessels on international voyages using low-flash point fuels with flash points less than 60℃. Hydrogen is in a gaseous state at ambient conditions, meaning that it does not have a designated flash point, and will flash for all temperatures above its boiling point at 20 K [12].

The Asia Industrial Gases Association (AIGA) [13] is a non-profit society promoting safety, health, environmental awareness, and security for the industry in Asia. They have published AIGA 033/14, which considers Hydrogen Pipeline Systems, and might possibly be transferrable to a maritime system. The publication is a product of the International Harmonization Council, which is a collaboration between AIGA, Compressed Gas

Association (CGA), European Industrial Gases Association (EIGA), and the Japanese Industrial and Medical Gases Association (JIMGA). The publication is intended for worldwide use and is based on the available technical information and experience [13].

For compressed hydrogen storage, there are no specific standards available. DNV [6] suggests complying with either DNV Rules for Ships Pt.4 Ch.7 or Pt.5 Ch.8, which addresses the rules for pressure vessels and the rules for compressed natural gas (CNG) ships. Special considerations must be evaluated due to hydrogen's special properties.

2.1.2 Liquified fuel supply systems

Liquified petroleum gas (LPG), which mainly consists of butane and propane, has been identified by DNV and Maschinenfabrik Augsburg-Nürnberg AG (MAN) [14] as an attractive energy source. According to DNV [14], this is primarily due to its shorter payback periods, lower investment costs, and less sensibility to changes in the fuel price marked. It is expected that LPG can reduce NO_x emissions by 10-20 % compared to heavy fuel oil (HFO). LPG will also reduce the emissions of particulate matter and black carbon emissions. In order to reach the net-zero emission target, LPG has been identified as a bridging fuel to ammonia, which is considered a green fuel. The materials and systems built for LPG will, in most cases, be suitable for ammonia. However, some adjustments may be necessary when converting from LPG to ammonia [14].

According to DNV [3], LNG is considered a mature fuel option in the maritime industry. However, challenges in finding and developing the most efficient use of the fuel tank systems and engine types still exist. LNG consists mainly of methane (CH_4), which is liquified at temperatures lower than -163℃. With only one carbon atom per molecule, methane is the hydrocarbon fuel with the lowest carbon content. Therefore, the use of LNG has the potential to reduce CO_2 emissions by 26 % compared to HFO [15].

Gu et al. [16] performed a study on a design of a low-pressure gas supply system for a dual-fuel engine. The gas supply system considers the transportation and gasification process of liquified natural gas (LNG) from the storage tank to the dual-fuel engine. Dual-fuel engines are designed to handle both natural gas (NG) and diesel. The natural gas is supplied with a small amount of diesel during the gas mode for better ignition. A typical gas supply system for LNG includes a gasifier, buffer tanks, and piping. For high-pressure systems, pumps must be included. Gu et al. [16] initially calculated and designed the fuel gas supply system by calculation and programming in Python. Then physical experiments were performed on a Wartsila model W6L20DF dual-fuel engine to verify the system's performance and reliability. The results indicate that the fuel supply system was able to deliver a stable supply of natural gas even if the load was varied. The authors suggest evaluating cases of pure methane as the NG when evaluating the heat transfer area in the gasifier. If the mole fraction of methane increases, the heat exchange area also increases due to methane's relatively large specific heat capacity, increasing the potential heat transfer. This heat exchange area will then also apply to NG with a low methane content. The fluid often used for heat exchange in the gasifier is ethylene glycol aqueous solution as a coolant. This substance is chosen due to its high specific heat capacity, low risk, and non-solidification properties at 0℃. The buffer tank's volume is affected by the mass flow rate of NG, and the volume will increase as the

mass flow rate increases. Gu et al. [16] suggest that the buffer tank should be determined according to a maximum expected NG flow as it is found that a change in the mass flow rate has a greater impact on the tank's volume than a change in the pressure.

Nerheim et al. [17] performed a study addressing the advantages and disadvantages of both liquified hydrogen (LH_2) and LNG, and the similarities between the two substances are discussed. The work is based on available data in the literature on various properties of hydrogen, LNG, and methane. The authors point out difficulties in finding reliable data on hydrogen and LNG and state that the study will contribute to making such data and references available. According to Nerheim et al. [17], a typical LNG low-pressure fuel system can be designed as in figure 2.1

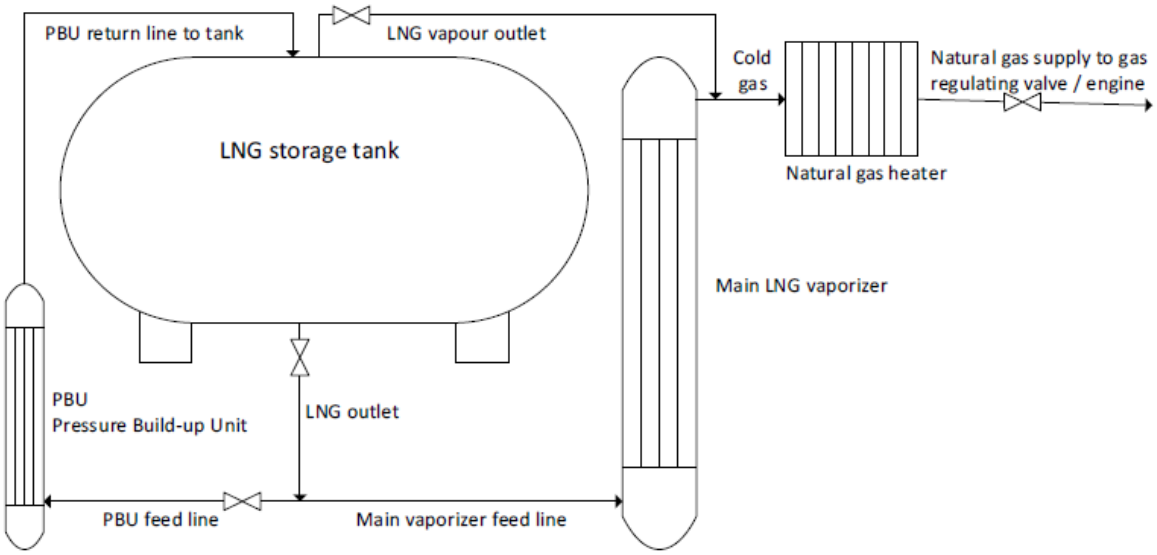

Figure 2.1: A typical LNG fuel supply system [17]

The system in figure 2.1 shows the main components of a typical LNG fuel system. The main components include an LNG storage tank, an LNG vaporizer, an NG heater, regulating valves, and a Pressure Build-up unit designed for pressures below 10 bar. The study's authors [17] point out several challenges with hydrogen as a maritime fuel. Hydrogen can be in a liquid state at -253℃, and LNG is liquified at - 163℃. Since hydrogen has a lower temperature than LNG when liquified, an increased challenge with storage and boil-off needs to be considered. Another challenge is hydrogen's small molecules which increase the risk of leakages. Some possible measures to deal with the identified challenges might be double piping, inert gas systems and ventilation, detectors, and safety procedures. Nerheim et al. [17] conclude that the main challenges with the LH_2 are maintaining sufficient low temperature, safety implications regarding the location of the storage tank, material-, system-, and design requirements for the piping and process equipment. The authors are also questioning the feasibility of LH_2 as a maritime fuel and suggest that the total cost of an LH2 system is probably higher than for an LNG system.

2.1.2.1 LNG Tanks:

According to Chorowski et al. [18], there are two main types of LNG tanks, integral tanks part of the hull structure or self-supporting tanks independent of the hull. The integral tanks consist of a thin membrane layer supported through insulation by the adjacent hull. A common way of constructing membrane tanks is with a primary membrane and a secondary membrane, as shown in figure 2.2 [19]. Such integral tanks usually have a relatively low maximum allowable working pressure, which is 0.25 – 0.7 barg depending on the hull structure design. The internal membrane tanks benefit because they effectively utilize the ship's available volume and offer a large storage capacity for LNG in the range of 100 – 20 000 m^3.

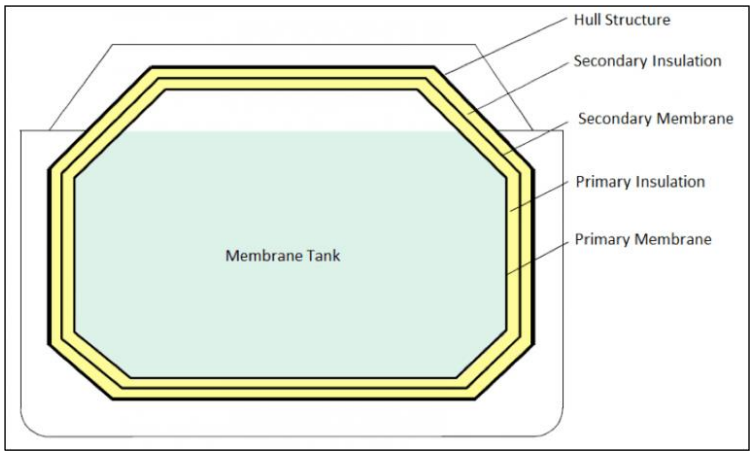

Figure 2.2: Membrane tank with primary and secondary membrane [19]

The hull-independent self-supporting tanks can be divided into A-, B- and C-type tanks.

A-type: An A-type tank is designed by classical ship-structural analysis. The risk of cracks and fatigue in the material leads to the requirement of a secondary barrier. The maximal allowable working pressure is the same as for integral tanks, and due to the design procedure, it is possible to fit the tank to the hull structure [18]. An A-type tank is shown in figure 2.3, where the spaces between the hull are used as the second barrier [19].

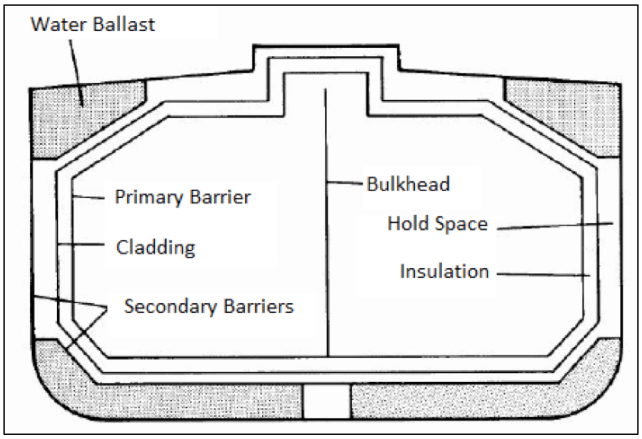

Figure 2.3: A-type tank with secondary barrier [19]

B-type: These tanks are designed using more comprehensive methods such as model tests and analytical tools to determine and predict the stress levels, fatigue life, and the characteristics of eventual crack propagation. Due to more extensive performance testing, only a partial secondary barrier is required, which can be in the form of a drip tray underneath the tank. The pressure range is the same as the A-type tanks [18]. Figure 2.4 illustrates a common B-type tank, the Kvaerner-Moss Spherical Tank, with a drip tray for leak detection [19].

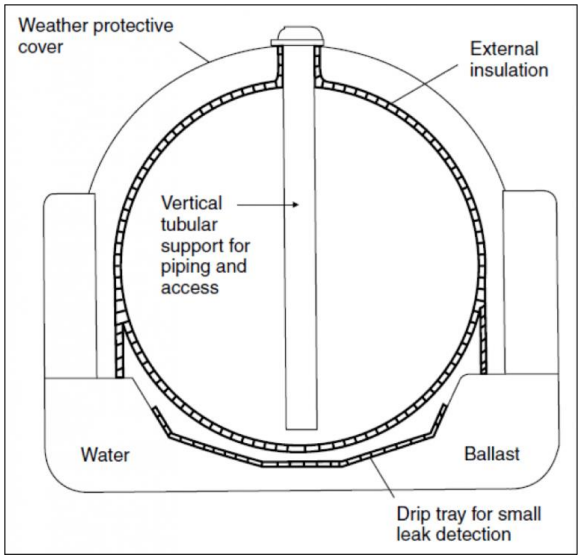

Figure 2.4: B-type Kvaerner-Moss Spherical Tank, with drip tray as a secondary barrier [19].

C-type: These tanks are independent of the hull, and due to higher working pressure, they are considered pressure vessels. The tanks are normally cylindrical in shape, but various shapes on the cross-section are seen on implemented tanks. Chorowski et al. [18] point out that a disadvantage of such tanks is the limited storage volume. The main advantage is that this kind of tank can be installed on already existing ships as a modification project from fossil fuels to fuel gas systems. Figure 2.5 shows a C-tank with two cylinders, considered as pressure vessels [19].

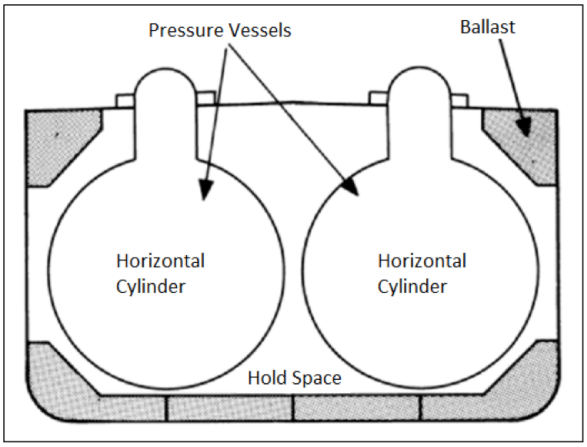

Figure 2.5: C-tank consisting of two cylinders regarded as pressure vessels [19].

2.1.2.2 Liquid Hydrogen (LH_2)

Figure 2.6 shows a schematic of a "below deck" liquified hydrogen fuel cell system. According to DNV [6], an LH_2 fuel supply system for a maritime fuel cell consists of a cryogenic storage tank with a suitable ventilation system. Fuel lines from the tank through a vaporizer and a pressure regulator unit (PRU) that regulates the pressure to an inlet pressure of about 3.5 bar. The PRU can be a pressure-built-up unit, a conditioning tank, or a pump. As shown in figure 2.6, there is also a need for large ventilation systems, both for the pressure relief and fuel supply system. The ventilation shall be able to continuously replace the air in the space surrounding the storage tank and fuel supply lines. In addition, there is a need for safety measures like fire protection and leak detection, and auxiliary systems. For bunkering the storage tanks, helium may be used to purge and pre-cool the tank and supply pipelines [6].

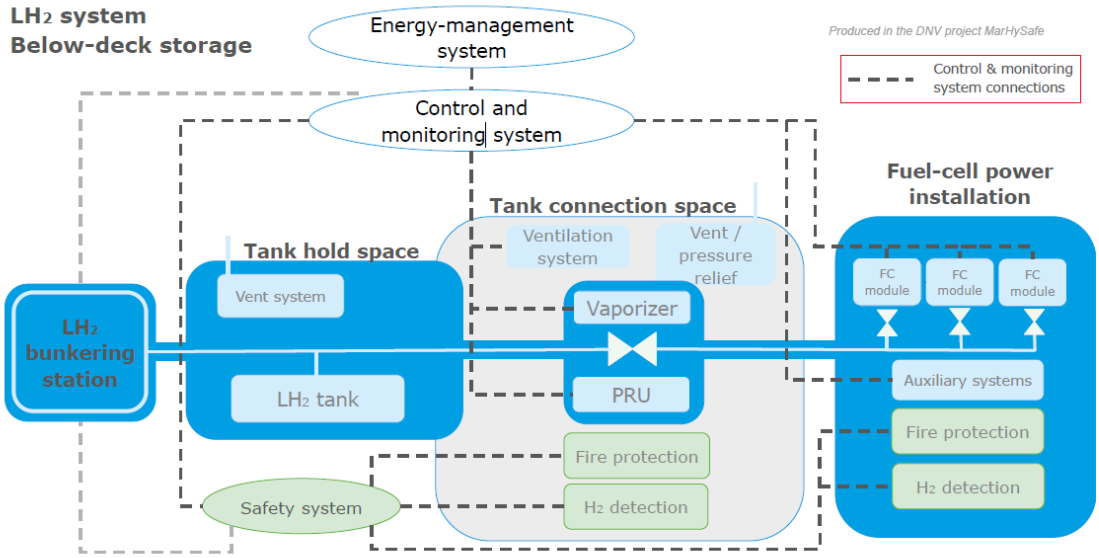

Figure 2.6: Schematic of a "below deck" liquified hydrogen fuel cell system [6]

2.1.3 Compressed fuel gas systems

While LPG and LNG are well-established fuel supply systems in the maritime industry, compressed natural gas (CNG) has primarily been focused on implementing as fuel in land-based vehicles, where CNG can be used as a replacement for petrol, diesel, and LPG [20].

A limited amount of literature is published on maritime compressed gas fuel systems. Standards like the IGF-Code give guidelines on designing such systems, but liquified fuel gas systems seem to be more widely used in the maritime sector.

2.1.3.1 Compressed hydrogen gas (CGH_2)

Compressed hydrogen gas (CGH_2) is often used as a fuel in fuel cell electric vehicles (FCEV), with the benefit of reducing emissions significantly. CGH_2 has a high energy content by mass but low energy content per volume [21]. In the maritime industry, CGH_2 was first introduced

as a fuel in 2000 by the German-made fuel cell driven vessel Hydra. Another well-known vessel utilizing CGH_2 is the Energy Observer, which is supposed to be self-sufficient with energy [22] [17].

A compressed hydrogen fuel gas system is in some ways considered easier to handle than LH_2. This is due to hydrogen's very low temperature in a liquid state, the risk of evaporation, and the challenge of maintaining the required temperature. But a significant fire and explosion risk is a major challenge with pressurized hydrogen systems. Compressed hydrogen is normally pressurized to 350 or 700bar for land-based systems [21]. Such pressures will induce very large leak flow rates. Compared to methane in gaseous form, DNV [6] points out four of the most important factors where CGH_2 is considered a higher risk fuel than methane. These are hydrogen's large flammability range, low ignition energy, shorter burning distances needed to initiate deflagration to detonation transition, and higher explosion pressures. Another drawback with compressed hydrogen is the required storage space due to its low volumetric energy density. The necessary fuel storage space is 10-15 times higher than conventional marine fuel oils. Therefore Xing et al. [23] suggest that CGH_2 is not ideal as fuel for long-distance shipping.

Figure 2.7 show a schematic of a compressed hydrogen fuel cell system. According to DNV [6], the normal pressure based on current marine certifications of CGH_2 storage tanks is 250 bar. The fuel supply system consists of a bunkering system, storage tanks, pressure regulating units, ventilation and pressure relief systems, and the fuel cell modules. Bunkering is based on land-based filling stations, and filling from trucks is currently considered the most promising method [6]. In addition, there is a need for control and monitoring systems, safety measures systems for fire protection and leak detection, and auxiliary systems. The ventilation must handle the pressure relief systems and continuously replace the air in the tank storage space.

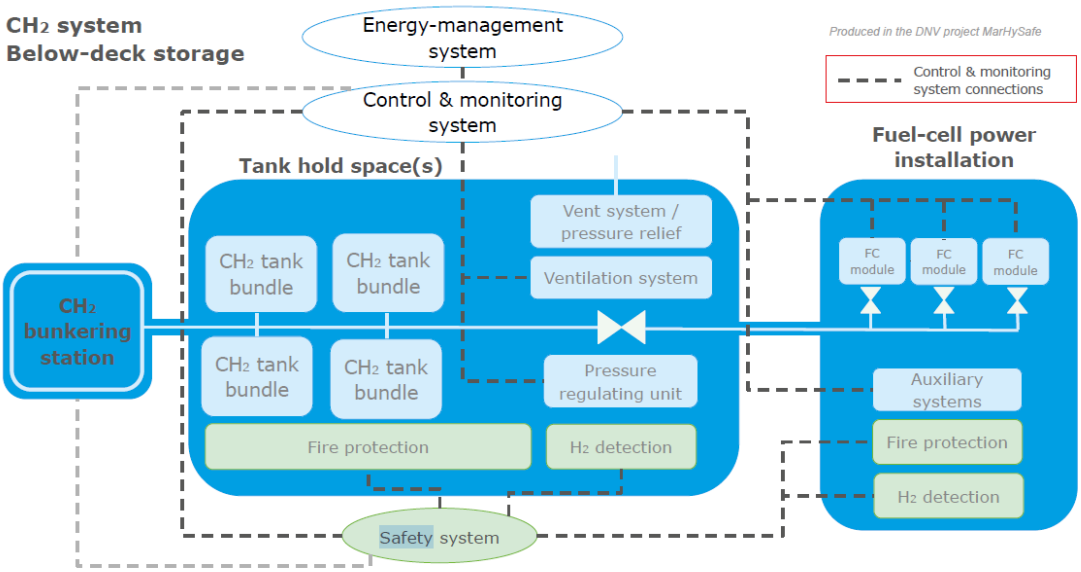

Figure 2.7: Compressed hydrogen gas system for a maritime "below deck" maritime fuel cell [6]

For the design of hydrogen-carrying pipelines intended for maritime use, DNV suggests, amongst others, that the ASME B31.12 and the IGF-code can be used as guidelines [6].

Regarding CGH_2 storage, DNV suggests two different storage systems: steel cylinders and composite cylinders. For choosing the material of the cylinder, the following needs to be considered [6]:

- The steel must not react with the hydrogen, leading to hydrogen embrittlement.
- The permeability of hydrogen
- Other gases in the hydrogen or possible contaminants can affect the corrosion of the steel.

Considering the CGH_2 composite cylinder, the following has to be considered when choosing materials [6]:

- The material must not react to hydrogen. This is due to the risk of increased aging of the material.
- The permeability of hydrogen
- Liner material suitable for hydrogen, and properties as manufactured including fatigue safety.

2.1.4 Energy conversion – Fuel Cells

For both natural gas and hydrogen, there are various ways to utilize the potential energy from the fuel. Gas- and dual-fuel engines and gas turbines are commercially available and the most common method for natural gas systems [17]. Gas turbines and combustion engines will run on hydrogen as well, but while these options are under consideration, fuel cells are the preferred and primary energy converter when considering hydrogen [15].

There are several different types of fuel cells available, like the proton exchange membrane fuel cell (PEMFC), phosphoric acid fuel cell (PACFC), molten carbonate fuel cell (MCFC), and solid oxide fuel cell (SOFC) [24]. According to Nerheim et al. [17], the main differences between the fuel cell types are the type of electrolyte, the ion transporting charge in the cell, and the fuel composition. A brief overview of a choice of the existing fuel cell technologies is listed in table 2.1 [17].

Table 2.1: Fuel Cell technologies and properties [17]

Abbreviation	**Fuel Cell Technology**	**Fuel**	**Operating Temp (℃)**	**Operating Pressure range of H_2**	**Efficiency (%)**
PEMFC	Proton exchange Membrane Fuel Cell	H_2 (g)	50 - 70	1 – 4 atm	40 -60
PAFC	Phosphoric Acid Fuel Cell	H_2 (g)	160 - 220	0 – 4 atm	35 - 45
MCFC	Molten Carbonate Fuel Cell	Pure H_2 or hydrogen-rich fluid	650	1 – 2 bar	45 - 60
SOFC	Solid Oxide Fuel Cell	Pure H_2 or hydrogen-rich fluid	600 – 900	1 – 8 bar	45 -55

2.2 Design of a fuel supply pipeline system

2.2.1 Theory for piping design

The heat release from the combustion of a gas can be found by:

$$q_c = \dot{m} \cdot HHV \tag{2.1}$$

Where q_c is the heat release, $\dot{m}$ is the mass flow rate, and HHV is the higher heating value.

50% of the released heat is assumed to be converted to energy in the fuel cell; the mass flow rate can then be calculated as follows with equation (2.2):

$$\dot{m} = \frac{q_c}{HHV \cdot \eta} \tag{2.2}$$

Where η denotes the efficiency.

The general expression for the mass flow rate is expressed in equation (2.3).

$$\dot{m} = \rho \cdot A \cdot u \tag{2.3}$$

Where u is the gas velocity, A is the cross-sectional area of the pipe, and ρ is the density which can be expressed by the ideal gas law:

$$\rho = \frac{p}{M \cdot R_u \cdot T} \tag{2.4}$$

Where M is the molecular weight of hydrogen and R_u is the universal gas constant, T is the gas temperature, and p is the pressure of the gas. For hydrogen, the specific gas constant, R, is 4.124 kJ/kg·K.

Noting that $A = \frac{\pi}{4} D^2$, the necessary internal pipe diameter, D, can then be found by utilizing equations (2.2) and (2.3), together with (2.4):

$$D = \sqrt{\frac{4 \cdot \dot{m} \cdot R \cdot T}{P \cdot u \cdot \pi}} \tag{2.5}$$

There will be four pipe branches from the main pipe that leads to each FC cabinet. All the cabinets are of equal size and consume an equal amount of energy. Then the mass conservation can be written as equation (2.6), assuming there is no change in accumulated mass with time:

$$\dot{m}_{main} = \dot{m}_{b1} + \dot{m}_{b2} + \dot{m}_{b3} + \dot{m}_{b4} = 4\dot{m}_{b1-4} \tag{2.6}$$

Rearranging gives:

$$\dot{m}_{b1-4} = \frac{\dot{m}_{main}}{4} \tag{2.7}$$

2.2.1.1 Metal properties

When considering the properties of metals, yield- and tensile strength are standard parameters. Yield strength is the stress where the deformation of the material shifts from

elastic to plastic. It can be defined as "… *the greatest stress achievable without any deviation from the proportionality of stress and strain"* [25]. The tensile strength, often called the ultimate tensile strength, indicates the maximum tensile load a material can withstand before necking occurs and the material fractures [25].

Figure 2.8 shows the stress vs. strain curve for a material. The elastic zone is the linear part of the graph, and beyond the point marked with yield strength, the deformation is plastic. The plastic deformation continues until the stress reaches the ultimate tensile strength, and then the deformation will reach failure [25].

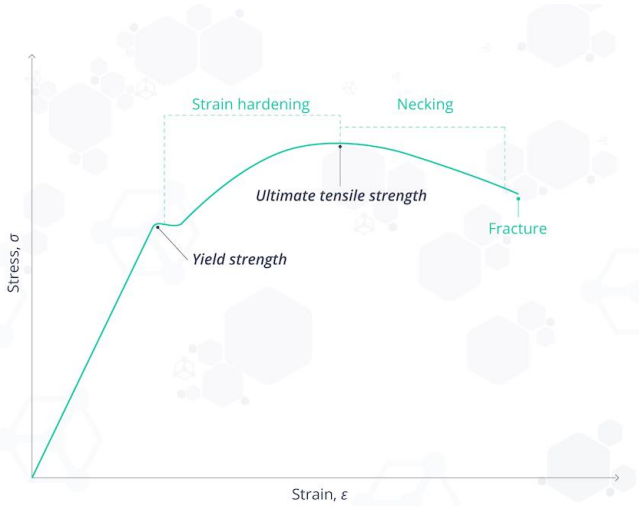

Figure 2.8: Stress vs. strain curve [25]

DNV operates with values for 0.2 % and 1 % yield strength. This refers to what is known as the proof stress (or offset stress), which is the amount of stress a material can withstand until a marginal amount of plastic deformation has occurred [25]. Figure 2.9 shows how the 0.2 % proof stress is measured, which is simply by drawing a line parallel to the linear elastic curve at 0.2% strain. The point of interception is defined as the proof stress [25]. It defines the yield strength where the stress-strain curve doesn't show a defined yield stress [26].

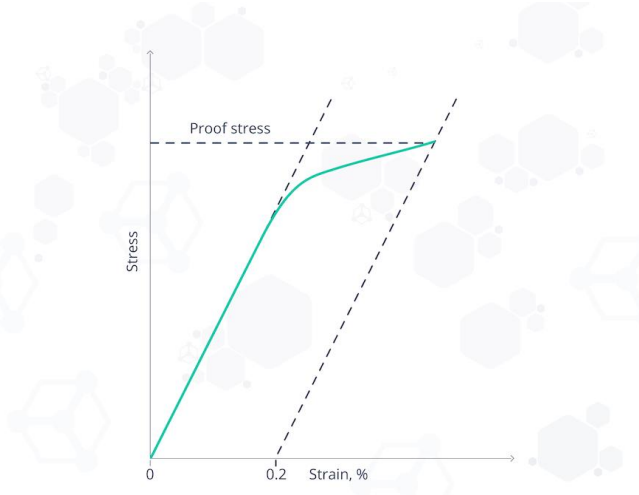

Figure 2.9: 0.2% proof stress, stress vs. strain curve

2.2.1.2 Degradation mechanisms, Hydrogen

According to the Asia Industrial Gases Association (AIGA) [13], pipelines transferring hydrogen gas are susceptible to degradation mechanisms that can occur due to the hydrogen's properties. Hydrogen embrittlement (HGE) is a general term for the degradation mechanisms that can occur from ambient temperatures up to about 200 °C and depends on the type and properties of the metal, environment, and mechanical loading. The mechanism of HGE can be described as a process where the diatomic hydrogen (H_2) is dissociated to monoatomic hydrogen (H). This enables the possibility of hydrogen being absorbed and diffused through the interstitial spacings in the metal. HGE can lead to embrittlement of the metal, enable crack propagation, and weaken the metal's strength properties significantly with only a small amount of hydrogen present in the metal [27]. Therefore, the type of material is an important choice when designing pipelines for hydrogen gas.

Hard steels are more affected by HGE compared to weaker steels. Therefore, steel with a maximum hardness of approximately 22 HRC (Hardness Rockwell C) or 250 HB (Hardness Brinell), which is roughly equivalent to a tensile strength of 800 MPa, should be chosen. In addition, the content of sulfur and phosphorus in the metal shall not exceed 0.01% and 0.015%, respectively [13].

2.2.1.3 Piping connections

Welding is the preferred method for connections on pipelines due to hydrogen's small molecules [13]. The welded zone often becomes harder than the material, and therefore a lower strength welding material should be used. Preferably with a tensile strength of about 500 MPa. Another method of avoiding the harder material from the weld procedure is performing special welding procedures, including thermal treatment and pre- or post-welding. The second-best method for pipe connections is by flanges and gaskets. This should be used if welded connections are found to be impractical. Then, a raised face, tongue and groove, or ring-joint flanges should be used with a proper gasket. The gasket material must be appropriate for the work pressure, hydrogen compatible, and fire-resistant in case of a leakage. Threaded connections are the third option connections. These should only be used where the two alternatives above are not applicable. Typically, a threaded connection will be used to connect instruments like manometers to the piping system [13].

2.2.1.4 Double-walled piping

For a double-walled pipe system, both the inner and outer stress needs to be considered during a pipe stress analysis. In addition, the inner and outer pipe expansion and the fixed support between the inner and outer pipe must be considered during the stress analysis [6].

The space between the inner and outer pipe shall be pressurized with an inert gas with a higher pressure than the inner pipe. The double-wall piping needs a support welded between the inner and outer pipe as a carrier to stabilize the inner pipe, and a possible design is shown in figure 2.10.

Figure 2.10: Possible design of double-walled pipe with carrier [28].

2.2.1.5 ASME B31.12-2011, minimal wall thickness calculation procedure

The ASME B31.12-2011 [29] recommends the following equation for calculations of the minimum wall thickness:

$$P = \frac{2 \cdot S \cdot t_w}{OD} \cdot F_d \cdot F_e \cdot F_T \cdot F_M \tag{2.8}$$

Rearranging gives:

$$t_w = \frac{P \cdot OD}{2 \cdot S \cdot F_d \cdot F_e \cdot F_T \cdot F_M} \tag{2.9}$$

Where:

OD = Outside diameter of the pipe

F_e = Longitudinal joint factor. Tabulated in ASME B31.12

F_d = Design factor.

P = Internal design pressure

S = Specified minimum yield strength.

t_w = Calculated minimum wall thickness

F_M = Material performance factor. Tabulated in ASME B31.12

F_T = Temperature derating factor

2.2.1.6 IGF-code, minimal wall thickness calculation procedure

The IGF-Code gives the following procedure for calculating the minimal wall thickness, t_w, for the piping:

$$t_w = \frac{\left(t_{w_0} + F_b + c\right)}{\left(1 - \frac{F_{tol}}{100}\right)} \tag{2.10}$$

$$t_{w_0} = \frac{P \cdot OD}{\left(2.0 \cdot \sigma_s \cdot F_{eff} + P\right)} \tag{2.11}$$

$$F_b = \frac{OD \cdot t_{w_0}}{2.5 \cdot r_b} \tag{2.12}$$

t_{w_0} = Theoretical wall thickness in mm.

P = Design pressure, in MPa

OD = Outside diameter

σ_s = Allowable stress, N/mm^2

F_{eff} = Efficiency factor. Equal to 1 for seamless pipes and longitudinally spirally welded pipes delivered by approved manufacturers.

F_b = Allowance for bending

r_b = Mean radius of the bend, mm

c = Corrosion allowance, mm

F_{tol} = Negative manufacturing tolerance, %.

The allowable stress shall be the lower of the two values $\frac{R_m}{2.7}$ or $\frac{R_e}{1.8}$, where R_m denotes the tensile strength and R_e denotes the yield strength (0.2% proof stress) [26].

2.2.2 Design of piping

For this design proposal, guidelines from both the IGF-code and the ASME B31.12-2011 will be followed. According to DNV, the IGF-Code is the primary framework when evaluating FC systems. However, the IGF-code does not consider the effect of hydrogen's properties. Therefore, the ASME B31.12-2011 Hydrogen Piping and Pipelines will be followed when evaluating the necessary strength, and the results will be checked with the guidelines from the IGF-code.

The piping network is divided into a main feed section from the storage tank. The main feed is split into four branches (b1-4), each leading to its respective FC cabinet. Each branch is then split into four sub-branches (sb1-4) at the FC cabinet, leading to each FC module.

Calculations considering the main feed pipe will be shown, while the calculations for the branches and sub-branches can be viewed in Appendix B.

The pipeline design is based on a "base case" vessel with the following assumed parameters as tabulated in table 2.2:

Table 2.2: Design parameters for the base case vessel

Parameter	Value	Unit
Total fuel cell effect, base case vessel	1280	[kW]
Effect, one PEMFC module	80	[kW]
Number of modules per fuel cell cabinet	4	[-]
Number of FC cabinets in total	4	[-]
Fuel	CGH_2	[-]
HHV H_2	141 800	[kJ/kg]
Efficiency Fuel Cell	50	[%]
Inlet design gas velocity	30	[m/s]
Max work pressure	10	[bar]
Gas Temperature	20	[℃]

Limitations: This system design will focus on the piping carrying hydrogen from the storage tank to the fuel cell modules. Pressure drop and friction effects in the pipeline will be neglected. Necessary valves will be included in the P&ID drawing but will not be investigated any further regarding strength and properties. The design will not include piping for other systems like oxygen, exhaust, and other auxiliary systems like cooling.

For the main feed pipe from the storage tank and a gas velocity equal to 30 m/s, equation (2.2) and (2.5) gives:

$$\dot{m}_{main} = \frac{q_c}{HHV \cdot \eta} = \frac{1280\ kW}{141\,800\ kJ/kg \cdot 0.5} = 0.01805\ kg/s$$

$$D_{main} = \sqrt{\frac{4 \cdot 0.01805\ kg/s\ \cdot\ 4124\ J/kgK\ \cdot 293.15\ K}{10\ \cdot 10^5\ Pa\ \cdot 30\frac{m}{s} \cdot \pi}} = 0.0304\ m = 30.4\ mm$$

The calculated necessary diameter for the main feed pipeline is 30.4 mm with the design gas velocity from table 2.2.

If a smaller inner piping diameter is preferred, an increased design gas velocity can be chosen. In figure 2.11, the necessary inner pipe diameter for the main feed pipe and the branches are plotted with increasing velocity utilizing equations (2.1 – 2.7). The design parameters from table 2.2 have been used as a basis, with the design gas velocity as the only variable.

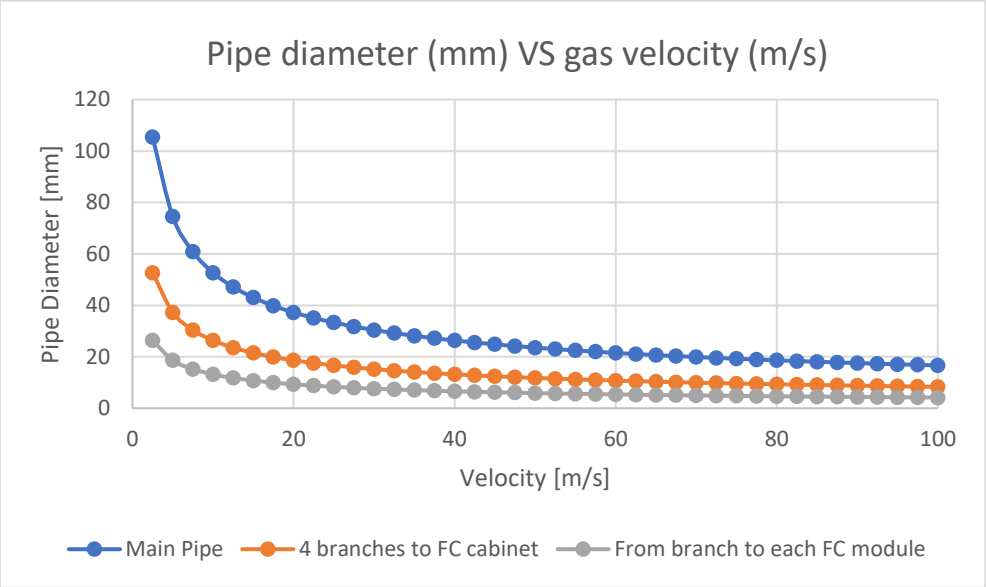

Figure 2.11: Necessary inner pipe diameter plotted vs. gas velocity utilizing equation (2.1 – 2.7).

The selected design piping has to withstand the selected design pressure as a minimum, which in this case is 10 bar. According to the IGF-Code, the minimal design pressure shall be 10 bar for a low-pressure system [26].

Various materials can be chosen for hydrogen pipelines. ASME B31.12-2011 lists what to consider when selecting materials and what materials to avoid. The list is mainly covering metals. Another material to the piping as a replacement for steel could have been to choose fiber-reinforced polymer (FRP). It has the benefit of lower installation costs and the possibility of having longer pipe elements leading to fewer joints [30]. The temperature and pressure in this study are considered low, and the temperature will likely range from 20 - 60℃ due to the nature of PEMFC, as seen in table 2.1. In this case, austenitic stainless steel will be considered for further calculations.

With different materials, different risks need to be evaluated. When choosing stainless steel for hydrogen purposes, one has according to ASME B31.12-2011, to consider three main factors [29]:

- There is a risk of stress corrosion cracking for austenitic stainless steels if exposed to chlorides and other halides, both internally and externally.
- If austenitic stainless steel is exposed to temperatures between 427 – 871 ℃, intergranular corrosion can occur.
- The brittleness of ferritic stainless steel at room temperature, which has been exposed to temperatures above 371 ℃ during service.

In DNV-RU-SHIP Pt.2 Ch.1 to Ch.4, using materials with either a VL certificate or W certificate is advised. These certificates indicate that the manufacturer and the manufacturing process are approved [31]. DNV-RU-SHIP Pt.2 Ch.2 provides rules and guidelines regarding metallic materials. For this case, the austenitic stainless steel, VL316L, is chosen as the material in accordance with DNV's rules for ship classification [31].

VL 316 L has the following properties and composition as tabulated in table 2.3.

Table 2.3: Metal properties for the selected steel VL 316 L [31]

Grade	Tensile strength (N/mm^2)	Minimum Yield strength (N/mm^2), 0.2%	Minimum Yield strength (N/mm^2), 1.0%
VL 316 L	450 – 700	195	235

ASME B31.12-2011 is a quite old standard, updated in 2014 and 2019. The version from 2011 is the only version found available online for free. According to ASME's website, the equations for wall thickness have been updated. However, the version from 2011 is the only standard found that particularly targets hydrogen as a fuel. Therefore, the wall thickness equations from ASME B31.12-2011 will be considered in this study. The results will also be compared with the equations for the wall-thickness given by the IGF-Code. The pipe strength calculations will be shown for the main supply pipe, while calculations for the pipe branches can be viewed in Appendix B.

For the given design gas velocity of 30 m/s, the selected standard dimensions are tabulated in table 2.4.

Table 2.4: Selected design values for the main feed pipe based on ASME/ANSI B 36.10 Welded and Seamless Wrought Steel Pipe and ASME/ANSI B36.19 Stainless Steel Pipe [29].

Section	Calculated Inner diameter (mm)	Corresponding std. pipe dimensions (inches)	Schedule	Wall thickness (mm)	Outer Diameter (mm)	Inner diameter (mm)
Main feed pipe	30.4 mm	1	5S	1.651	42.164	32.462

The values from table 2.4 are utilized for the pipe strength calculations. The required minimum wall thickness is calculated with equation (2.9) following the ASME B31.12-2011 and with the equations (2.10 – 2.12) following the IGF-Code. The schedule in table 2.4 denotes the standard of the thickness of the pipe for a given outer diameter.

The different factors necessary for pipe strength calculations are tabulated in table B1.2 in Appendix B, and the required pipe thickness can be calculated following ASME B31.12-2011 and equation (2.9):

$$t_{w_{main,min}} = \frac{P \cdot OD}{2 \cdot S \cdot F_d \cdot F_e \cdot F_T \cdot F_M} = \frac{1.0\ MPa \cdot 42.164mm}{2 \cdot 195\ MPa \cdot 0.5 \cdot 1.0 \cdot 1.0 \cdot 1.0} = 0.216\text{mm}$$

As can be observed from the calculation, the necessary wall thickness for the feed pipeline with a design pressure of 10 bar is 0.216mm. This is without a corrosion allowance included.

ASME B31.12-2011 suggests using 0.5mm as corrosion allowance to the steel resulting in a minimum wall thickness of 0.716 mm for the main feed pipeline.

The IGF-Code [26] states that the fuel supply system can be designed as gas-safe- or electrostatic discharge (ESD) – protected machinery spaces. For this study, a gas-safe machinery space will be considered. Then the gas pipes must be completely enclosed by either a double-walled pipe or a duct, and the piping joints, branches, and connections shall be fully welded, inspected, and radiographed.

For the double-wall piping, 11 bar will for simplicity be assumed and regarded as the inert gas pressure for this study. Table 2.5 summarizes the selected outer piping for the main feed pipe based on standard dimensions and the selected inner piping from table 2.4.

Table 2.5: Outer pipe dimensions for the main feed pipe based on ASME/ANSI B 36.10 Welded and Seamless Wrought Steel Pipe and ASME/ANSI B36.19 Stainless Steel Pipe [32].

Section	Outer Diameter (mm) Inner pipe	Outer diameter, outer pipe (mm)	Inner diameter, outer pipe (mm)	Schedule	Wall thickness Outer pipe (mm)	Nominal diameter, Outer pipe (inches)
Main feed pipe	42.164	60.325	57.023	5S	1.651	2

Check if the design pipe has sufficient minimum wall-thickness with equation (2.9):

$$t_{w_{outer,main,min}} = \frac{P \cdot OD}{2 \cdot S \cdot F_d \cdot F_e \cdot F_T \cdot F_M} = \frac{1.1\ MPa \cdot 60.325\ mm}{2 \cdot 195\ MPa \cdot 0.5 \cdot 1.0 \cdot 1.0 \cdot 1.0} = 0.340\text{mm}$$

Considering the corrosion allowance of 0.5 mm, $tw_{outer,main,min} = 0.840\ mm$

The results indicate that the minimum wall thickness is less than the design thickness, meaning that the main feed pipe has sufficient strength for the working pressure.

2.2.3 IGF-Code design

By following the IGF code for calculating the thickness, the following calculated results are achieved:

$$\frac{R_m}{2.7} = \frac{450\ MPa}{2.7} = 166.67\ MPa$$

$$\frac{R_e}{1.8} = \frac{195\ MPa}{1.8} = 108.33\ MPa$$

The lowest value shall be chosen, therefore $\frac{R_e}{1.8} = 108.33\ MPa = \sigma_s$.

2.2.3.1 Inner piping:

Assuming $F_{eff} = 1$.

$$t_{w0,main} = \frac{P \cdot OD}{\left(2.0 \cdot \sigma_s \cdot F_{eff} + P\right)} = \frac{1.0\ MPa \cdot 42.164\ mm}{(2.0 \cdot 1 \cdot 108.33\ MPa + 1.0\ MPa)} = 0.194\ mm$$

The bend radius, r_b, is assumed to be $2 \cdot OD$, a standard method used in the industry [33].

$$F_{b_{main}} = \frac{OD \cdot t_{w0}}{2.5 \cdot r_b} = \frac{42.164\ mm \cdot 0.194\ mm}{2.5 \cdot 2 \cdot 42.164\ mm} = 0.039\ mm$$

The corrosion allowance is assumed to be 0.5 mm, and a negative manufacturing tolerance of 12.5% [29].

$$t_{w_{main,min,IGF}} = \frac{\left(t_{w0} + F_b + c\right)}{\left(1 - \frac{F_{tol}}{100}\right)} = \frac{(0.194 + 0.039 + 0.5)}{\left(1 - \frac{12.5}{100}\right)} = 0.837\ mm$$

The inner main feed pipe wall thickness is calculated to be 0.837mm following the IGF-Code.

2.2.3.2 Outer piping IGF:

$$t_{w0,main,IGF\ outer} = \frac{P \cdot OD}{(2.0 \cdot \sigma_s \cdot F_e + P)} = \frac{1.1\ MPa \cdot 60.325\ mm}{(2.0 \cdot 1 \cdot 108.33\ MPa + 1.1\ MPa)} = 0.305\ mm$$

$$F_{b_{main,main\ outer}} = \frac{D \cdot tw_0}{2.5 \cdot r_b} = \frac{60.325\ mm \cdot 0.305\ mm}{2.5 \cdot 2 \cdot 60.325\ mm} = 0.061\ mm$$

$$t_{w_{main,min,IGF,outer}} = \frac{(tw_0 + F_b + c)}{\left(1 - \frac{F_{tol}}{100}\right)} = \frac{(0.305 + 0.061 + 0.5)}{\left(1 - \frac{12.5}{100}\right)} = 0.989\ mm$$

The outer main feed pipe minimum wall thickness is calculated to be 0.989mm following the IGF-Code.

2.2.3.3 Calculated minimum wall thickness

The calculated minimum wall thicknesses for the main feed pipe and the branches are tabulated in table 2.6.

Table 2.6: Calculated minimum pipe wall thickness (tw), including results from Appendix B. ASME B31.12-2011 & IGF - Code

Pipe system	Design pipe wall thickness (Inner/Outer)	ASME B31.12, Inner Piping. [mm]	IGF-Code, Inner Piping [mm]	ASME B31.12, Outer Piping [mm]	IGF – Code, Outer Piping [mm]
Main feed pipe	1.651/1.651	0.716	0.837	0.840	0.989
Branch 1-4	2.769/1.651	0.609	0.706	0.688	0.803
Sub-branch 1-4	1.245/1.651	0.553	0.636	0.620	0.719

In table 2.6, the results of the calculated minimum wall thickness obtained from the main feed pipe and the branches by following ASME B31.12-2011 and the IGF-Code are tabulated. The outer main feed pipe is identified with the smallest ratios between the design- and calculated wall thicknesses. The following calculations show the safety factor (*sf*) with respect to the wall thickness:

$$sf_{main,ASME,outer} = \frac{t_{w_{design}}}{t_{w_{calculated}}} = \frac{1.651}{0.840} = 1.97$$

$$sf_{main,IGF,outer} = \frac{t_{w_{design}}}{t_{w_{calculated}}} = \frac{1.651}{0.989} = 1.67$$

The results from the pipe strength calculations in table 2.6 and the *sf* calculations indicate that the IGF-Code is the most conservative option regarding pipe wall thickness for the given design pressure. Branch 1-4 is identified as the piping with the largest ratio between the design- and calculated wall-thickness, with a ratio of 4.55.

If the minimum wall-thickness calculations for both ASME B31.12-2011 and the IGF-Code are plotted with increasing pressure, then the results indicate that the ASME B31.12-2011 becomes the most conservative approach for higher pressures. From figure 2.12, it can be observed that the steel used for this study's design, VL316L, the IGF-Code is the most conservative standard up to design pressures about 53 MPa, and then ASME B31.12 becomes the most conservative. The discrepancy between the two standards increases with increasing pressure, as shown in figure 2.12.

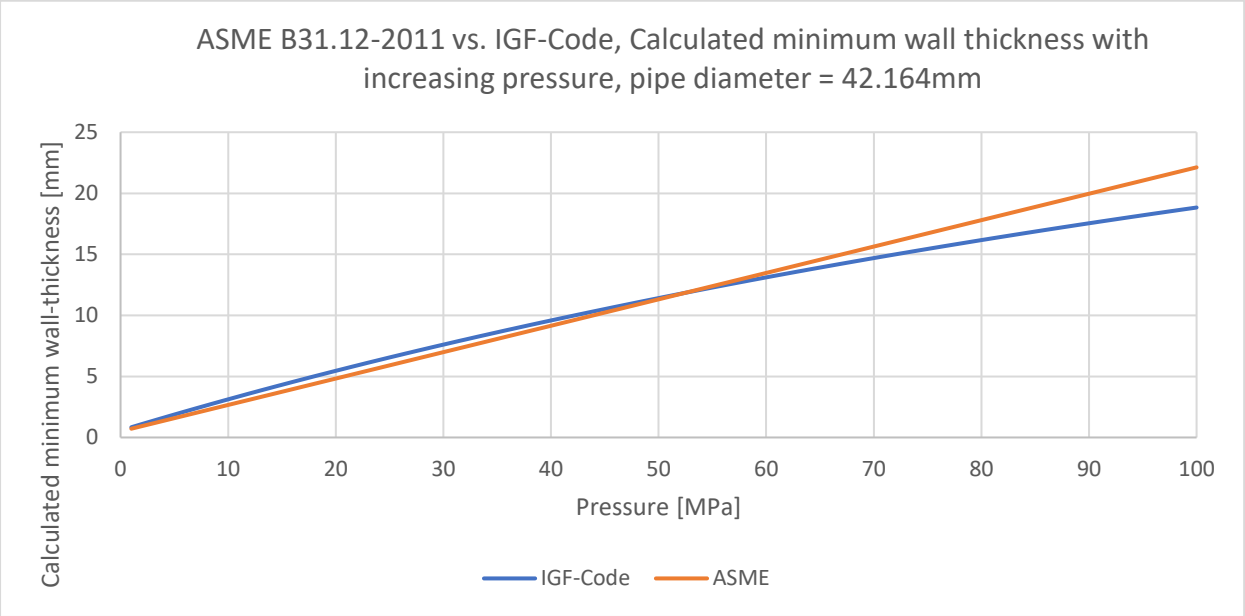

Figure 2.12: Comparison between ASME B31.12-2011 and the IGF-Code with increasing pressure. Outer pipe diameter = 42.164 mm. Material: VL316L, stainless steel, yield strength = 195 MPa.

2.2.4 Valves

According to the IGF-Code [26], valves on the inlet of the main fuel supply line shall be placed as close to the tank as possible. The valve arrangement on the main supply line shall consist of a manually operated stop valve, in series with an automatically operated "master gas fuel valve."

The gas consumers, which in this case are the FC, shall have a valve system called "double block and bleed," which consists of two shut-off valves in series, with a bleed valve between the two shut-off valves [26]. A version of a "double block and bleed valve" is shown in figure 2.13. The "double block and bleed" configuration can either be designed as two separate valves in series or as one unit with three internal valves. The configuration shall be operated remotely or automatically, as it is used for the shutdown procedure of the gas consumer [26]. If the master gas valve is automatically shut, the double block and bleed valve must shut, and the bleed valve shall ventilate the gas line downstream of the double block configuration. In addition, there shall be one manually operated valve mounted on the gas line to ensure the safe isolation of the fuel cell during maintenance [26].

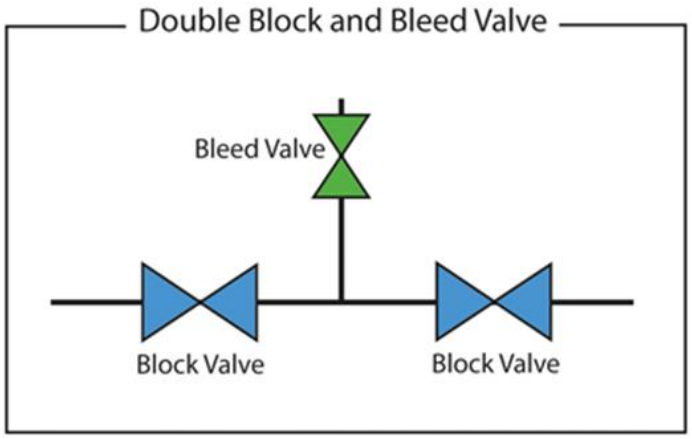

Figure 2.13: Schematic of a Double Block and bleed valve [34]

Pressure relief valves shall be installed to protect the system from excessive pressure. If a pressure relief valve is activated, the gas flow shall be routed to a safe location or open air. In this design, a pressure relief valve will be placed after the reduction valve and before each fuel cell module to protect the FC modules from excessive pressure.

2.2.5 P&ID

The P&ID diagram in figure 2.14 represents a schematic for the suggested design of the base case fuel supply system, as shown in table 2.2. The storage tank is equipped with a pressure relief valve leading to open air. This system's pressure relief and safety valves lead the gas to open air. After the storage tank, there is a manually operated valve, a master fuel gas valve connected electronically to the engine control console (ECC), and an electronically connected pressure regulator to obtain the desired system pressure.

Next in line is the flow regulating valve, which is electronically connected to the ECC and regulates the gas flow based on the necessary power consumption. A safety valve is placed after the flow regulating valve. Then the main feed line is divided into four branches leading to each FC cabinet. Each branch is equipped with a “double block and vent valve” configuration, electronically controlled by the ECC. In addition, an electronically controlled vent valve is installed after the double block and vent configuration to ventilate the gas downstream to the fuel cells.

Each branch has one pressure relief valve mounted to protect the fuel cell modules from excessive pressure. Then each branch is divided into the four sub-branches leading to each fuel cell module, with a manually operated double-valve arrangement. The double-valve arrangement is to be able to isolate one single fuel cell module for maintenance purposes safely. The safety relief valves are connected to the main venting pipe leading to open air.

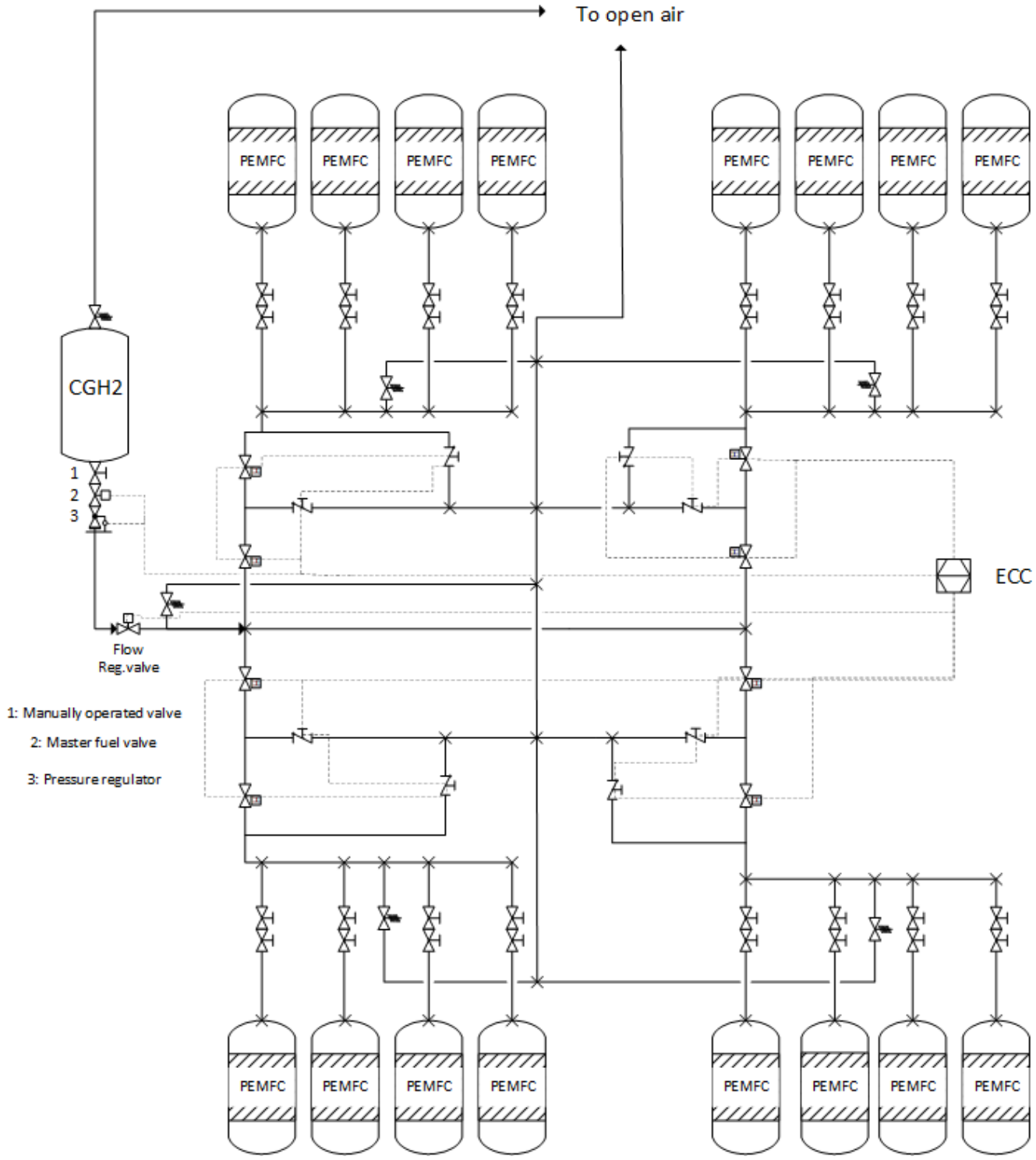

Figure 2.14: P&ID, suggested hydrogen fuel piping for PEMFC

2.3 Summary and comments

A general literature review on maritime fuel gas systems has been performed in this part of the study. Some work is published on LNG and liquified systems, but finding literature that considers compressed fuel gas systems has been a challenge. While LPG and LNG are commonly used for maritime fuel gas systems, LH_2 seems to be a more challenging fuel and may even be too challenging compared to CGH_2. LH_2's extremely low temperature is a disadvantage, possibly leading to CGH_2 as a more attractive fuel for maritime fuel cell systems. However, the fuel storage volume and the safety hazards are challenges that need to be solved when considering CGH_2 as a fuel for maritime vessels.

There is no complete framework published that specifically covers hydrogen-fueled maritime vessels. According to DNV, the IGF-Code is the most suitable standard. However, it does not specifically cover hydrogen. ASME B31.12 covers hydrogen pipelines specifically, but not from a maritime perspective. Therefore, a hydrogen pipeline design has been performed following the guidelines from ASME B31.12-2011 and the IGF-Code.

Standardized dimensions available on the commercial market were used as a basis for the design of piping dimensions. The selected piping was the nearest option in the chosen selection to fit the necessary diameter for the design gas velocity. The design has not been optimized in regards of finding the best fit possible. As seen in figure 2.11, the pipe diameter increases as the gas velocity increases. If a higher design gas velocity is accepted for the pipeline system, another pipe with a smaller diameter could have been chosen. This would have led to less steel weight and probably reduced costs, which are factors that need to be evaluated in a total maritime pipeline design.

The pipe dimensions were chosen based on the required power consumption for the total fuel cell system and the design gas velocity as tabulated in table 2.2. The required inner diameter for the main feed pipeline was 30.4 mm with the design gas velocity. The nearest fit from standardized dimensions was selected, which led to a design wall thickness of 1.651 mm. Further, the selected piping for the main feed pipeline has an outer diameter of 42.164 mm and 60.325 mm for the inner and outer pipe, respectively. The main feed pipeline has been split into four branches and sub-branches, and an identical calculation procedure is performed in Appendix B, but the results were tabulated in table 2.6. As seen in table 2.6, the calculated minimum wall thickness varies with the piping diameter. The least conservative results for the minimum wall thickness were obtained for the outer main feed pipeline, with $t_w = 0.989$mm calculated with the IGF-code. The most conservative result was obtained for the inner piping for branch 1-4, with $t_w = 0.609$ mm calculated with the ASME B31.12-2011, where the selected design wall thickness for the inner branch 1-4 was 2.769 mm. This is considered too conservative, and an optimization should definitely be performed.

The calculated results with ASME B31.12 and the IGF- Code indicate that the proposed design has sufficient thickness, and parts of the piping design are likely over-dimensioned. Considering the outer piping for the main branch, which has the lowest ratio between the design- and calculated minimum wall thickness, a design pressure calculated with the design wall thickness would correspond to about 3 and 4 MPa for the IGF-Code and ASME B31.12-2011, respectively. This is approximately 3 and 4 times the design pressure and probably more than sufficient.

From table 2.6, it can be observed that the minimal wall thickness calculations based on the IGF-Code give the most conservative results, which indicates that the IGF-Code has a safer calculation method for the design pressure in this study. A conservative approach should often be used as a guideline, as a conservative approach leads to a safer calculation result.

When the minimum wall thickness calculations are plotted with increasing pressure, the ASME B31.12-2011 is identified as the most conservative approach for pressures above 53 MPa. From figure 2.12, it can be observed that an intersection between the two standards is obtained at 53 MPa. This is where the ASME B31.12-2011 starts calculating the largest magnitudes of the minimum wall thickness, leading to the most conservative approach. Some of the reason for this is probably that the design pressure is present in both the numerator and the denominator in equation 2.11 for the IGF-Code. The numerator and denominator are both increasing with increasing pressure, leading to a “flattening” effect of the curve, as shown in figure 2.12. The denominator in the calculations following ASME B31.12-2011 is constant, with the pressure in the numerator as the only variable, leading to a linear relationship. However, the version of ASME B31.12 utilized in this study is from 2011, and the equations have been updated in the newer versions. As the newer versions of ASME B31.12 are not available for free, the differences between the versions have not been investigated.

A P&ID shown in figure 2.14 was presented for a suggested pipeline model from a storage tank to the fuel cell modules. The design is supposed to be in accordance with ASME B31.12-2011 and the IGF-Code regarding fuel supply systems and considers fuel feed lines and the most necessary valves and safety valves. The safety relief valves lead the hydrogen gas to open air, and the vent duct should be placed such that the hydrogen is led away from the vessel. A possibility of isolating every pipeline branch safely with a double valve arrangement in series is implemented. The hydrogen has a very low density and is difficult to contain. If a leak occurs or maintenance is needed, the affected pipeline must be isolated safely without any hydrogen leakage through the valve. A double valve arrangement is assumed to minimize the risk of internal leakage in the valve and is believed to increase the level of safety when operating the system. The valves have not been considered detailed in the matter of the type of valve, strength, and other properties. The main focus on the valves has been their intended function in the system.

3 Part Two

This part will start with a literature review of the relevant equations of state (EOS) for a compressible flow system containing hydrogen. The literature review will have a general overview and then focus on some of the earlier work that has been done involving hydrogen and pipeline flow. The dynamic leak flow model development will start with an overview of the relevant theory, focusing mainly on pipe flow and finite difference methods. Then a description of the implementation procedure, validation with hand calculations, and presentations of the results will follow. Part two will be finalized with a discussion of the implemented model and a conclusion at the end.

3.1 Equation of State literature review

The relation between pressure, volume, and temperature, which is known as the PVT-behavior, was discovered by scientists in the 19th century, and the EOS for an ideal gas can be expressed as:

$$pV = NR_uT \tag{3.1}$$

Where R_u is the universal gas constant, V is the volume of the gas, p is the pressure, N is the number of moles in the gas, and T is the temperature of the gas. The ideal gas law is valid for moderate pressures and temperatures. According to Smith et al. [35], the ideal gas state can be described *as "... the state of a gas comprised of real molecules that have negligible molecular volume and no intermolecular forces at all temperatures and pressures."*

For high pressures, a compressibility factor, Z, can be used as a correction factor to handle the difference in the value of the real gas molar volume and the ideal gas molar volume. The value of Z will vary and have a value less than 1 for low temperatures and a value higher than 1 for high temperatures [35]. Figure 3.1 indicates the effect of higher pressure on the compressibility factor for hydrogen. It is obvious from figure 3.1 that for pressures above 10 MPa, the effect of non-ideality is of significance for the calculation results.

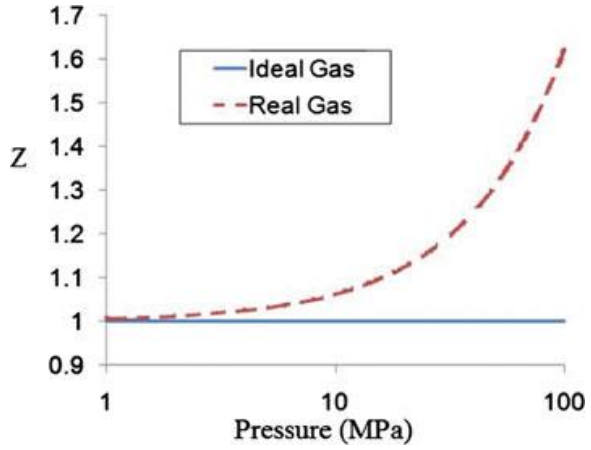

Figure 3.1: Hydrogen compressibility factor at a temperature of 300K [36].

The compressibility factor is defined by equation (3.2), and by considering $Z = 1$ the ideal gas law is obtained.

$$Z \equiv \frac{pV}{NR_uT} \tag{3.2}$$

A method for approximating the value of Z is by viral expansion, where Z can be expressed as follows:

$$Z = 1 + \frac{B}{V} + \frac{C}{V^2} + \frac{D}{V^3} + \cdots \tag{3.3}$$

The parameters B, C, and D are called viral coefficients, and they are dependent on gas temperature only for a given gas. For engineering purposes, it is common to truncate the expansion after the third term [35].

3.1.1 Cubic equations of state:

Cubic equations of state are useful to calculate the states of both liquids and vapors for a wide range of pressures, volumes, and temperatures. The equations are a compromise between being suitable for multiple cases and the simplicity for general use. According to Smith et al. [35], *"the cubic equations are in fact the simplest equations capable of representing both liquid and vapor behavior."*

3.1.1.1 The van der Waals Equation of State

J.D. van der Waals proposed the first practical cubic equation of state in 1873, which can be expressed as:

$$p = \frac{RT}{V-b} - \frac{a}{V^2} \tag{3.4}$$

The purpose of the coefficients a and b, is to account for the intermolecular forces and to handle the finite size of molecules, respectively [35]. If the coefficients are set to zero, the ideal gas law is obtained.

3.1.1.2 Redlich-Kwong equation

The Redlich-Kwong (RK) equation was first introduced in 1949 with the following expression [35]:

$$p = \frac{RT}{V-b} - \frac{a(T)}{(V+b)(V+b)} \tag{3.5}$$

Due to the continuous enhancement of the parameters in equation (3.5), multiple generic cubic equations of state have been developed with equation (3.5) as the basis.

3.1.1.3 Soave Redlich-Kwong (SRK)

The SRK equation of state is a cubic equation of state commonly used for hydrocarbons and gases. It can be applied to cryogenic systems down to -140℃ and pressures up to 35MPa. At the triple-point, it can be challenging to obtain the correct root for the cubic equations [37].

SRK is a further development of the RK-equation (3.5) and was first published in 1972. The equation can be written in a polynomial form as in equation (3.6) [38].

$$Z^3 - (1 - B)Z^2 + (A - B^2 - B)Z - AB = 0 \tag{3.6}$$

Where:

$$A = \frac{a\alpha p}{(RT)^2} \tag{3.7}$$

$$B = \frac{bp}{RT} \tag{3.8}$$

$$a = 0.42747\ \frac{(RT_c)^2}{p_c} \tag{3.9}$$

$$b = 0.08664\ \frac{RT_c}{p_c} \tag{3.10}$$

$$\alpha = \left[1 + (0.480 + \ 1.574\omega - 0.176\omega^2)\left(1 - \sqrt{\frac{T}{T_c}}\right)\right]^2 \tag{3.11}$$

T_c and p_c is the critical temperature and pressure, respectively, and ω is the acentric factor [38]. The acentric factor considers the differences in molecular shape, which increases with non-sphericity and polarity [37]. The acentric factor is defined as shown in equation (3.12) [35]:

$$\omega \ \equiv \ -1.0 - \log(P_r^{sat})_{T_r=0.7} \tag{3.12}$$

3.1.1.4 Peng-Robinson

According to Smith and Smith [37], the Peng-Robinson equation of state is the most popular of the cubic equations of state, and gives a better prediction of liquids' density than the SRK EOS. Smith and Smith [37] also point out that cubic equations of state lack the ability to accurately predict the behavior of mixtures containing a significant amount of hydrogen.

The Peng-Robinson equation of state is similar to the SRK equation of state and can be expressed in the polynomial form [38]:

$$Z^3 - (1 - B)\ Z^2 + (A - B^2 - 2B)Z - (AB - \ B^2 - \ B^3) = 0 \tag{3.13}$$

Where:

$$A = \frac{a\alpha p}{(RT)^2} \tag{3.14}$$

$$B = \frac{bp}{RT} \tag{3.15}$$

$$a = 0.45724\ \frac{(RT_c)^2}{p_c} \tag{3.16}$$

$$b = 0.07780\ \frac{RT_c}{p_c} \tag{3.17}$$

$$\alpha = \left[1 + (0.37464 + 1.5422\omega - 0.26992\omega^2)\left(1 - \sqrt{\frac{T}{T_c}}\right)\right]^2 \tag{3.18}$$

Where ω is equal to equation (3.12).

The Peng-Robinson EOS is used for hydrocarbons and gases with temperatures down to -250°C and pressures up to 1000 bar [37].

3.1.2 Abel-Noble

The Abel-Noble EOS originates from the van der Waals EOS, but this EOS only contains one constant parameter, making it quite simple to implement in a physical problem. The Abel-Noble EOS can be implemented as shown in equation (3.19) [36].

$$p = \frac{\rho RT}{(1 - b\rho)} = (1 - b\rho)^{-1}\rho RT = Z\rho RT \tag{3.19}$$

The correction factor b is approximated as a constant and is supposed to represent the finite volume of the gas molecules. If $b = 0$, the expression for an ideal gas is obtained. Zou et al. [39] suggest a value of the co-volume constant as $b = 0.007691$ [m^3/kg], while Khaksarfard et al. [36] suggest $b = 0.007555$ [m^3/kg].

According to Toro et al. [40], the Abel-Noble EOS is also referred to as the co-volume EOS and is suitable for dense gases at high pressures. The purpose of the co-volume constant is to consider the occurrence when the volume occupied by the molecules is not negligible. From experimental results on a range of solid fuels, it has been observed that b has small and negligible changes. Therefore, it is reasonable to assume and consider b as a constant.

The Abel-Noble performs well for pressures less than 200 MPa and temperatures close to ambient conditions, and its simplicity makes it convenient for general engineering purposes [41].

3.1.3 EOS, Pipe Flow & Hydrogen

The following subchapter will introduce some of the work that has been published on EOS, hydrogen, and pipe flow.

Khaksarfard et al. [36] performed a numerical simulation of a tank's high-pressure release of hydrogen. Due to the high pressures, up to 70 MPa, a real gas model was implemented as the ideal gas assumption cannot be applied to such high pressures. The real-gas EOS implemented was the Beattie-Bridgeman with five constants and Abel-Noble with only one constant. The results show a negligible difference between Beattie-Bridgeman and Abel-Noble, and the Beattie Bridgeman EOS suffers from instability problems. Khaksarfard et al. [36] emphasize that a real gas equation should be used for pressures above 10 MPa.

A study performed by Maciej Chaczykowski [42] has been investigating the pipeline thermal model and non-isothermal, one-dimensional compressible flow in a pipeline. The study includes a detailed thermal model. This has been done by implementing the heat transfer term in the energy equation. The GERG-88 method, which stand for Groupe Européen de Recherches Gaziéres 1988, was implemented as a real gas model. This EOS is commonly used to calculate the compressibility factor of natural gas, assuming that the gas is considered a five-component mixture of hydrogen, carbon monoxide, carbon dioxide, nitrogen, and the sum of hydrocarbon gas. In the model, the compressibility factors are differentiated with respect to time, pressure, and temperature. The derivative terms of the compressibility factor are normally small. A common practice is to use a constant factor or a simple equation as an approximation to save computational time.

In the study performed by Q.Zou et al. [39], a model for high-pressure hydrogen leakage, which includes heat exchange corrections (HEC), has been implemented. The model is named the HEC-model. Various EOS and enthalpy formulas have been investigated for this study. The model excludes the assumption of isentropic conditions for the pressurized gas tank. However, the assumption of isentropic conditions is implemented for the leakage orifice. The model is validated by comparing empirical data and other similar experiments found in the literature. A comparison of the different EOS has been performed where the Soave-Redlich-Kwong and Aungier-Redlich-Kwong EOS shows promising results but are found to be more complicated to implement in a model. Therefore, the Able-Noble EOS was implemented due to its simplicity with only one constant and well performance. A formula based on the Helmholtz free energy has been implemented to calculate the enthalpy. The Helmholtz equation shows promising results when compared to data from the National Institute of Standards and Technology (NIST). The gas tank was modeled with Abel-Noble EOS, but the leakage orifice was modeled with a mass flow formula based on van der Waals EOS and Perry's flow coefficient formula. The model can accurately predict the different states in the system due to the consideration of the heat exchange between the gas and its surroundings and uses more accurate real-gas EOS and enthalpy formulas.

Zhou et al. [43] performed a study on the decompression of a high pressure CO_2, and evaluated the leakage flow through a nozzle in the pipe by a two stage leakage process model. They found that the Span-Wagner (SW) EOS, which employs the Helmholtz free energy, predicted the results more accurately than the Peng Robinson EOS. However, they stated that the Peng Robinson EOS is a compromise between accuracy and dealing with flows with phase changes near the critical point. The SW EOS has a quite complex format and is more computational demanding than the PR EOS.

Alesaadi et al. [44] investigated experimental data obtained from hydrogen adsorption and desorption processes. The state of the hydrogen was modeled with the Sanches-Lacombe Equation of state (SL EOS). The SL EOS can be written as:

$$\overline{\rho^2} + \bar{P} + \bar{T}\left[\ln(1-\bar{\rho}) + \left(1-\frac{1}{r}\right)\bar{\rho}\right] = 0 \tag{3.20}$$

Where $\bar{\rho} = \frac{\rho}{\rho^*}$, $\bar{P} = \frac{P}{P^*}$, $\bar{T} = \frac{T}{T^*}$, and $r = \frac{P^* M}{(R\,T^*\rho^*}$.

The authors [44] investigated the hydrogen adsorption and desorption processes for a wide range of pressures, 0 – 80 bar, and found that the SL EOS gives reasonable results.

Bai-Gang et al. [45] presented a new equation of state for hydrogen gas to investigate the fuel consumption characteristics of hydrogen-fueled vehicles. The proposed equation considers the interaction distance between the hydrogen molecules and is based upon the Van der Waals equation. The proposed equation can be written as:

$$p_r = \frac{T_r}{Z_c(V_r + 0.13636) - \frac{1}{8}} - \frac{\frac{27}{64}}{\sqrt{T_r} Z_c^2 (V_r + 0.13636)^2} \tag{3.21}$$

Where the subscript *r* denotes the reduced properties. They investigated pressures in the range from 0.1 – 70 MPa, and within the temperature range of 48 – 398 K. The results indicate that the calculation of fuel consumption of hydrogen has an error of less than 0.5% compared to available empirical data. The EOS is relatively simple in form and trivial to implement, and the authors claim that the new equation of state can be used to estimate the cruising range of hydrogen-fueled vehicles.

Lemmon et al. [46] have proposed an EOS for calculating the density of hydrogen gas in the temperature range 220 – 440 K and pressures up to 45 MPa. The proposed equation is a truncated virial-type equation made to fit empirical current standard data within 0.01 %. Lemmon et al. emphasize that the equation is only for density calculations within the given temperature and pressure range. The proposed equation gives an uncertainty for the density of 0.2 %, and the results have been compared to experimental data. The virial expression can be written as:

$$z(p,T) = 1 + \sum_{i=2}^{6} \sum_{j=1}^{2} \nu_{ij} \left(\frac{p}{1\ MPa}\right)^{i-1} \left(\frac{T}{100K}\right)^{n_{ij}} \tag{3.22}$$

The constants from equation (3.22) are tabulated in [46]. The authors conclude that the equation shows reasonable and promising results compared to NIST Standard Reference Database data. However, Lemmon et al. state that there might be other uncertainties that haven't been considered in the current study. Such uncertainties could be the suitability of the parahydrogen equation to represent the actual fuel used, temperature and pressure dependence of the tank volume, and other uncertainties in temperature and pressure measurement [46].

Kim et al. [47] performed a study on numerical modeling of the transcritical mixing and reacting flow processes encountered in liquid propellant rocket engines. The non-ideal thermodynamic behavior was modeled using a real-gas equation of state, which was a modified version of the Soave-Redlich-Kwong EOS. The modified SRK EOS was compared to a model with the assumption of ideal gas. The base case chosen for this study was a gaseous hydrogen/cryogenic liquid oxygen (GH_2/LO_x) coaxial jet flame at supercritical pressure. The SRK EOS was chosen due to its accuracy in estimating low carbon fuels and its wide range of thermodynamic conditions. The modified version of the SRK equation can be written as:

$$p = \frac{\rho R_u T}{M_w - b\rho} - \frac{a\alpha\rho^2}{M_w(M_w + b\rho)} \tag{3.23}$$

Where R_u is the universal gas constant, M_w is the molecular weight of the fluid mixture. In order to calculate equation (3.23), the constants: a, α, b, a are determined by universal relationships.

$$a_i = 0.42727 \left(\frac{R_u^2 T_{c,i}^2}{p_{c,i}}\right) \tag{3.24}$$

$$b_i = 0.08664 \left(\frac{R_u T_{c,i}}{p_{c,i}}\right) \tag{3.25}$$

$$a\alpha = \sum_{i=1}^{N}\sum_{j=1}^{N} X_i X_j \sqrt{a_i a_j \alpha_i \alpha_j}\left(1 - \overline{\kappa_{ij}}\right) \tag{3.26}$$

Where $\overline{\kappa_{ij}}$ denotes the binary interaction coefficient and X_i denotes the mole fraction of species i.

$$b = \sum_{i=1}^{N} X_i b_i \tag{3.27}$$

$$\alpha_i = \left[1 + S_i\left(1 - \sqrt{\frac{T}{T_{c,i}}}\right)\right]^2 \tag{3.28}$$

$$S_i = 0.48508 + 1.55171\omega_i - 0.15613\omega_i^2 \tag{3.29}$$

Kim et al. [47] suggest replacing the expression of α_i (3.28) with the following expression:

$$\alpha_{H_2} = 1.202 \exp(-0.30228 T_c) \tag{3.30}$$

This replacement is performed if the fluid has a very low critical temperature, as is the case with hydrogen ($T_c = 33\ K$). The authors claim that this replacement is more accurate when the reduced temperature of hydrogen is higher than 2.5 (T > 83 K). When the replacement expression (3.30) is used for hydrogen, the binary interaction coefficient $\overline{\kappa_{ij}}$ is also set to zero. The authors conclude in their study that the real-fluid-based flamelet model is performing well, and realistic predictions of the characteristics of a turbulent non-premixed GH_2/LO_x flame at supercritical pressures are obtained.

3.2 Pipe flow theory

The continuity equation can be defined as [42]:

$$\frac{\partial \rho}{\partial t} + \frac{\partial (\rho u)}{\partial x} = 0 \tag{3.31}$$

Where $\frac{\partial \rho}{\partial t}$ represents the change in mass over time, ρ represents the mass density, and $\frac{\partial (\rho u)}{\partial x}$ represents the change in the mass flux in and out of the control volume where u denotes the velocity [48].

$$\frac{\partial (\rho u)}{\partial t} + \frac{\partial (p + \rho u^2)}{\partial x} = -\frac{f \rho |u| u}{2D} - \rho g \sin \alpha \tag{3.32}$$

The momentum equation (3.32) is derived from Newton's second law of motion and represents the transient force balance within the control volume. The equation's left-hand side (LHS) represents the change of mass times acceleration in time and space. The term $\frac{\partial p}{\partial x}$ on the LHS represents the net force introduced by the pressure gradient. The right-hand side (RHS) term - $\frac{f \rho |u| u}{2D}$ represents the frictional force acting on the fluid in the opposite direction of the velocity. The RHS term $\rho g \sin \alpha$ represents the gravity force due to the incline of the piping, where g is the gravitational constant and α is the angle between the horizontal plane and the pipeline, as illustrated in figure 3.2.

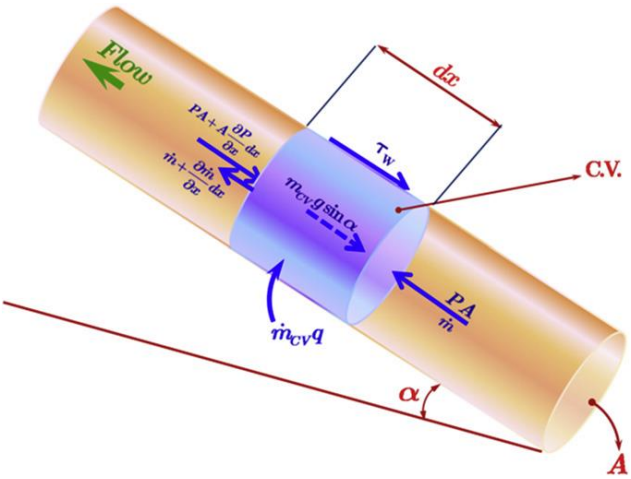

Figure 3.2: Inclined gas pipeline with control volume [49]

The model will include multiple 90 degrees elbows in series. This leads to the necessity of an extra added term to the momentum equation due to the irregularities in the geometry. In this case, a total bend loss factor, K_t, is applied, and the following additional term for considering the Δp must be added to the RHS in the momentum equation [50]:

$$\Delta p = -\frac{K_t u^2 \rho}{2} \tag{3.33}$$

Where K_t is a constant based on the piping geometry and empirical data from pressure loss experiments. The subscript t denotes the total amount of bends in the system.

The momentum equation then becomes:

$$\frac{\partial(\rho u)}{\partial t} + \frac{\partial(p + \rho u^2)}{\partial x} = -\frac{f\rho|u|u}{2D} - \frac{K_t u^2 \rho}{2} - \rho g \sin\alpha \tag{3.34}$$

$$\frac{\partial E}{\partial t} + \frac{\partial[(E+p)u]}{\partial x} = -\frac{4q}{D} - \frac{2f\rho u^3}{D} \tag{3.35}$$

The energy equation can be expressed as shown in equation (3.35), where the LHS term $\frac{\partial E}{\partial t}$ represents the change in the total energy, E, over time [43]. The second term on the LHS, $\frac{\partial[(E+p)u]}{\partial x}$, represents the change in the total energy flux. The first term on the RHS, $\frac{4q}{D}$, represents the heat transfer due to either heating or cooling depending on the gas- and the ambient temperature. q is the heat transfer flux, and the multiplier term $\frac{4}{D}$ is due to the ratio of the inside pipe surface area to the internal pipe volume, $\frac{4}{D} = \frac{\pi D}{(\pi D^2/4)}$. The second term on the RHS, $\frac{2f\rho u^3}{D}$, is representing the frictional heat work from the pipe gas flow [48].

The Mach number, Ma, is the ratio between the fluid velocity and the speed of sound for the fluid and is defined as:

$$Ma = \frac{u}{C} \tag{3.36}$$

C denotes the speed of sound in the fluid, and for an ideal gas, C can be expressed as:

$$C = \sqrt{\gamma\left(\frac{R}{M}\right)T} = \sqrt{\frac{\gamma p}{\rho}} \tag{3.37}$$

M is the molar mass of the gas, and γ is the ratio of the specific heats with constant pressure and constant volume, which is expressed by equation (3.40) for a calorically ideal gas.

$$\gamma = \frac{c_p}{c_v} \tag{3.38}$$

Assuming that the enthalpy is a function of temperature and pressure, $h = h(T, p)$, specific heat capacity for constant pressure can be expressed as:

$$c_p = \left(\frac{\partial h}{\partial T}\right)_p \tag{3.39}$$

A similar expression can be obtained for the specific heat capacity for constant volume:

$$c_v = \left(\frac{\partial e}{\partial T}\right)_v \tag{3.40}$$

Where e denotes the specific internal energy.

Utilizing that $c_p - c_v = R$ for an ideal gas, and equation (3.38), the following relationships can be expressed:

$$c_p = \frac{\gamma R}{\gamma - 1}, \qquad c_v = \frac{R}{\gamma - 1} \tag{3.41}$$

This can further be derived to the following expression for the specific internal energy [40]:

$$e = \frac{p}{(\gamma - 1)\rho} \tag{3.42}$$

Then the total energy can be expressed as in equation (3.43):

$$E = \frac{1}{2}\rho u + \rho e \tag{3.43}$$

Implementing the Abel-Noble co-volume EOS, equation (3.42) becomes:

$$e_{Abel-Noble} = \frac{p(1 - b\rho)}{\rho(\gamma - 1)} \tag{3.44}$$

Likewise, the caloric co-volume EOS for the speed of sound can be expressed with equation (3.45):

$$C_{Abel-Noble} = \sqrt{\frac{\gamma p}{(1 - b\rho)\rho}} \tag{3.45}$$

And the total energy can be expressed as:

$$E_{Abel-Noble} = \frac{1}{2}\rho u + \frac{p(1 - b\rho)}{(\gamma - 1)} \tag{3.46}$$

3.2.1 Friction factor

The friction factor is a dimensionless number that considers the effect of friction between the pipe wall and the fluid. Correlations based on empirical data are the most common method to calculate the friction factor, and one of the most known empirical correlations is the Colebrook-White correlation [38]. The Colebrook-White equation is widely used in the industry and serves as the basis for the well-known Moody diagram [51].

The Colebrook-White equation is written as:

$$\frac{1}{\sqrt{f}} = -2\log\left(\frac{\epsilon}{3.7D} + \frac{2.51}{Re\sqrt{f}}\right) \tag{3.47}$$

Where f denote the Darcy-Weisbach friction factor, ϵ is the internal roughness of the pipe wall, D is the internal diameter of the pipe, and Re is the Reynolds number. The internal roughness of the pipe can be found in tables based on empirical data [4].

The Reynolds number is a dimensionless number discovered after Osborne Reynolds' flow visualization experiments in 1883 and is commonly used to define whether the fluid flow is

turbulent or laminar [52]. It is defined as the ratio of the inertial forces to viscous forces acting on the fluid. The Reynolds number can be expressed as:

$$Re = \frac{\rho u D}{\mu} \tag{3.48}$$

Where μ is the dynamic viscosity of the fluid, ρ is the density of the fluid, D is the internal diameter of the pipe, and u is the average velocity of the fluid.

The critical Reynolds numbers are for pipe flow defined as 2300, where the transition to turbulent flow normally occurs. Flow with a Re lower than 2300 is normally considered laminar, a smooth and streamlined flow. The transition to turbulent flow normally occurs at Re between 2300 – 4000. For Re greater than 4000, the flow is normally considered as a fully developed turbulent flow, which is a flow characterized by chaotic swirls and multiple eddies [53].

As observed from equation (3.47), the equation is in an implicit form that requires an iterative procedure to be solved. Helgaker [38] points out that an iterative process can be computationally expensive, especially if the friction factor is solved for each pipe section.

Although the Colebrook-White equation is widely used, alternative explicit approximations exist to the Colebrook-White equation that is easier to implement.

A common explicit approximation is the Haaland's approximation, which is found to be a fairly accurate approximation to the Colebrook-White equation [51]:

$$\frac{1}{\sqrt{f}} = -1.8\, log\left[\left(\frac{\epsilon}{3.7D}\right)^{1.11} + \frac{6.9}{Re}\right] \tag{3.49}$$

The recommended range for Haaland's approximation is for Reynolds numbers in the range $4000 \leq Re < 10^8$ and for $\frac{\epsilon}{D}$; $10^{-6} \leq \frac{\epsilon}{D} < 5 \cdot 10^{-2}$ [54].

The Churchill approximation is an explicit approximation covering the whole flow regime, laminar and turbulent [51]. The Churchill approximation is found to have an error of 2.19% of the Colebrook-White equation and is defined as:

$$f = 8\left(\left(\frac{8}{Re}\right)^{12} + \frac{1}{(A + B)^{1.5}}\right)^{\frac{1}{12}} \tag{3.50}$$

where:

$$A = \left(2.457 \ln \frac{1}{\left(\frac{7}{Re}\right)^{0.9} + 0.27\frac{\epsilon}{D}}\right)^{16} \tag{3.51}$$

$$B = \left(\frac{37530}{Re}\right)^{16} \tag{3.52}$$

The Churchill approximation was found by Winning and Coole [55] to be computationally efficient and an acceptable compromise between computational cost and error. In addition, Yufeng et al. [56] found that the Churchill and Colebrook-White equation gave almost identical results for friction factor calculations in a capillary tube.

3.2.2 Viscosity

The viscosity term μ, appears in the denominator of equation (3.48) and can be defined as a measure of how resistant a Newtonian fluid is to motion [53]. For a Newtonian fluid, the shear stress within the fluid is proportional to the velocity gradient, and the viscosity is the proportionality constant:

$$\tau_n(P) = \mu \frac{\partial u}{\partial x_n} \tag{3.53}$$

$\tau_n(P)$ is the shear stress normal to direction n, and $\frac{\partial u}{\partial x_n}$ represents the velocity gradient in direction n. For a given shear stress, it can be observed from equation (3.53) that the velocity gradient will increase if the viscosity decreases and vice versa [53]. The viscosity of gases will increase with an increase in the temperature. This is because the intermolecular collisions between the molecules increase in frequency with higher temperatures. These collisions will result in a disturbance of the molecules moving in different directions and not as a "unit," leading to more resistance in the flow [57].

Both Helgaker [38] and Langelandsvik [58] have suggested the Lee-Gonzales-Eakin (LGE) empirical correlation for viscosity calculations for natural gases. This correlation was found by Lee et al. [59] in 1966 and is based on experimental data for natural gases in the temperature range of 100 – 340 F (311 – 444 K) and the pressure range of 100 – 8000 psia (6.9 – 551.6 bar). The LGE correlation can be expressed as [59]:

$$\mu = K \exp(X \left(\frac{\rho}{1000}\right)^Y \tag{3.54}$$

where

$$K = \frac{(9.4 + 0.02M)\left(\frac{9T}{5}\right)^{1.5}}{209 + 19M + \left(\frac{9T}{5}\right)} \tag{3.55}$$

$$X = 3.5 + \frac{986}{\left(\frac{9T}{5}\right)} + 0.01M \tag{3.56}$$

$$Y = 2.4 - 0.2X \tag{3.57}$$

M denotes the molecular weight, and T is the temperature of the gas. The LGE correlation computes the viscosity in micropoise, where $1 \text{ micropoise } = 10^{-7} \frac{kg}{ms}$.

3.2.3 Heat transfer

Steady heat transfer will be considered for the model in this study. The heat transfer model will utilize an overall heat transfer coefficient based on a composite radial system with both conduction and convection occurring.

3.2.3.1 Fourier's law

Fourier's law [60] for heat transfer through conduction can be expressed as:

$$q_{r,cond} = -\lambda A \frac{dT}{dr} \tag{3.58}$$

Where q_r is the heat transfer rate, A is the area normal to the direction of heat transfer, λ is the thermal conductivity for the fluid or material, and $\frac{dT}{dr}$ is the temperature gradient where r denotes the radius from the center of the cylinder to each surface layer.

3.2.3.2 Newton's law of cooling

The gas will transfer heat to the surface of the cylindrical pipe through the mechanism of heat convection. This mechanism can be expressed by Newton's law of cooling[60]:

$$q_{r,conv} = hA(T_s - T_{\infty)} \tag{3.59}$$

Where h is the convection heat transfer coefficient, and $(T_s - T_{\infty)}$ is the difference between the surface and fluid temperature, respectively.

3.2.3.3 The overall heat transfer coefficient (U)

For a composite system similar to figure 3.3, there will be a heat transfer given that there is a temperature difference between the gas temperature (T_g) and the ambient temperature (T_a). In figure 3.3, *A* is the cross-sectional pipe, and *B* is the cross-sectional insulation surrounding the pipe. r_1 to r_3 denotes the radius from the center of the pipe to the wall film boundary layers between the gas and the pipe, pipe and the insulation, and insulation to the ambient, respectively. The heat transfer between $T_{s,1}$ & $T_{s,2}$, and $T_{s,2}$ & $T_{s,3}$ can be modeled with equation (3.58). Likewise, the heat transfer between the gas ($T_{g,1}$) and the inner surface ($T_{s,1}$) and the heat transfer between the outer surface ($T_{s,3}$) and the ambient (T_a) can be modeled with equation (3.59). A convenient way of simplifying the total heat transfer through a composite system is utilizing an overall heat transfer coefficient, *U* [60].

The total heat transfer for a composite system can be expressed as:

$$q_r = UA\left(T_{g,1} - T_a\right) \tag{3.60}$$

The overall heat transfer coefficient for the system in figure 3.3 can be expressed as follows:

$$U = \frac{1}{\frac{1}{h_1} + \frac{r_1}{\lambda_A} ln\, \frac{r_2}{r_1} + \frac{r_1}{\lambda_B} ln\, \frac{r_3}{r_2} + \frac{r_1}{r_3}\frac{1}{h_a}} \tag{3.61}$$

h_1 and h_a is the inner and outer convective heat transfer coefficient, respectively, and λ denotes the thermal conductivity of the material.

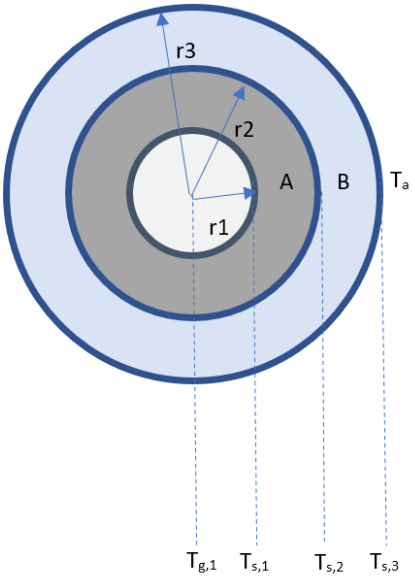

Figure 3.3: Example of a pipe with one layer of insulation

Nusselt number correlations can be implemented to calculate the convective heat transfer coefficient. Such a correlation is the Dittus-Boelter relation, which can be used to calculate the convective heat transfer coefficient for the heat transfer between the gas and the pipe's inner wall [38]. The Dittus-Boelter equation for turbulent flow is expressed as:

$$Nu = \frac{hL}{\lambda} = 0.023 \cdot Re^{0.8} \cdot P_r^n \tag{3.62}$$

Where Nu denotes the Nusselt number, λ is the thermal conductivity of the gas, L is the characteristic length, and P_r is the Prandtl number, which can be expressed as:

$$P_r = \frac{\mu \cdot C_p}{\lambda_{H_2}} \tag{3.63}$$

The n in P_r^n from equation (3.62) is chosen depending on whether heat is entering or leaving the system. The following relation yields:

$$n = \begin{cases} T \leq T_a & 0.3 \\ T > T_a & 0.4 \end{cases} \tag{3.64}$$

From expression (3.64), it can be seen that $n = 0.3$ if heat is entering the system and $n = 0.4$ if the heat is leaving the system.

3.2.4 Pipe leakage theory

A leakage in a pipeline can be modeled by adding a leakage source term to each equation and using the choked flow theory. The governing equations can then be written as follows [61]:

$$\frac{\partial \rho}{\partial t} + \frac{\partial (\rho u)}{\partial x} = -M_l \tag{3.65}$$

$$\frac{\partial(\rho u)}{\partial t} + \frac{\partial(\rho u^2 + p)}{\partial x} = -uM_l \tag{3.66}$$

$$\frac{\partial E}{\partial t} + \frac{\partial(E + p)u}{\partial x} = -(E_l + p_l)\frac{1}{\rho_l} M_l \tag{3.67}$$

The critical pressure ratio (CPR) is a term that can be used to identify the type of flow through the leakage orifice. The CPR indicates whether the flow is considered as subsonic or sonic and is here defined as the critical inside- to outside pressure ratio [61]:

$$CPR = \frac{p_{2cr}}{p_a} = \left(\frac{\gamma + 1}{2}\right)^{\left(\frac{\gamma}{\gamma-1}\right)} \tag{3.68}$$

In equation (3.68), p_a is the atmospheric pressure which is assumed to be homogeneous surrounding the pipe. p_{2cr} is the inside critical pressure at the leakage orifice.

This means that for a sonic flow, the criteria $\frac{p_2}{p_a} \geq CPR$ must be satisfied, and for the flow to be subsonic, the criteria $\frac{p_2}{p_a} \leq CPR$ is satisfied [61].

Isentropic flow through the orifice is a reasonable assumption for a gas leaving the control volume through a leakage orifice [61]. The following isentropic relationships for a sonic flow, assuming that the $Ma = 1$ at the leak orifice, can then be utilized:

$$\rho_l = \rho\left(\frac{2}{\gamma + 1}\right)^{\frac{1}{(\gamma-1)}} \tag{3.69}$$

$$u_l = c_l = c\sqrt{\frac{2}{\gamma + 1}} \tag{3.70}$$

For a subsonic flow, the isentropic relationship is dependent on the atmospheric pressure and pressure inside the pipe. The density and velocity through the orifice can be expressed with the following equations [61]:

$$\rho_l = \left(\frac{p_a}{p}\right)^{\frac{1}{\gamma}} \rho \tag{3.71}$$

$$u_l = c\left\{\frac{2}{\gamma - 1}\left[\left(\frac{p_a}{p}\right)^{\frac{(\gamma-1)}{\gamma}} - 1\right]\right\}^{1/2} \tag{3.72}$$

The mass flux leaving through a leakage orifice can be expressed with the ratio of the leakage orifice area and the cross-sectional area of the pipe, which can be shortened to:

$$M_l = \rho_l u_l \left(\frac{D_o}{D}\right)^2 \tag{3.73}$$

Where the subscript *l* denotes the leakage point.

3.3 Finite Difference methods

Finite difference methods are used to approximate differential equations with finite differences and are commonly used when modeling one-dimensional (1D) compressible flow. The method is based on Taylor series expansion, and by truncating the Taylor series for a given function, one can obtain approximations of the derivatives in time and space [40]. The governing equations can be transferred from partial differential equations (PDE) to discretized algebraic expressions in both time and space.

There are mainly two methods of discretizing the domains, either explicit or implicit, with both having different advantages and disadvantages. The advantage of explicit methods is their simplicity in implementing, but explicit methods can be proved to only be stable for very small timesteps. Implicit methods are unconditionally stable but more complicated to implement [38]. An example of a simple implicit method is the backward Euler method for the time discretization and centered differences for the spatial discretization. This is shown in equations (3.74) and (3.75) [38].

$$\frac{\partial Y(x_i, t_{n+1})}{\partial t} = \frac{Y_i^{n+1} - Y_i^n}{\Delta t} + \mathcal{O}(\Delta t) \tag{3.74}$$

$$\frac{\partial Y(x_i, t_{n+1})}{\partial x} = \frac{Y_{i+1}^{n+1} - Y_{i-1}^{n+1}}{2\Delta x} + \mathcal{O}(\Delta x^2) \tag{3.75}$$

Equations (3.74) and (3.75) are of 1st-order accuracy and 2nd – order accuracy, respectively.

For this study, a non-linear system of hyperbolic conservation laws will be implemented to a suited finite difference scheme.

3.3.1 The Riemann Problem

When considering a gas pipe flow model with an expected discontinuity, it is important to mention the Riemann problem. According to LeVeque [62], the Riemann problem "… *is simply the hyperbolic equation together with special initial data".*

$$q(x, 0) = \begin{cases} q_l & x < 0 \\ q_r & x > 0 \end{cases} \tag{3.76}$$

Equation (3.76) indicates that if a discontinuity occurs at t = 0, and x = 0, two separate states occur at q_l and q_r. Given that the system is a hyperbolic problem, the discontinuity will result in a set of waves propagating away from the origin, x = 0. Assuming $q_r = Q_i$ and $q_l = Q_{i-1}$, information used for flux computation can be obtained, and the cell values can be updated. The system's eigenvalues and eigenvectors must be considered when solving Riemann problems. Because the exact solution to the Riemann problem is computationally expensive, approximate Riemann solvers are used when implementing numerical methods [62]. For approximating the Riemann problem, two common methods are used. Either by approximating the numerical flux directly or evaluating the flux by approximating the state. An example of an approximate Riemann solver is the Harten, Lax, and van Leer (HLL) solver, which approximates the numerical intercell flux directly [40].

3.3.2 Courant-Friedrich-Lewy number

The CFL number is a dimensionless quantity in the range $[0\ ,1]$ and usually taken as the empirical value of 0.9. The CFL number is defined in equation (3.77) [40].

$$CFL = \frac{\Delta t\ a}{\Delta x} \tag{3.77}$$

Where a is the wave propagation speed.

The CFL number considers the ratio between the wave propagation speed and the grid speed $\frac{\Delta x}{\Delta t}$ [40]. A low value of the CFL number will lead to more diffusive simulation results and a very small time step, and should be kept as close to one as possible [63]. From equation (3.77), it follows that the time step Δt can be calculated as follows:

$$\Delta t = \frac{CFL\ \Delta x}{a} \tag{3.78}$$

where a can be calculated as $a = \max\big(C + abs(u)\big)$, where C is the speed of sound and u is the gas velocity [40].

3.3.3 Lax-Wendroff scheme

For a non-linear system of hyperbolic conservation laws, the 2nd-order accurate two-step Richtmyer version of the Lax-Wendroff scheme can be implemented. It is common to refer to this scheme as both the Richtmyer scheme and the two-step Lax-Wendroff scheme. The advantage of this scheme is that the system of governing equations can be evaluated directly without needing eigenvalues or taking the Riemann problem into account [40].

The governing equations must be written in the following form [40]:

$$\frac{\partial \mathbf{A}}{\partial t} + \frac{\partial \mathbf{B}}{\partial x} + \mathbf{C} = 0 \tag{3.79}$$

Where **A** denotes the time derivatives, **B** denotes the flux terms, and **C** denotes the source terms.

The first steps of the Lax-Wendroff two-step method are as follows [38]:

$$\mathbf{A}_{i\,+\,1/2}^{n+\,1/2} = \frac{1}{2}(\mathbf{A}_{i+1}^{n} + \mathbf{A}_{i}^{n}) - \frac{\Delta t}{2\Delta x}(\mathbf{B}_{i+1}^{n} - \mathbf{B}_{i}^{n}) - \frac{\Delta t}{4}(\mathbf{C}_{i+1}^{n} + \mathbf{C}_{i}^{n}) \tag{3.80}$$

$$\mathbf{A}_{i-\,1/2}^{n+\,1/2} = \frac{1}{2}(\mathbf{A}_{i}^{n} + \mathbf{A}_{i-1}^{n}) - \frac{\Delta t}{2\Delta x}(\mathbf{B}_{i}^{n} - \mathbf{B}_{i-1}^{n}) - \frac{\Delta t}{4}(\mathbf{C}_{i}^{n} + \mathbf{C}_{i-1}^{n}) \tag{3.81}$$

And the second step:

$$\mathbf{A}_{i}^{n+\,1} = \mathbf{A}_{i}^{n} - \frac{\Delta t}{\Delta x}\big(\mathbf{B}_{i+\,1/2}^{n+\,1/2} - \mathbf{B}_{i-1/2}^{n+\,1/2}\big) - \frac{\Delta t}{2}\big(\mathbf{C}_{i+\,1/2}^{n+\,1/2} + \mathbf{C}_{i-1/2}^{n+\,1/2}\big) \tag{3.82}$$

The intercell fluxes $\mathbf{B}_{i+\,1/2}^{n+\,1/2}$ and $\mathbf{B}_{i-1/2}^{n+\,1/2}$ are calculated from the solution of the first step $\mathbf{B}_{i+\,1/2}^{n+\,1/2} = \mathbf{B}\big(\mathbf{A}_{i\,+\,1/2}^{n+\,1/2}\big)$ and $\mathbf{B}_{i-\,1/2}^{n+\,1/2} = \mathbf{B}\big(\mathbf{A}_{i-\,1/2}^{n+\,1/2}\big)$. Identical to the intercell fluxes, the

intercell source term values can be calculated as $\mathbf{C}_{i+1/2}^{n+1/2} = \mathbf{C}\left(\mathbf{A}_{i+1/2}^{n+1/2}\right)$ and $\mathbf{C}_{i-1/2}^{n+1/2} = \mathbf{C}\left(\mathbf{A}_{i-1/2}^{n+1/2}\right)$.

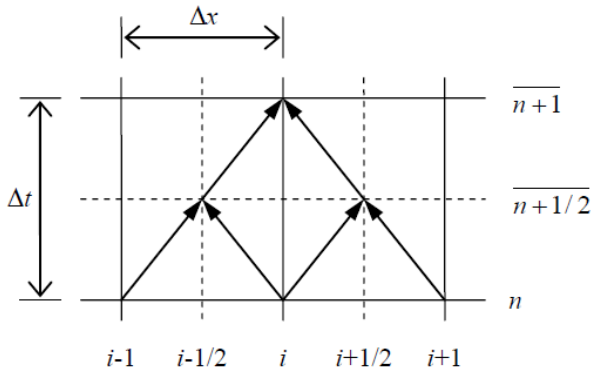

Figure 3.4: Computational stencil for two-step Lax-Wendroff scheme [64].

Figure 3.4 shows the stencil for the two-step Lax-Wendroff scheme. As indicated by equation (3.80 – 3.82), the intercell values for both space and time, $i \pm 1/2$ and $n \pm 1/2$, is calculated before moving one time step further $n + 1$. The Lax-Wendroff method uses centered differences in space and is 2nd order accurate in both time and space. 2nd- order accuracy indicates better accuracy than a 1st-order scheme, but will likely be more prone to produce spurious oscillations near sharp and steep gradients behind the wave [40].

The Lax-Wendroff scheme must satisfy the condition $CFL \leq 1$ to be stable.

3.3.4 Lax-Friedrichs scheme

Another popular and well-known scheme is the Lax-Friedrich scheme. This scheme is 1st-order accurate and more diffusive than the two-step Lax-Wendroff scheme. Lax-Friedrich uses forward differences in time and central differences in space but is stabilized by averaging $\mathbf{A}_i^n$ over its neighbor cells [63]. As the scheme has a monotonic characteristic, it can be used to stabilize an unstable scheme, and the scheme is conditionally stable if the condition $CFL \leq 1$ is satisfied [40]. The governing equations can be written as in equation (3.79).

The Lax-Friedrich scheme can be expressed by the discretized system [40]:

$$\mathbf{A}_i^{n+1} = \mathbf{A}_i^n - \frac{\Delta t}{\Delta x}\left(\mathbf{B}_{i-1/2} - \mathbf{B}_{i+1/2}\right) \tag{3.83}$$

Where the Lax-Friedrich intercell fluxes are calculated as follows:

$$\mathbf{B}_{i+1/2}^{\mathrm{LF}} = \frac{1}{2}\left(\mathbf{B}_i^n + \mathbf{B}_{i+1}^n\right) + \frac{\Delta x}{2\Delta t}\left(\mathbf{A}_i^n - \mathbf{A}_{i+1}^n\right) \tag{3.84}$$

3.3.5 Upwind scheme

While the Lax-Friedrich and the two-step Lax Wendroff schemes use central differences as approximations for the spatial derivative, the well-known 1st-order accurate Upwind scheme uses one-sided approximation. This means that the scheme uses information for spatial approximation from points on the side and in the direction of the flow [63].

For a general conservation equation, the upwind scheme can be written as shown in (3.85) and (3.86):

$$\mathbf{A}_i^{n+1} = \mathbf{A}_i^n - \frac{\Delta t}{\Delta x}(\mathbf{B}_{i+1} - \mathbf{B}_i) \tag{3.85}$$

$$\mathbf{A}_i^{n+1} = \mathbf{A}_i^n - \frac{\Delta t}{\Delta x}(\mathbf{B}_i - \mathbf{B}_{i-1}) \tag{3.86}$$

The sign of the propagating wave speed will decide whether equation (3.85) or (3.86) is selected. If a forward propagating wave is assumed, equation (3.85) yields and vice versa [63].

The upwind scheme is conditionally stable as long as the CFL condition $CFL \leq 1$ is satisfied and is a quite popular scheme that can be extended to higher-order accuracy and total variating diminishing schemes [40].

3.3.6 Total Variating Diminishing scheme

According to Toro [40]:

> "*A subclass of Total variation stable methods is those whose total variation does not increase in time; these are commonly referred to as Total Variating Diminishing (TVD) methods…".*

As mentioned in section 3.3.3, the 2nd-order Lax-Wendroff scheme produces spurious oscillations at sharp gradients that overpredict the solution compared to the exact solution. Highly oscillating schemes will increase their variation with time and are prone to a large total variation [40].

A numerical scheme is TVD if:

$$TV(u^{n+1}) \leq TV(u^n) \tag{3.87}$$

Equation (3.87) indicates that the scheme is TVD if the total variation of the next level time step is less or equal to the previous timestep [40].

A widely used method to establish a TVD scheme for a high order numerical scheme is a flux limiter approach. The basic idea of a flux limiter is to establish a scheme that uses a low order monotone scheme for the fluxes when at sharp gradients and a high order scheme for the fluxes elsewhere.

3.3.7 TVD third order Runge-Kutta

An explicit TVD scheme of higher-order accuracy is the TVD 3rd – order Runge-Kutta scheme that can be used for the time discretization. The governing equations must be written as [38]:

$$\frac{\partial \mathbf{q}}{\partial t} + \mathbf{D}\frac{\partial \mathbf{q}}{\partial x} = \mathbf{S} \tag{3.88}$$

q represents the flow variables, **D** denotes the coefficient matrix, and **S** denotes the source term vector.

$$\mathbf{q}^{(1)} = \mathbf{q}^n + \Delta t \mathbf{R}(\mathbf{q}^n) \tag{3.89}$$

$$\mathbf{q}^{(2)} = \frac{3}{4}\mathbf{q}^n + \frac{1}{4}(\mathbf{q}^{(1)} + \Delta t \mathbf{R}(\mathbf{q}^1)) \tag{3.90}$$

$$\mathbf{q}^{(n+1)} = \frac{1}{3}\mathbf{q}^n + \frac{2}{3}(\mathbf{q}^{(2)} + \Delta t \mathbf{R}(\mathbf{q}^{(2)})) \tag{3.91}$$

R denotes the vectors of the spatial derivatives and the source terms [38]. The Runge-Kutta schemes can be implemented as different variants, usually with accuracy from 1st to 4th order, where the 1st and 2nd order is the Euler's- and Heun's methods, respectively [63]. Welahettige [65] implemented a 4th – order Runge-Kutta method to handle the source terms by source terms splitting.

3.3.8 First-Order Centered Scheme (FORCE)

The First-Order Centered Scheme (FORCE) [40] is based on the Random Choice Method (RCM), but the stochastic steps from RCM have been replaced by deterministic versions by integral averages of the Riemann problem.

The First-Order Centered Scheme (FORCE) is in conservation form given by:

$$\mathbf{A}_i^{n+1} = \mathbf{A}_i^n + \frac{\Delta t}{\Delta x}\left(\mathbf{B}_{i-1/2} - \mathbf{B}_{i+1/2}\right) \tag{3.92}$$

The intercell fluxes can be shown to become the average of the fluxes between the Richtmyer Lax-Wendroff two-step scheme (RI), and the fluxes from the Lax-Friedrich (LF) scheme:

$$\mathbf{B}_{i+1/2}^{\mathrm{FORCE}} = \frac{1}{2}\left(\mathbf{B}_{i+1/2}^{\mathrm{RI}} + \mathbf{B}_{i+1/2}^{\mathrm{LF}}\right) \tag{3.93}$$

$$\mathbf{B}_{i-1/2}^{\mathrm{FORCE}} = \frac{1}{2}\left(\mathbf{B}_{i-1/2}^{\mathrm{RI}} + \mathbf{B}_{i-1/2}^{\mathrm{LF}}\right) \tag{3.94}$$

With CFL < 1, the FORCE scheme is found to be stable and has a monotone characteristic.

3.3.9 A Flux Limiter Centered Scheme

A Flux Limiter Centered Scheme (FLIC) [40] is a 2nd -order accurate and TVD scheme that, together with a flux limiter function, combines the low-order FORCE fluxes with the high-

order Richtmyer fluxes. The fluxes from the Richtmyer scheme and FORCE scheme are both obtained by centered differences. The high order Richtmyer flux is denoted as:

$$\mathbf{B}_{i\pm 1/2}^{HI} = \mathbf{B}_{i\pm 1/2}^{RI} \tag{3.95}$$

And the low order monotone FORCE flux is denoted as:

$$\mathbf{B}_{i\pm 1/2}^{LO} = \mathbf{B}_{i\pm 1/2}^{FORCE} \tag{3.96}$$

Then a general flux limiter method can be given as:

$$\mathbf{B}_{i\pm 1/2} = \mathbf{B}_{i\pm 1/2}^{LO} + \phi_{i\pm 1/2}\left(\mathbf{B}_{i\pm 1/2}^{\mathrm{HI}} - \mathbf{B}_{i\pm 1/2}^{\mathrm{LO}}\right) \tag{3.97}$$

Where $\phi_{i+1/2}$ is the flux limiter function. As can be seen from equation (3.97), the value of $\phi_{i+1/2}$ will determine whether the scheme becomes a low order- or a high order scheme. If $\phi_{i+1/2} = 0$, the scheme becomes $\mathbf{B}_{i+1/2} = \mathbf{B}_{i+1/2}^{LO}$, a low order scheme. And if $\phi_{i+1/2} = 1$, the scheme becomes $\mathbf{B}_{i+1/2} = \mathbf{B}_{i+1/2}^{HI}$, a high order scheme.

Various flux limiter schemes can be chosen to obtain a non-oscillatory nature, but Toro [40] suggests using either SUPERBEE (SB), VANLEER (VL), VANALBADA (VA), or MINBEE (MB) for a centered flux scheme. These flux limiter schemes are given by:

$$\phi_{SB}(r) = \begin{cases} 0, & r \le 0, \\ 2r, & 0 \le r \le 0.5, \\ 1, & 0.5 \le r \le 1, \\ min\{2, \phi_g + (1-\phi_g)r\}, & r > 1, \end{cases} \tag{3.98}$$

$$\phi_{VL}(r) = \begin{cases} 0, & r \le 0 \\ \dfrac{2r}{1+r} & 0 \le r \le 1 \\ \phi_g + \dfrac{2(1-\phi_g)r}{1+r} & r \ge 1 \end{cases} \tag{3.99}$$

$$\phi_{VA}(r) = \begin{cases} 0, & r \le 0 \\ \dfrac{r(1+r)}{1+r^2} & 0 \le r \le 1 \\ \phi_g + \dfrac{(1-\phi_g)r(1+r)}{1+r^2} & r \ge 1 \end{cases} \tag{3.100}$$

$$\phi_{MB}(r) = \begin{cases} 0, & r \le 0 \\ r & 0 \le r \le 1 \\ 1 & r \ge 1 \end{cases} \tag{3.101}$$

ϕ_g is defined as:

$$\phi_g \equiv \frac{(1 - c_{max})}{(1 + c_{\max})} \tag{3.102}$$

Where $c_{\max}$ can be set to equal the CFL number, $c_{\max} = CFL$.

To calculate r, Toro [40] suggests using the total energy as the variable and defining $q \equiv E$. Then r can be calculated for the right and left intercells, denoted by *R* and *L* respectively.

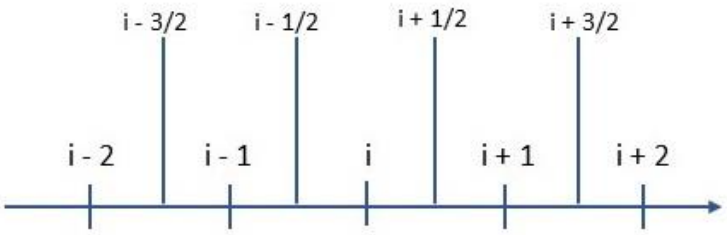

Figure 3.5: grid showing intercell boundaries

For $r_{i+1/2}$ there is a need to calculate the intercell flux on the left side of $i + 1/2$ and on the right side of $i + 1/2$. By observing figure 3.5 and following the procedure presented by Toro [40], the following expressions can be implemented for r:

$$r^L_{i+1/2} = \frac{\Delta q_{i-1/2}}{\Delta q_{i+1/2}} = \frac{q_i - q_{i-1}}{q_{i+1} - q_i} \tag{3.103}$$

$$r^R_{i+1/2} = \frac{\Delta q_{i+3/2}}{\Delta q_{i+1/2}} = \frac{q_{i+2} - q_{i+1}}{q_{i+1} - q_i} \tag{3.104}$$

And similar for $r_{i-1/2}$ yields:

$$r^L_{i-1/2} = \frac{\Delta q_{i-3/2}}{\Delta q_{i-1/2}} = \frac{q_{i-1} - q_{i-2}}{q_i - q_{i-1}} \tag{3.105}$$

$$r^R_{i-1/2} = \frac{\Delta q_{i+1/2}}{\Delta q_{i-1/2}} = \frac{q_{i+1} - q_i}{q_i - q_{i-1}} \tag{3.106}$$

Finally, the flux limiter can be determined by the following equation for both $r_{i-1/2}$ and $r_{i+1/2}$, where the minimum value of the intercell boundary on either right or left side is chosen [40]:

$$\phi^{LR} = \min\{\phi(r^L_{i+1/2}), \phi(r^R_{i+1/2})\} \tag{3.107}$$

The Superbee flux limiter is the least diffusive but prone to oscillations near sharp gradients, while Minbee is the most diffusive flux limiter. Minbee is least prone to obtain spurious oscillations but may smoothen discontinuities due to its diffusive nature [40]. Welahettige [65] points out in his Ph.D. thesis that the Superbee flux limiter will keep the second-order accuracy of the scheme.

3.3.10 Boundary Conditions

A common method to implement boundary conditions is by the use of "ghost cells" (GC) which are fictitious cells placed "outside" of the domain, left and right at the boundaries. For a spatial domain discretized into Nx cells, this can be done by specifying a cell left for x = 0 as cell 0, and a fictitious cell to the right of the domain's end, denoted Nx +1. This is illustrated in figure 3.6.

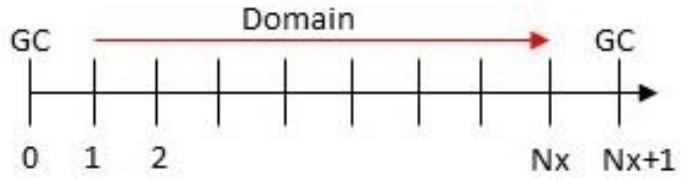

Figure 3.6: Domain showing ghost cells

The Neumann- and Dirichlet boundary conditions are common methods to define the end boundaries. The Neumann boundary condition considers the gradient to the variable as a zero gradient. For a given flow variable Y, the Neumann boundary condition is expressed as:

$$\frac{\partial Y}{\partial x} = 0 \tag{3.108}$$

The Dirichlet boundary conditions are fixed values. For a flow variable Y, the Dirichlet boundary condition for x = 0, can be expressed as Y(0) = 5 [63].

3.3.11 Source terms

The source terms, **C**, can be treated with source-terms splitting, here shown with the 1st- order accurate and explicit Euler method [40]. With source-term splitting, the advection terms are solved first with, e.g., the FORCE scheme, shown in equation (3.92). The solution in equation (3.92) can be replaced with a temporary solution expressed as $\mathbf{A}^* = \mathbf{A}^{n+1}$. The final solution is obtained when the source terms are added to the temporary solution as shown by equation (3.109).

$$\mathbf{A}^{n+1} = \mathbf{A}^* + \Delta t \mathbf{C}(t^n, \mathbf{A}^n) \tag{3.109}$$

3.4 Model development

As mentioned in the introduction, a physical leak flow model for a maritime fuel cell system is in the progress of being built at the USN. One of the main objectives of this study is to develop a numerical one-dimensional leak flow model based on the physical model. The model shall be transient, consider the effects of a gas leak, and capture the rarefaction waves that initially occur in the pipeline.

The dynamic leak flow model will be developed with a simplified compressed gas fuel cell system as a basis, and such a system is illustrated in figure 3.7. The total system consists of a pressure vessel containing compressed hydrogen gas (CGH_2), a pipeline, sensors for measuring pressure and flow rate, and a fuel cell module (FC). The dynamic leak flow model developed during this study will be limited to contain only the pipeline with an inlet at the storage tank side and an outlet at the fuel cell side. The dynamic leak flow model's control volume is marked with the dotted line, and only the system within the dotted line will be considered in this study. The gas has been reduced to work pressure before entering the domain.

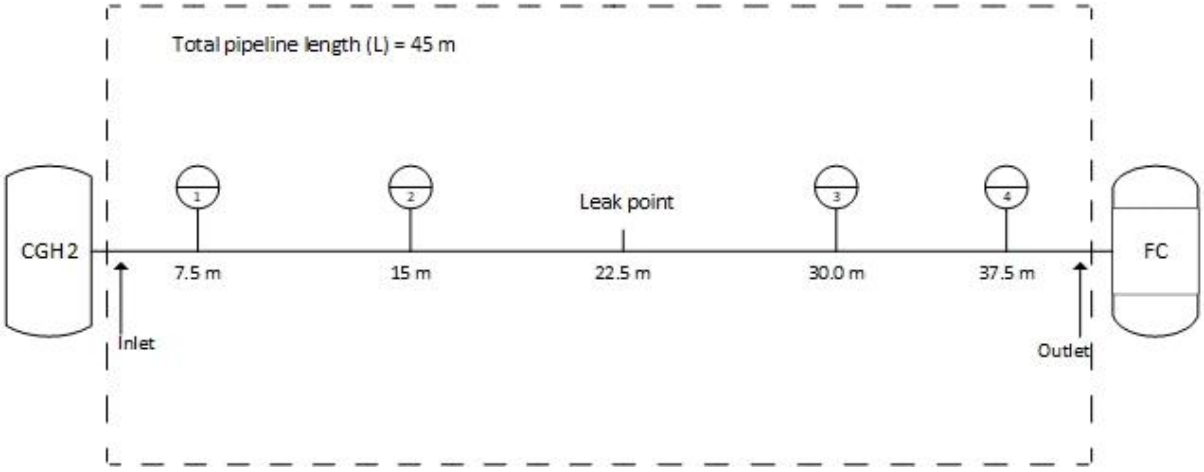

Figure 3.7: Sketch of the system to be modeled in this study

Pressure and flow sensors will be simulated at equal distances from the leak point upstream and downstream. The sensors are crucial in such a system for the ability of leak detection. In addition, the pipeline will consist of twenty 90˚ bends, being placed with equal spacing between each bend. Flow and pressure regulating valves at the inlet have not been considered for the dynamic leak flow model in this study.

In this study, the leak flow model has been implemented using the software Python version 3.9.

Parameters used for the development of the dynamic leak flow model are tabulated in table 3.1 and are used as initial conditions for the simulations if nothing else is specified:

Table 3.1: Model parameters

Parameter	Value	Unit
Total pipeline length (L)	45.0	[m]
Inner diameter (D)	9.0	[mm]
Outer Diameter (OD)	12.0	[mm]
Number of 90˚bend	20	[-]
Internal roughness (ϵ)	$0.025 \cdot 10 - 3$	[m]
Ambient Temperature (T_a)	293.15	[K]
Atmospheric Pressure (p_a)	101325.0	[Pa]
Work Pressure (p)	10.0	[bar]
Inlet gas velocity [u]	30.0	[m/s]
Inlet Density (ρ)	0.822	[kg/m^3]
Gas constant, Hydrogen (R)	4124.2	[J/KgK]
γ	1.41	[-]
c_p	0.0144	[J/KgK]

c_p and γ are assumed to be constant for this system. As can be observed from equations (3.39) and (3.40), the specific heat capacity with constant volume and pressure are both dependent on the temperature. However, the temperature change in the dynamic leak flow model is expected to be small. Therefore, the change in γ and c_p is approximated as negligible, and the value is considered constant. The inlet density is calculated manually with the Abel-Noble EOS, considering the inlet pressure and ambient temperature.

The length of the pipeline is discretized into Nx = 2000 grid cells, where the distance between each cell is taken as $dx = \frac{L}{Nx} = 0.0225m$.

In this study, a CFL number equal to 0.87 has been chosen for the simulations, which has been identified as stable due to trial and error in the developed model.

The implementation of the time step is performed as in equation (3.78), with $a = \max\big(C + abs(u)\big)$.

The spatial marching is performed with slicing and vectorization in Python, while the time marching is performed with a for-loop.

The non-linear hyperbolic equations (3.31, 3.34 – 3.35) are written as equation (3.79), resulting in equation (3.110).

$$\mathbf{A} = \begin{bmatrix} \rho \\ \rho u \\ E \end{bmatrix} \quad \mathbf{B} = \begin{bmatrix} \rho u \\ (\rho u^2 + p) \\ (E + p)u \end{bmatrix} \quad \mathbf{C} = \begin{bmatrix} 0 \\ -\frac{f\rho|u|u}{2D} - K_t\frac{\rho u^2}{2} \\ -\frac{4q}{D} - \frac{2f\rho|u|^3}{D} \end{bmatrix} \tag{3.110}$$

and a FLIC scheme as described in section 3.3.7 is implemented for the model using Superbee and Minbee as flux limiters.

3.4.1 Computation procedure

The scheme is initialized by applying the initial conditions in table 3.1 for the whole spatial domain, and the **A**, **B**, and **C** vectors are defined as shown in (3.110).

The $\mathbf{A}_{i+1/2}^{n+1/2}$ and $\mathbf{A}_{i-1/2}^{n+1/2}$ is computed with the Richtmyer (two-step Lax Wendroff) scheme, and the intercell flow variables are solved to enable the computation of the intercell fluxes, $\mathbf{B}_{i+1/2}^{n+1/2} = \mathbf{B}(\mathbf{A}_{i+1/2}^{n+1/2})$ and $\mathbf{B}_{i-1/2}^{n+1/2} = \mathbf{B}(\mathbf{A}_{i-1/2}^{n+1/2})$.

Fluxes from the Lax-Friedrich scheme, $\mathbf{B}_{i\pm1/2}^{\mathrm{LF}}$, is computed as shown in equation (3.84). With both the Richtmyer and Lax-Friedrich fluxes computed, the computation of the FORCE fluxes is performed as shown in equations (3.93 – 3.94).

The flux limiter is constructed using the total energy, E, and the FORCE and Richtmyer fluxes as the low- and high-order fluxes, respectively. Both Superbee and Minbee flux limiters have been implemented, following the suggested procedure by Toro [40], as described in section 3.3.9. The flux limiter measures the total variation of the solution, and with the Minbee flux limiter being implemented, the fluxes, $\mathbf{B}_{i\pm1/2}$, will become a first order scheme near sharp gradients and discontinuities, and a second-order scheme elsewhere. The Superbee flux limiter is claimed to maintain the scheme's second-order accuracy at sharp gradients. With the fluxes and flux limiter function being computed, the source terms are added to the temporary solution, $\mathbf{A}_i^*$ as shown in equation (3.109). Then one time step, $\mathbf{A}_i^{n+1}$, finally can be performed and new values for the flow variables can be calculated and updated. The vector **A** contains the flow variables $[\rho, \rho u, E]$ and the updated values for ρ, u, and E is used to calculate updated values for p and T by utilizing equation (3.46) and the Abel-Noble EOS. The time step is updated at the end of each loop in the time marching loop.

The leakage is modeled as source terms to the governing equations and implemented in the model in the same manner as shown in equation (3.109). Isentropic relations for both subsonic and sonic flow are implemented, with the CPR as the deciding point whether equations for subsonic or sonic flow should be utilized. Source terms for the leakage are set to be zero until a specified leak time occurs, and then the source terms will be implemented with their computed isentropic relations.

3.4.2 Validation method

The model in its homogenous form, without source terms, is tested and compared to the initial condition (IC) *test 2*, which is called the *123 problem* and described in Toro [40]. As

the rarefaction waves that occur due to a leakage in the system are of interest in this study, *test 2* is assumed to be a suitable tool for testing the model. T*est 2* has a solution with two rarefaction waves and a stationary contact discontinuity. The exact solution of *test 2* can be observed in figure 3.8. According to Toro [40], *test 2* is used to test the performance of numerical schemes with a low-density flow. The numerical schemes can have trouble computing *test 2* as the pressure is close to the vacuum. This is seen in schemes like the Lax-Wendroff scheme.

Table 3.2: Initial conditions for *Test 2* [40]

Test	ρ_l	u_l	p_l	ρ_r	u_r	p_r
2	1.0	- 2.0	0.4	1.0	2.0	0.4

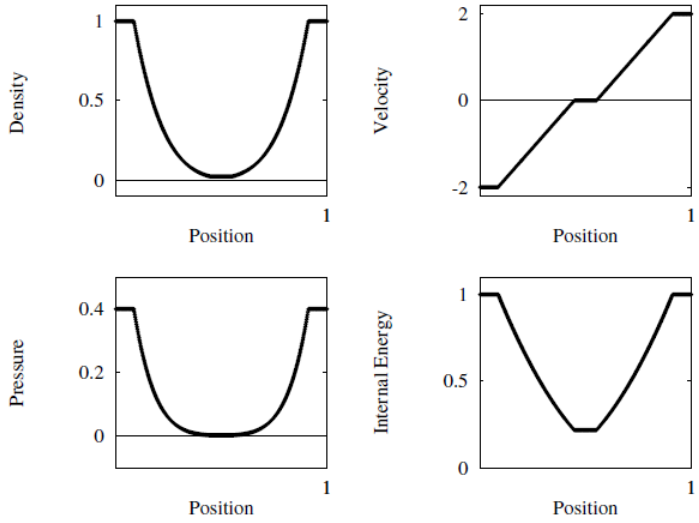

Figure 3.8: The exact solution of *test 2* for density, velocity pressure, and specific internal energy [40]

Validation of the implemented model with source terms will mainly be performed by comparing simulated results with hand calculations.

3.4.3 EOS

From the literature review, it is found that for pressures above 10 MPa, a real-gas EOS should be used. Still, only moderate pressures up to 10 bar are evaluated in this study, and the ideal gas assumption is probably applicable. However, the simple and easy-to-implement EOS Abel-Noble is implemented in the dynamic leak flow model, which is believed to make the model more versatile if higher pressures were to be investigated. The Able-Noble co-volume constant is taken as $b = 7.691 \cdot 10^{-3}$. If ideal gas EOS is preferred, it is quite simple obtained by setting $b = 0$ in the model. In addition, five premade initial conditions have been implemented in the model, and steady-state variables have been stored after 30000 time steps for both Abel-Noble and the ideal gas EOS. The stored variables can be used to start the simulation in a steady-state. One can switch between the ideal gas EOS and Abel-Noble in the code by only changing the implemented initial condition selector using the stored steady-

state variables. The stored variables are attached electronically as own files together with the Python script in Appendix E.

3.4.4 Implemented source terms

This section will focus on each source term that has been included in the dynamic leak flow model. Implementation of the source terms to the FLIC scheme is as described in section 3.3.11.

3.4.4.1 Friction

The friction source terms the momentum and energy equation is expressed in equations (3.111 – 3.112), respectively.

$$\mathbf{C}_{fric} = \frac{f\rho|u|u}{2D} \tag{3.111}$$

$$\mathbf{C}_{fricwork} = \frac{2f\rho u^3}{D} \tag{3.112}$$

Both equations (3.111 – 3.112) contain the Darcy-Weisbach friction factor (f), which is calculated by the Churchill correlation, described by equations (3.50 – 3.52). To have enough information to compute f, the dynamic viscosity, μ, have to be calculated as it appears in the Reynolds number calculation. μ is calculated using empirical data from the website [66], which has been plotted in MS Excel for 1, 10, 50, and 100 bar. Then the equation for the trendline was found, and an approximately linear relationship was found, as shown in figure 3.9.

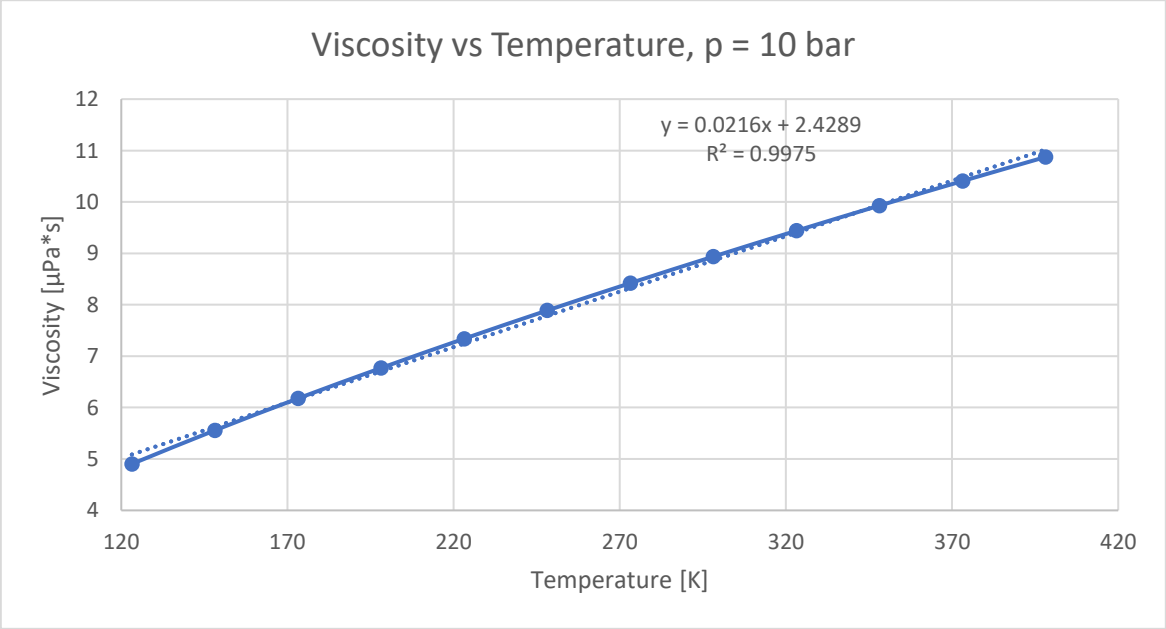

Figure 3.9: Viscosity vs. temperature with trendline, 10 bar. Based on empirical data from [66].

From figure 3.9, the value of $R^2 = 0.9975$, which indicates that the data fits well for a linear relationship, with $R^2 = 1$ being the best fit. The equation obtained for the trendlines is implemented in the dynamic leak flow model for selected pressures. A linear interpolation function has been implemented in the code to handle cases where the work pressures are between the implemented pressure levels. Graphs showing the trendlines for the remaining implemented pressures are attached in Appendix C. If the work pressure is below 1bar or above 100 bar, a simplification has been made by using the trendline for 1- and 100 bar, respectively.

For very low Reynolds numbers, Re < 100, the friction factor is set to be a constant of 0.6 as a simplification. This is to avoid the case of division by zero or overflow during the computation of the Churchill equation.

Equation (3.111) is calculated for each cell, meaning that if calculating the whole length, *L*, of the pipeline by hand, the friction term would have been:

$$\mathbf{C}_{fric} = \frac{f\rho|u|uL}{2D} \tag{3.113}$$

The computation of (3.111) is performed in each cell for the whole domain, where the term (3.111) is multiplied by the length of each cell, *dx*, as shown in equation (3.114). The total Δp is calculated and updated for each loop and summarized at the end of the simulation. This procedure is identical for equation (3.109).

$$\mathbf{C}_{fric} = \frac{f\rho|u|u}{2D}dx \tag{3.114}$$

As the source term will be multiplied with dx during the simulations, the implemented version of the friction source terms is as expressed with equations (3.110 – 3.111).

3.4.4.2 Minor losses

The pipeline is designed with 20 bends which are assumed to be regular 90˚ flanged elbows. According to [67], the minor loss coefficient, K, for such elbow bends are equal to 0.3, $K = 0.3$. The minor loss equation is here expressed as shown in equation (3.114).

$$\mathbf{C}_{\text{minor}} = K_t \frac{\rho u^2}{2} \tag{3.115}$$

Here K_t denotes the total minor loss coefficient, meaning if hand calculation were to be performed, the total minor loss coefficient would have been, $K_t = 20 \cdot K$ for a number of 20 bends.

The minor loss equation is implemented on 20 different cells in the spatial domain of the pipeline. To avoid having a bend placed in the first and last part of the pipeline, $2 * \left(\frac{Nx}{N_{bend}}\right)$ has been subtracted from the total spatial domain, and the bends are distributed with equal spacing between the bends. The first bend is placed at $Bend_{loc} = \frac{Nx - 2*\left(\frac{Nx}{N_{bend}}\right)}{Nx}$, which is approximately 2m downstream from the inlet of the 45 m pipeline.

Then the next bend is placed at $2 * Bend_{loc}$, and equally spaced up to $20 * Bend_{loc}$ where the last bend is placed approximately 40.5 m downstream from the inlet of the 45 m pipeline.

During the integrations in the simulation, the computed values are divided over the whole domain due to the multiplication with dx. Therefore, $K_t = \frac{K}{dx}$, which is implemented in the model for correct computation of the losses at the given cell. The implemented expression of equation (3.115) then becomes:

$$\mathbf{C}_{\text{minor}} = \frac{K_t}{dx}\frac{\rho u^2}{2} \tag{3.116}$$

3.4.4.3 Gravity term

The pipeline is assumed to be horizontal, and the fluid considered is hydrogen which is a low-density gas. Therefore, the gravity term, $\rho g \sin\alpha$, in the momentum equation is neglected in this study.

3.4.4.4 Heat transfer

The heat transfer source term in the energy equation is here expressed as:

$$\mathbf{C}_{\text{heat}} = \frac{4q}{D} \tag{3.117}$$

where the heat flux is expressed as:

$$q = U\left(T_{g,1} - T_a\right) \tag{3.118}$$

For the current pipe model, the expression for the overall heat transfer coefficient (3.61) becomes:

$$U = \frac{1}{\frac{1}{h_{gw}} + \frac{r_1}{\lambda_{pipe}} ln\,\frac{r_2}{r_1} + \frac{r_1}{r_2}\frac{1}{h_{air}}} \tag{3.119}$$

h_{gw} is calculated with the Dittus-Boelter equation and the Prandtl number expressed by equations (3.62) and (3.63). Similar to the viscosity calculation for the friction terms, the thermal conductivity of the gas is calculated based on empirical data from the website [66]. The 10 bar pressure level, with its corresponding trendline, is plotted in figure 3.10.

As shown in figure 3.10, the trendline fits very well with the linear relationship with an R^2 = 0.9967. Trendlines for pressures of 1, 10, 50, and 100 bar have been computed and can be observed in Appendix D. If the working pressure is between two pressure levels, a linear interpolation is performed to obtain λ for the hydrogen gas. If the work pressure is below 1bar or above 100 bar, a simplification has been made using the trendline for the 1- and 100 bar trendline, respectively.

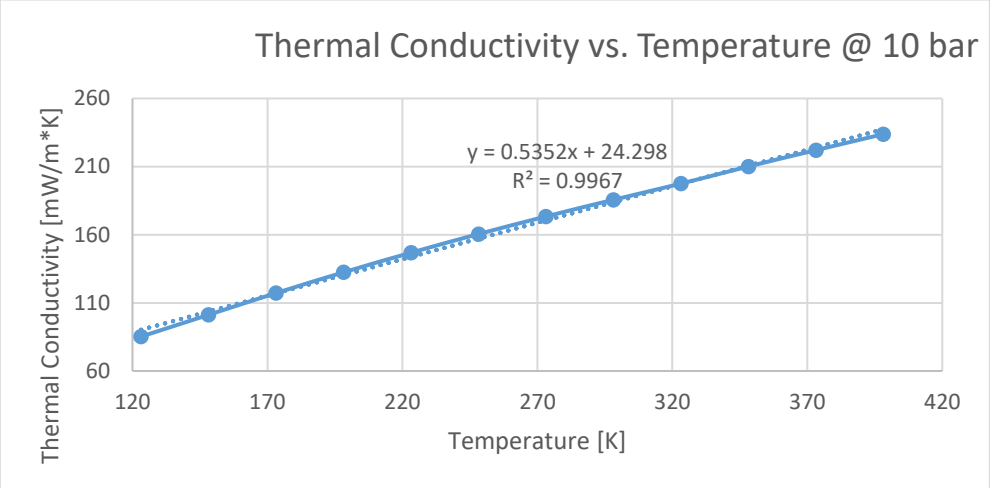

Figure 3.10: Thermal conductivity plotted with temperature with trendline. Based on empirical data from [66].

The thermal conductivity for the piping material, λ_{pipe}, is assumed to be 45 (W/mK), which is in the range of carbon steel [68], and the convective heat transfer coefficient for air is assumed to be 50 (W/m^2K) [60].

Similar to the friction terms in section 3.4.4.1, the heat transfer calculations are performed for each cell by multiplying with each cell's length, *dx*. The heat transfer term has been implemented as shown in equation (3.117).

3.4.5 Implemented BC's

Inlet:

The Neumann BCs (zero gradients) have been implemented for the inlet at the velocity, density, and total energy, and a fully developed flow has been assumed for the inlet. The Dirichlet BC (fixed value) has been implemented on the pressure, as the pressure is assumed to be known at the inlet.

Outlet:

Regarding the outlet, the Neumann BCs have been implemented on the pressure, density, and total energy. The velocity is assumed to be known at the outlet, and the Dirichlet BC has been implemented on the velocity to have a property that restricts the outlet. A boundary condition that restricts the flow at the outlet is necessary for the model to obtain a steady-state.

3.4.6 Leakage point

The leakage has been implemented using isentropic relations described in section 3.2.4, with the implementation of source terms described in section 3.3.11. According to Berstad et al. [61], the assumption of ideal gas- and that the flow through the leakage orifice is an isentropic process works sufficiently well. The leakage term has been modeled similarly to the minor losses equation described in section 3.4.4.2. The equation is divided by *dx* as the leakage occurs at a given point:

$$M_l = \frac{\rho_e u_e \left(\frac{D_o}{D}\right)^2}{dx} \tag{3.120}$$

Equation (3.120) is implemented as a source term in the continuity equation and further used for the leakage term for the momentum- and energy equation as shown in equation (3.65 – 3.67). The point of leakage is considered at $\frac{L}{2}$, which is at 22.5m for the given pipeline length of 45 m. The simulations are in a steady-state before the leakage is activated.

3.5 Model validation

In this section, the developed pipeline gas flow model will be validated by comparing it to literature and hand calculations. All hand calculations are compared to a simulation with the following initial conditions for the whole domain:

Table 3.3: Initial conditions for hand calculation

$\rho\ \left[\frac{kg}{m^3}\right]$	$p\ [Pa]$	$u\ \left[\frac{m}{s}\right]$
0.822	100000	30

All hand calculations are shown in Appendix F.

3.5.1 Test 2

Test 2 shows promising results for the schemes with both Minbee and Superbee as flux limiters. Figures 3.11 and 3.12 show the plotted results of test 2 after 200-time steps, and the results show similar behavior as the exact solution shown in figure 3.8. However, both Minbee and Superbee seem to be a little diffusive when looking at the velocities in figures 3.11 and 3.12 and compared with figure 3.8.

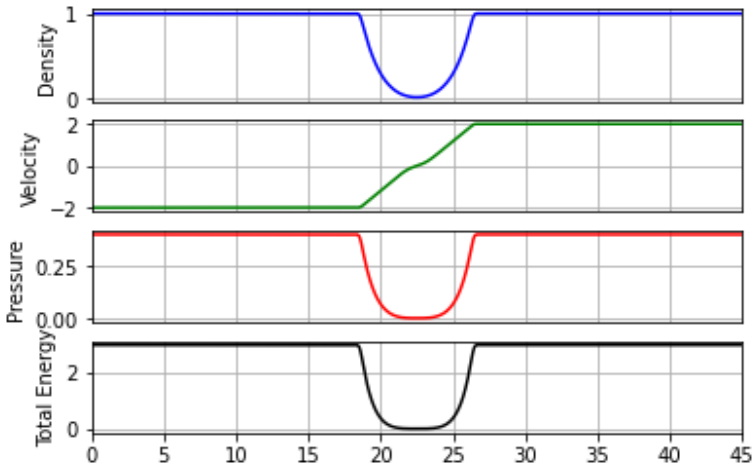

Figure 3.11: *Test 2 - FLIC scheme & Minbee flux limiter. Simulated with 200 time-steps. The plot is showing the flow variables density [kg/m^3], velocity [m/s], pressure [Pa], and total energy [J]. The x-axis represents the pipeline length 0 – 45m.*

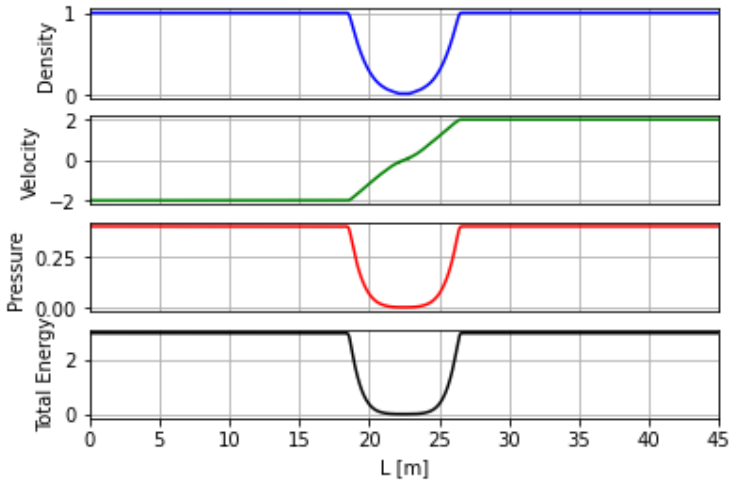

Figure 3.12: *Test 2 - FLIC scheme & Superbee flux limiter. Simulated with 200 time-steps. The plot is showing the flow variables density [kg/m^3], velocity [m/s], pressure [Pa], and total energy [J]. The x-axis represents the pipeline length 0 – 45m.*

3.5.2 Steady-state

The system to be modeled is a pipeline with gas flowing continuously. As the gas has been flowing for some time, it is expected that the gas will stabilize at a certain Δp due to natural flow effects like, e.g., friction. Therefore, the simulations should be in a steady-state before the leakage is initiated to obtain as realistic results as possible.

With source terms implemented, the model should reach a steady state after a number of time steps. The simulation presented in Figures 3.13 and 3.14 is performed with the length of the pipeline divided into 2000 cells, *Nx = 2000*, and the Minbee flux limiter. The initial conditions are in accordance with table 3.1. As shown in figure 3.13, the simulation seems to reach a steady-state after approximately 7000-time steps, which corresponds to 100 – 150 ms. In figure 3.14, the local effects of the 90˚ bends can be observed as small local changes in the velocity.

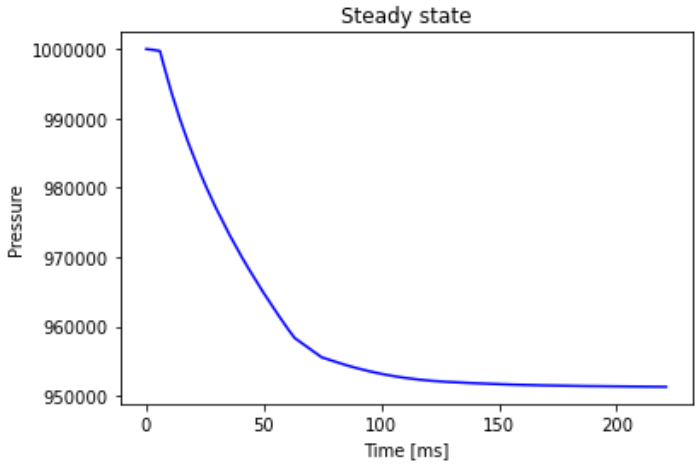

Figure 3.13: Pressure [Pa] plotted with respect to time. The pressure is measured at Pressure Sensor 4 (PS4), placed 37.5 m downstream of the pipe inlet.

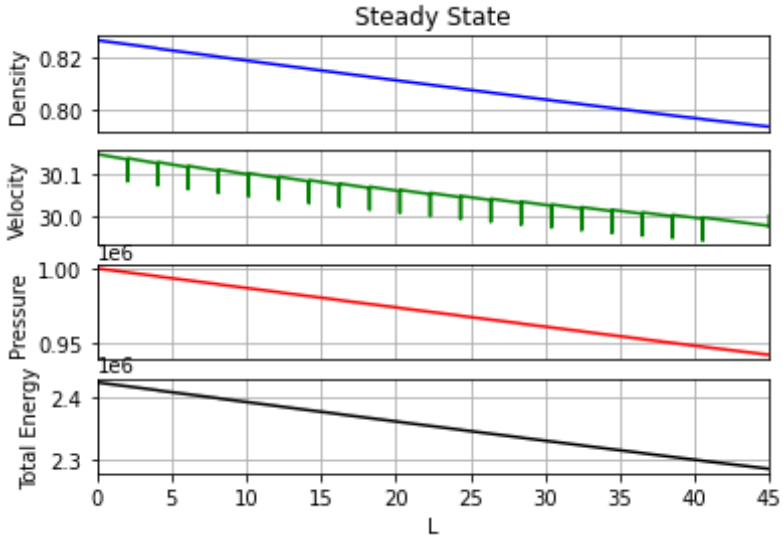

Figure 3.14: Steady-state flow variables, density [kg/m^3], velocity [m/s], pressure [Pa], and total energy [J] plotted vs Length of the pipeline [m]

3.5.3 Heat loss

The temperature difference, ΔT, between the inlet and outlet of the pipeline is simulated to be approximately 7 K. Simulation time was set to 15150 time steps, which corresponds to about 221 ms. The result can be observed in figure 3.15.

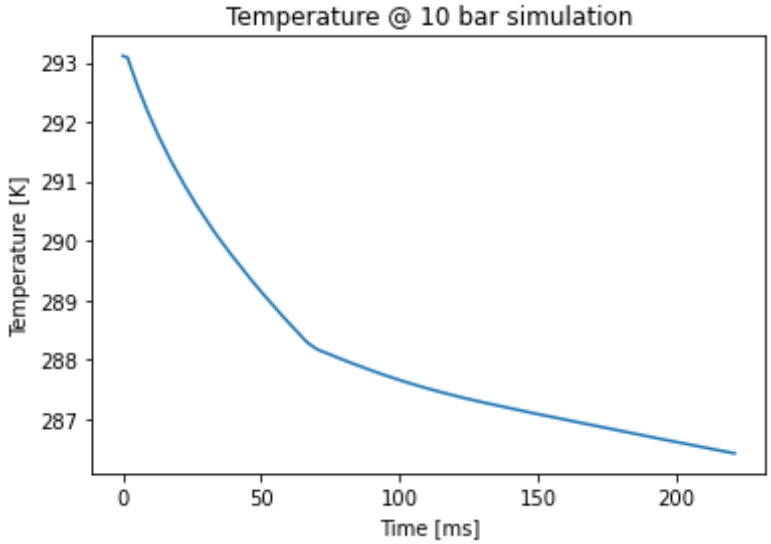

Figure 3.15: Temperature vs. Time plot. The plot shows the change in temperature at the outlet of the pipeline.

The dynamic leak flow model calculates the thermal conductivity to be about 0.1774 W/mK. When compared to the tabulated empirical data for the 10-bar column [66], a value of λ = 0.1774 W/mK at T = 286 K seems reasonable. Calculated by the use of the trendline given by figure 3.10, gives for the computed end temperature of 286 K:

$$\lambda = \big((0.5352 \cdot 286) + 23.298\big) \cdot 1e - 3 = 0.1774 \text{ W/mK}.$$

The total Δp due to source terms is computed to approximately 0.58 bar. Considering the simulated outlet pressure and density, this gives a calculated temperature of 286 K at the outlet, and the ΔT is then 7 K between the ambient and the outlet.

If the initial pressure is changed from 10 to 8 bar, the dynamic leak flow model will perform a linear interpolation between the two implemented trendlines for 1 and 10 bar to obtain λ. For 8 bar, the temperature at the outlet is still calculated as 286 K. The linear interpolation computation has been checked by hand by interpolating through the tabulated values. First, by finding λ corresponding to 286 K for both 1- and 10 bar. Then an interpolation between the pressure ranges was performed, and the interpolation gives a λ of 0.1795 w/mK, while the dynamic leak flow model computes 0.1771 w/mK.

The overall heat transfer coefficient, U, has been calculated for hand to be 0.004236 W/m^{2}K, and is computed by the dynamic leak flow model as 0.00424 W/m^{2}K.

The heat transfer for a ΔT = 7 K between the gas temperature and the ambient temperature is then calculated to be 13.2 W, while the simulated value is 12.8 W.

3.5.4 Minor losses

According to the obtained results from the simulations, the minor losses account for approximately 0.023 bar of the total Δp of 0.58 bar from the source terms. Each of the twenty bend's pressure drop can be observed in figure 3.16.

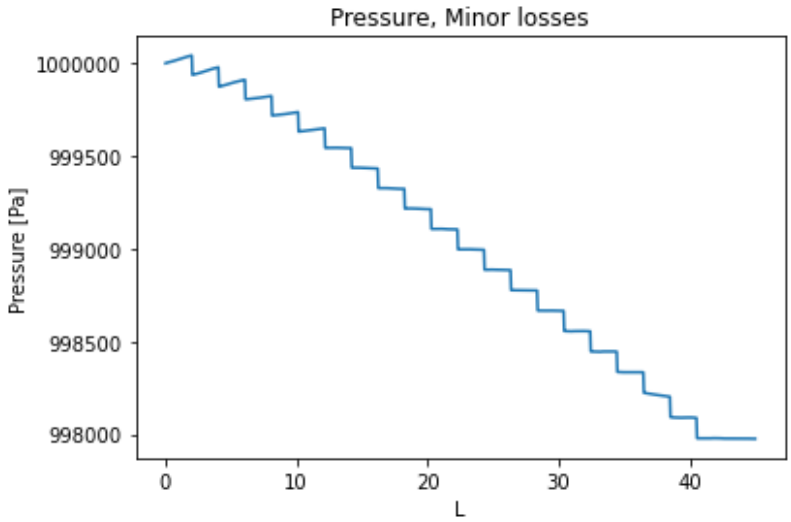

Figure 3.16: Simulation with Minor losses implemented as the only source term. Each "step" in the plot corresponds to one 90˚ bend. Initial conditions are in accordance with table 3.1.

With hand calculations, the total minor losses are calculated to be 0.0222 bar for twenty bends, and the Δp for each bend is calculated to be approximately 110 Pa. Compared with the hand calculations, the simulated results seem reasonable.

3.5.5 Friction source terms

To calculate the friction factor, the viscosity must be pre-calculated. This has been done equivalent to the thermal conductivity described in section 3.5.3, and the hand calculations correspond well with the model's estimated values.

Hand calculations for the friction factor using the Churchill correlation for values computed at the outlet seem to correspond with the computed values by the dynamic leak flow model. Hand calculation results in $f_{hand} = 0.0306$, and the computed value by the model is $f_{comp} = 0.0306$.

In addition, the Reynolds number and the relative roughness have been used to compare the friction factor with the Moody diagram [69]. As can be observed by the red line in figure 3.17, the Churchill correlation seems to give promising results for the friction factor. Here $Re \approx 25000$ and $\frac{\varepsilon}{D} = 0.0028$.

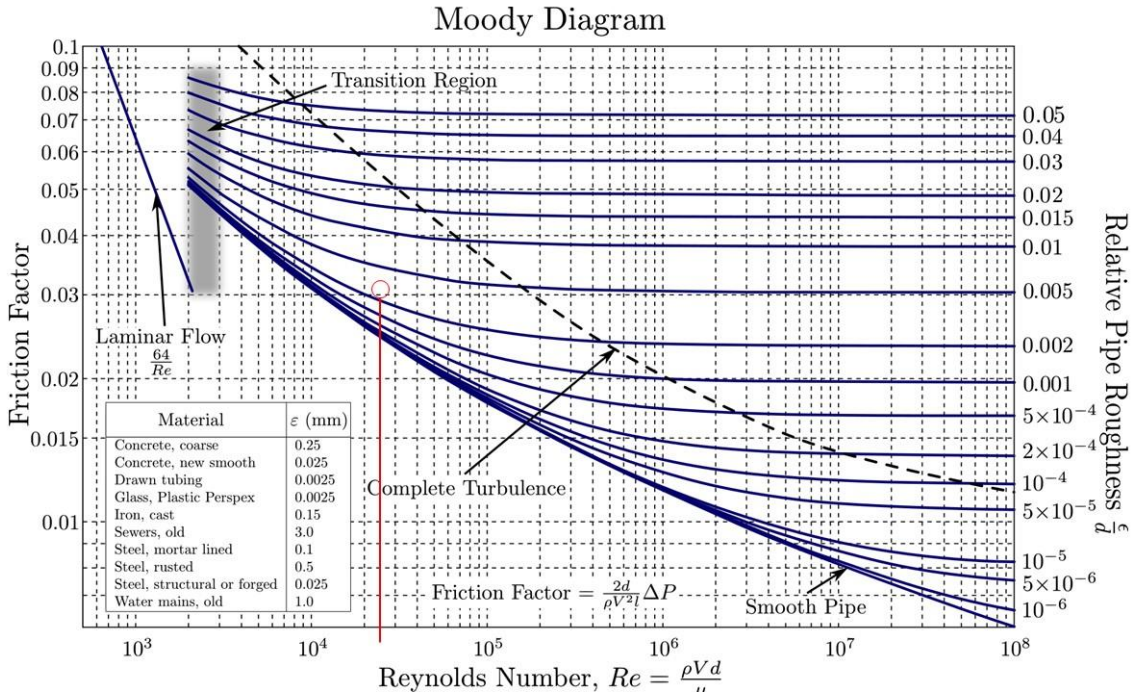

Figure 3.17: Moody Diagram [69]. The red line indicates the friction factor using the values: $Re \approx 25000$ and $\frac{\varepsilon}{D} = 0.0028$.

3.5.5.1 Pressure drop due to friction

The Δp is calculated by the term $\mathbf{C}_{fric} = \frac{f\rho|u|uL}{2D}$. With hand calculations, this results in a Δp of 0.566 bar for a pipeline length of 45 m. The simulated Δp due to friction is 0.525 bar for the whole pipeline length, which seems reasonable compared to the hand calculations.

3.5.5.2 Friction work

The friction work term in the energy equation alone accounts for a Δp of about 580 Pa in the total system. The results from the hand calculations of equation (3.112) indicate that the energy equation's friction work term is implemented correctly.

3.5.5.3 Leakage

The mass flow rate through the leakage orifice is calculated using equations (3.69-3.70) for sonic flow. A leakage orifice diameter of 1.00 mm has been considered. The hand calculations result in a leakage mass flow rate of 0.49 g/s, identical to what the model computes with the initial values.

3.6 Results

This section presents the results obtained from the simulations performed by the implemented dynamic leak flow model. First, a comparison between the two implemented flux limiters, Minbee and Superbee, will be presented. Then the calculated leakage mass flow rate for varying leakage orifice diameter will be presented. Finally, three simulation cases will be presented where the main purpose is to present how the model estimates the pressure drop and rarefaction waves due to a leak in the system. The results from the three cases have been limited to considering only the initial effects and the initial wave that occurs from the leakage.

The first case focuses on the total pressure drop measured from the inlet to the pipeline outlet. The simulations are performed with increasing leakage orifice diameters, from 0 – 6.0mm.

The second case considers the Δp, and the change in the mass flow rate that occurs due to a leak, measured at four different locations on the pipeline with increasing leak diameter orifice, 0.25mm – 6.00 mm.

The third case has been performed with varying inlet pressures from 2-10 bar and a leak orifice diameter of 0.5, 1.0, and 2.5 mm. All simulations have been performed assuming a sonic flow through the leakage orifice.

3.6.1 Comparison of Minbee and Superbee flux limiters

Simulations with both Superbee and Minbee as flux-limiters in the dynamic leak flow model have been performed with the initial conditions in accordance with table 3.1. Simulations have been run without any leakage source term but with all other source terms implemented. Results from the simulations indicate that the Superbee flux limiter is suffering from producing oscillations, which becomes especially noticeable for the density calculation. Simulation results plotted with time for Superbee and Minbee can be observed in Figures 3.18 and 3.19, and 3.20 and 3.21, respectively.

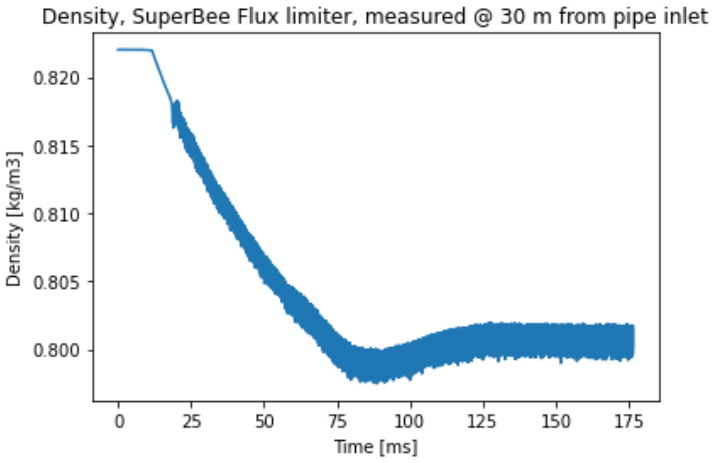

Figure 3.18: Density plotted with respect to time with Superbee flux limiter. The simulation is finished after 12200-time steps, and the inlet pressure is 10 bar. The inlet mass flow rate is 1.585 g/s.

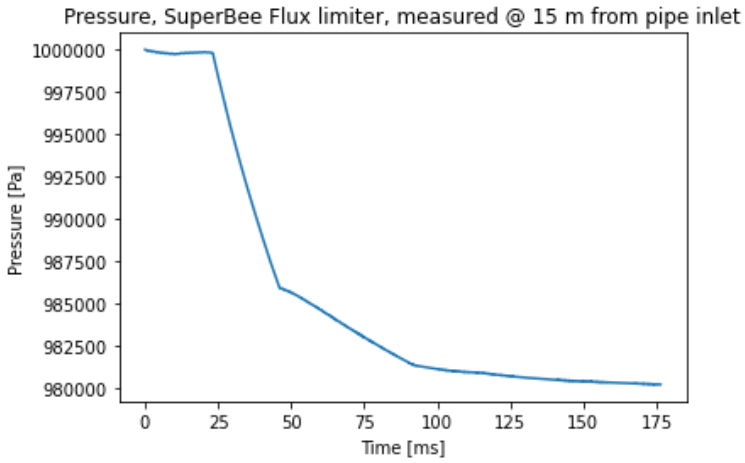

Figure 3.19: Pressure plotted with respect to time with SuperBee flux limiter. The simulation is finished after 12200-time steps, and the inlet pressure is 10 bar. The inlet mass flow rate is 1.585 g/s.

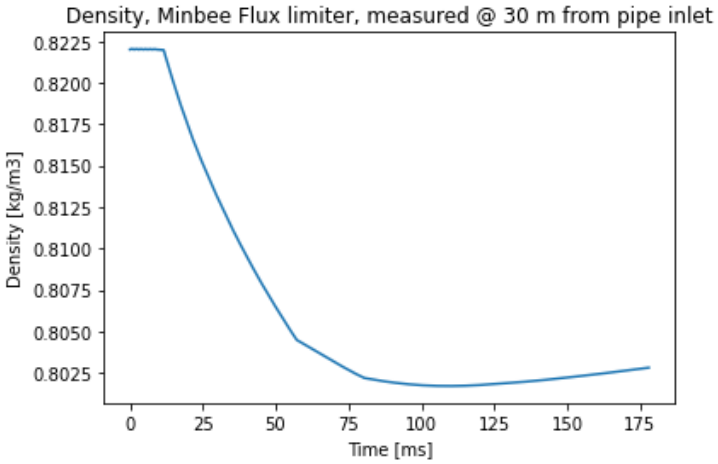

Figure 3.20: Density plotted with respect to time with Minbee flux limiter. The simulation is finished after 12200-time steps, and the inlet pressure is 10 bar. The inlet mass flow rate is 1.585 g/s.

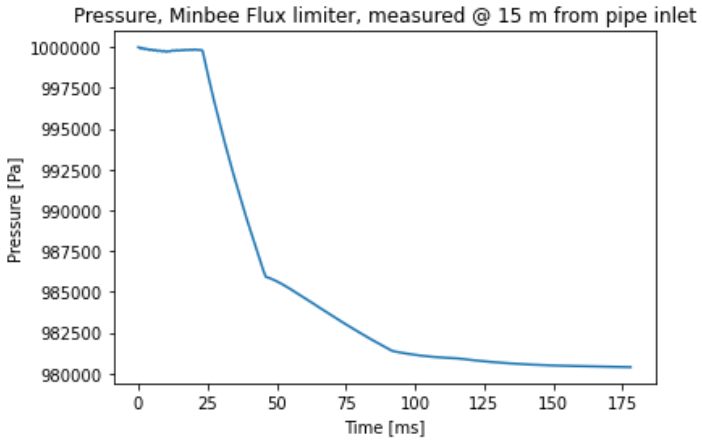

Figure 3.21: Density plotted with respect to time with Minbee flux limiter. The simulation is finished after 12200-time steps, and the inlet pressure is 10 bar. The inlet mass flow rate is 1.585 g/s.

The obtained results indicate that the model with both the mentioned flux limiters calculates identical pressure for the given simulation case. However, the oscillations produced in the calculation of the density seem to make a noticeable difference in the calculated density between Superbee and Minbee. Because of the challenge with oscillations produced by the Superbee flux limiter, all results in the further work during this study will be simulated with the Minbee flux limiter only.

3.6.2 Leakage mass flow rate with increasing leak orifice diameter

The leakage mass flow rate for orifice diameters from 0.25 – 6.00 mm has been plotted with the inlet mass flow rate. From figure 3.22, it follows that the leakage mass flow rate is equal to the inlet mass flow rate at a leakage orifice diameter of approximately 1.80 mm. This corresponds to a ratio between the leak orifice diameter and the cross-sectional pipe diameter, $\left(\frac{D_o}{D}\right)$, of 0.2, with a pipe diameter of 9 mm. The ratio $\left(\frac{D_o}{D}\right) = 0.2$ has been checked for diameters of $2 \cdot D$ and $3 \cdot D$ and correspond well to where the leak mass flow rate exceeds the inlet mass flow rate for L = 45 m and Nx = 2000.

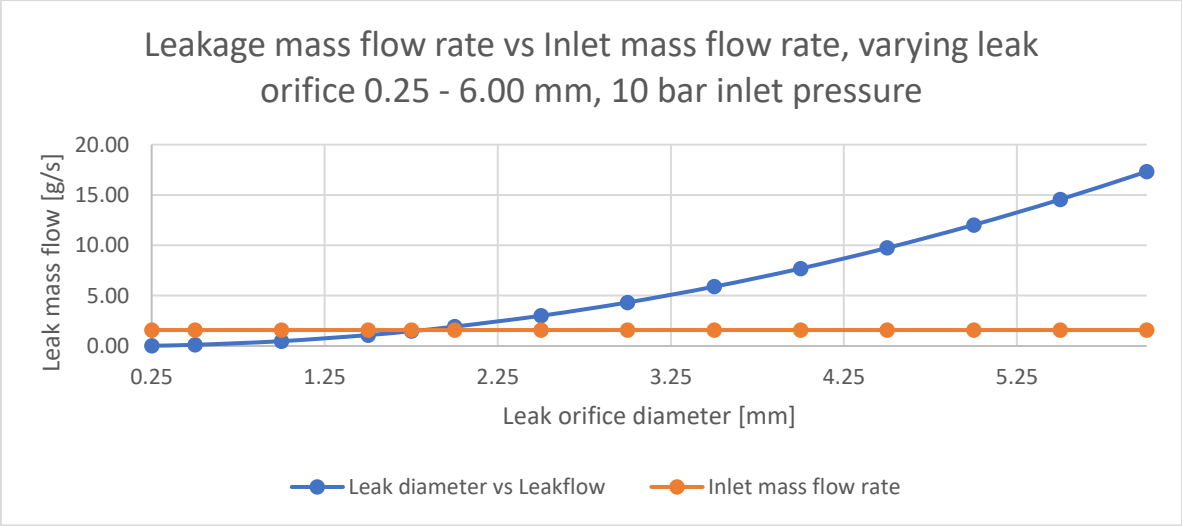

Figure 3.22: Plot of the leakage mass flow rate and the inlet mass flow rate with increasing leak orifice diameter simulated by the model. Inlet pressure 10 bar, Abel-Noble EOS.

3.6.3 Case 1 – Total Δp, measured from inlet to outlet

In case 1, simulations have been performed with a varying leakage orifice diameter from 0.25 mm and up to 6.00 mm, with a step of 0.25mm with both Abel-Noble EOS and the assumption of an ideal gas. The ICs from table 3.1 have been used, and the model is simulated until a steady state is obtained before the leakage is initiated. A code for storing the steady-state simulations for both ideal gas and Abel-Noble was implemented. The steady-state variables were stored after 30000 time steps and used as initial conditions for the further simulations. When starting the simulation in steady-state, the simulation run-time was 1350 time steps, and the leakage was initiated after 300 time steps. The resulting total pressure

drop from both Abel-Noble and Ideal gas, measured from the inlet to the outlet of the pipeline, has been plotted in MS Excel and is shown in Figures 3.23 and 3.24. The total calculated Δp without any leakage was approximately 0.58 bar for both EOSs. From figures 3.23 and 3.24, it can be observed that for a diameter between 1.0 -1.25mm, the effect of the leakage slightly starts to affect the total pressure drop. At a leakage orifice diameter of about 1.5 mm, the gradient for the Δp seems to change, resulting in a significant effect of the leakage on the total Δp. There is no significant difference in the calculated results between the Ideal gas assumption and the Abel-Noble EOS. The inlet pressure was set to 10 bar, and the inlet mass flow rate was 1.585 g/s.

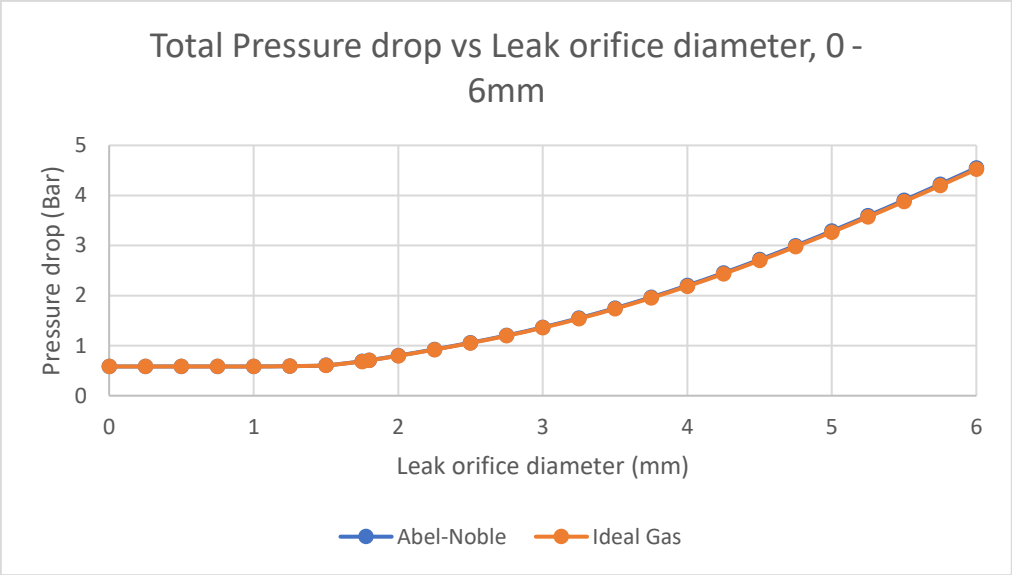

Figure 3.23: Total Δp obtained with both Abel-Noble and Ideal gas, measured from the inlet to the pipeline outlet. Inlet pressure: 10 bar. Inlet mass flow rate: 1.585 g/s.

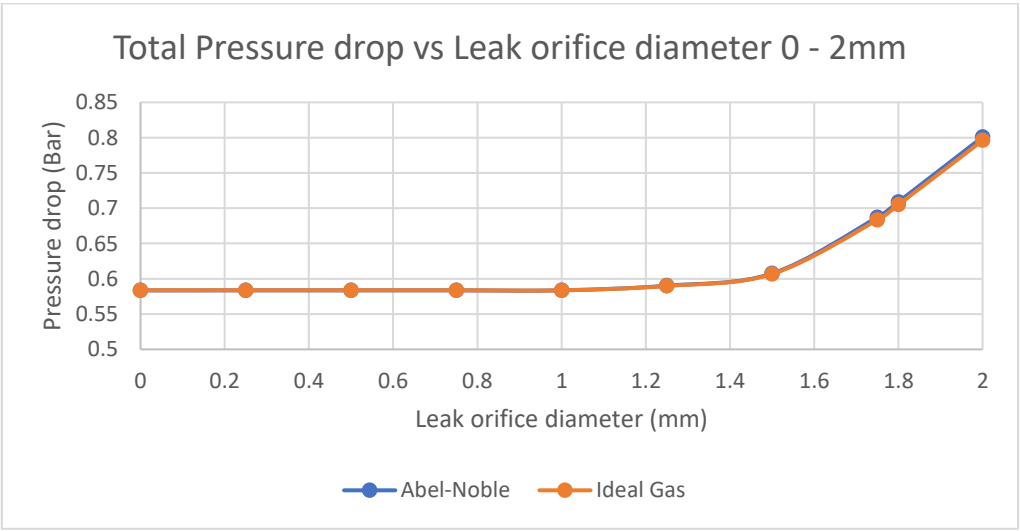

Figure 3.24: A closer view of the total Δp, with leak orifice diameters 0-2 mm, obtained with both Abel-Noble and Ideal gas, measured from the inlet to the pipeline outlet. Inlet pressure: 10 bar. Inlet mass flow rate: 1.585 g/s.

3.6.4 Case 2 – Pressure drop due to rarefaction wave, increasing leakage diameter

Four sensors have been simulated on the pipeline with equal spacing from the leakage point. Both pressure- and mass-flow sensors will be considered. The sensors are placed 7.5m, 15m, 30m, and 37.5m from the pipeline inlet. Values for initial conditions are simulated in accordance with table 3.1, and the stored steady-state values for both Abel-Noble and ideal gas from Case 1 have been utilized as starting point. The simulations are performed with 1350 time steps, and the leakage is initiated after 300 time steps. Case 2 will be focused on the Δp due to the rarefaction wave at the sensors and the resulting mass flow rate. The leakage orifice diameter has been varied in an equivalent method as in case 1, and the results for Δp have been plotted in MS Excel. In addition, plots for leakage orifice diameters of 1.00mm, and 1.80mm, will be presented.

Figure 3.25 and 3.26 indicates that for leakages with an orifice diameter larger than 2 mm, the Δp downstream is larger than the Δp upstream. PS1 & PS4 and PS2 & PS3 have identical distances from the leakage point, with PS1 & PS2 placed upstream and PS3 & PS4 placed downstream. Small discrepancies in the curve at 3.25 mm and 4.75 mm can be observed as a "dip" in the simulated pressure drop. This is probably due to inaccuracies in the manual readings of the results.

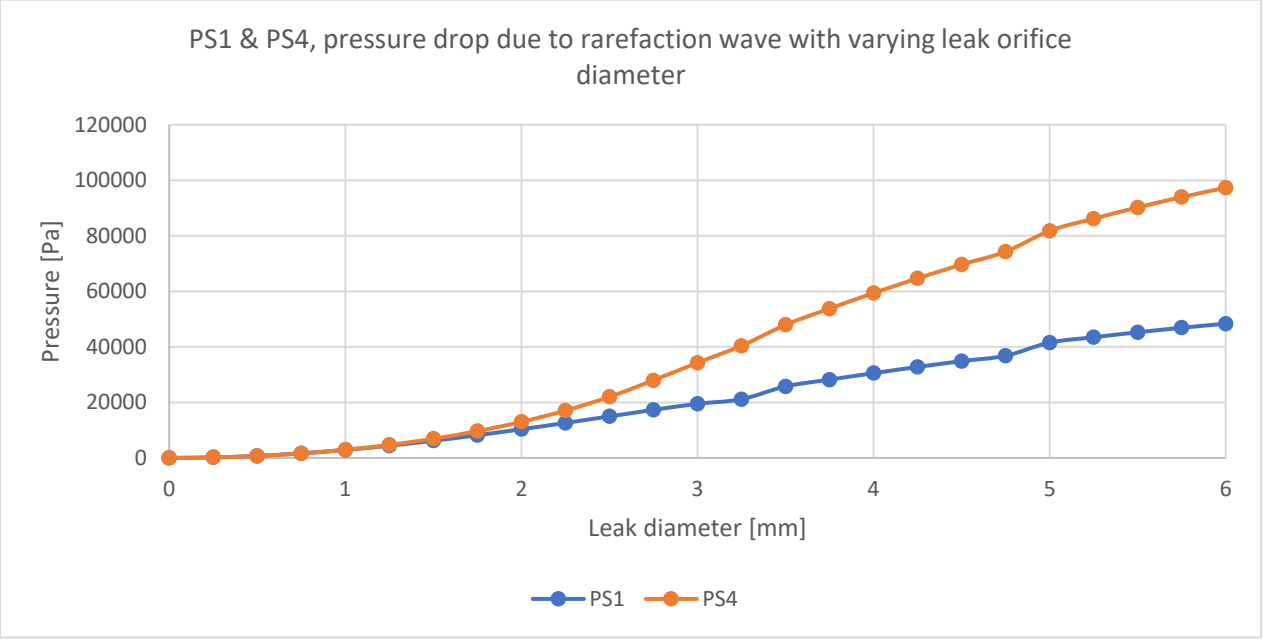

Figure 3.25: PS1 & PS4 Δp due to rarefaction wave plotted with increasing leak diameter. Inlet pressure 10 bar, mass flow rate: 1.585 g/s. Abel-Noble EOS.

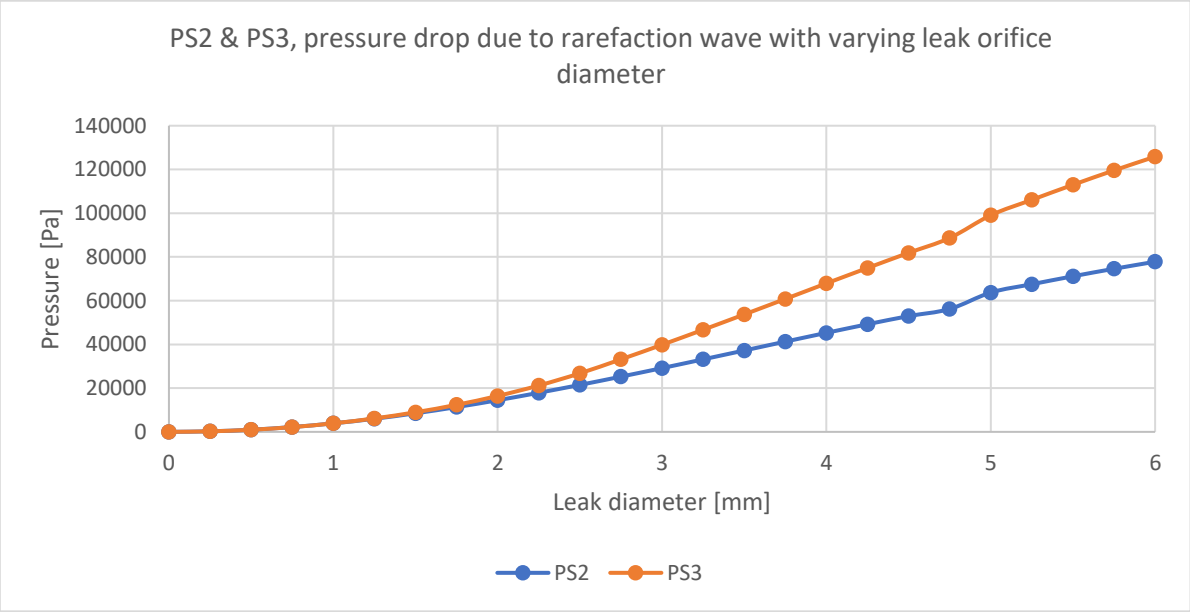

Figure 3.26: PS2 & PS3 Δp due to rarefaction wave plotted with increasing leak diameter. Inlet pressure 10 bar, mass flow rate: 1.585 g/s. Abel-Noble EOS.

A closer view of the results between 0 – 2 mm can be observed in Figures 3.27 – 3.28, where also results obtained with the ideal gas law are plotted. Here the results indicate that the effect of the difference in the pressure drop starts to occur at a leakage orifice diameter of approximately 1.25 mm. The magnitude of the rarefaction wave seems to be calculated about equally with both Abel-Noble and ideal gas. Abel-Noble estimates the pressure drop as slightly larger in magnitude than the ideal gas law, but it is not a significant difference.

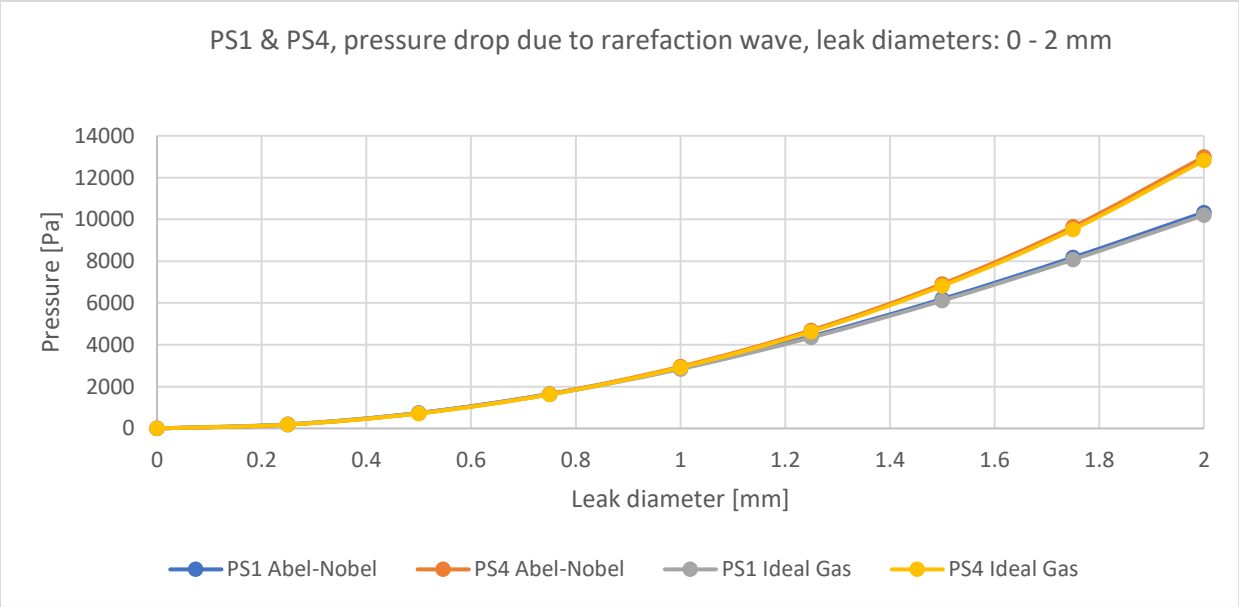

Figure 3.27: PS1 & PS4 Δp due to rarefaction wave plotted with increasing leak diameter, 0 – 2mm with both Abel-Noble and ideal gas law. Inlet pressure 10 bar, mass flow rate: 1.585 g/s.

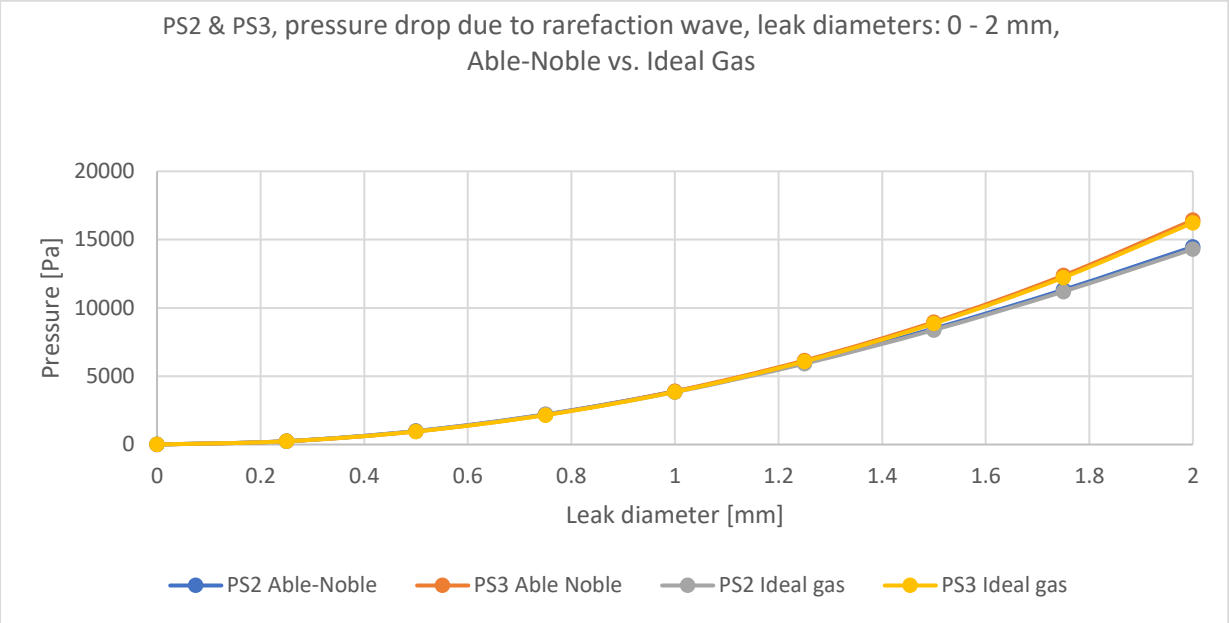

Figure 3.28: PS2 & PS3 Δp due to rarefaction wave plotted with increasing leak diameter, 0 – 2mm with both Abel-Noble EOS and ideal gas law. Inlet pressure 10 bar, mass flow rate: 1.585 g/s.

3.6.4.1 1.00 mm leakage orifice diameter

Figure 3.29 shows the different flow variables, density, velocity, pressure, and the total energy after 1350 time steps. At this moment, it can be observed that the initial waves are close to the endpoints of the domain and have passed the location of the sensors. The leak is located at 22.5 m, and it can be observed that the Δp due to the leakage has minimal impact on the total Δp measured from the inlet to the outlet of the pipeline. However, the velocity has a noticeable change at the leakage point, increasing the gas velocity upstream and reducing the gas velocity downstream.

From figure 3.29, it can be observed that the leakage points are barely noticeable. However, looking at the density calculations, it seems like there are some numerical instabilities at the point of leakage. Figure 3.30 and 3.31 shows a close-up view at the point of leakage for the pressure and the density for the same simulation as in figure 3.29. The instabilities only appear for the density calculations, where the density seems to obtain an overshoot, resulting in a larger magnitude at the point of leakage. The overshoot seems to disappear with the use of the ideal gas EOS, as shown in Figures 3.32 and 3.33. In figure 3.33, it can be observed some tendencies of oscillations near the point of leakage, but the overshoot is not present as in figure 3.31. This indicates that the model suffers from some numerical instabilities at the leakage point for the density calculation when utilizing the Abel-Noble EOS. A small drop in magnitude can be observed in figures 3.30 – 3.33 right before and after the leakage point. This is due to bend number 11 and 12, placed at 22.26 m and 24.29 m from the inlet with L = 45m, respectively.

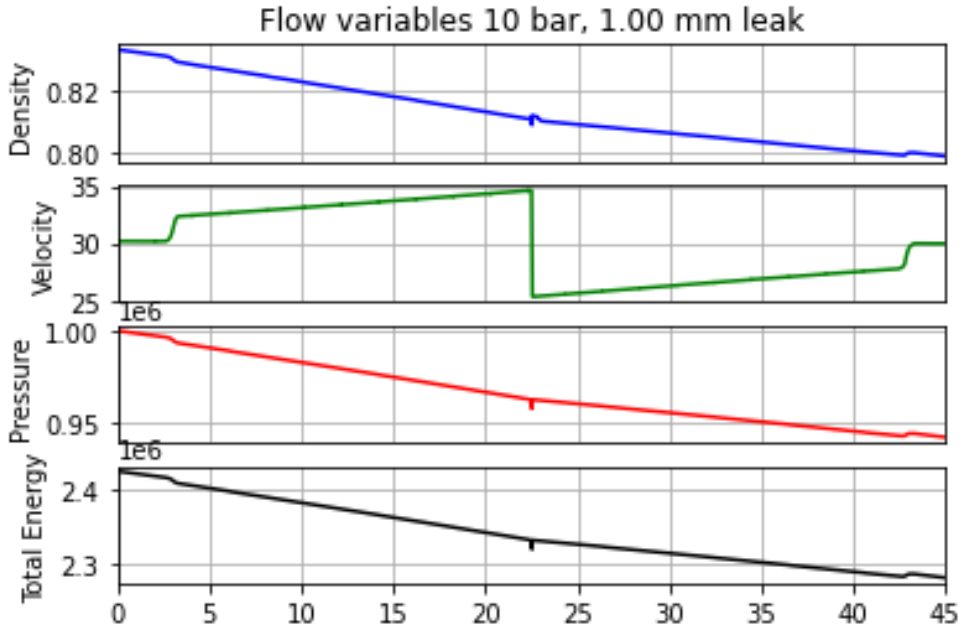

Figure 3.29: The density [kg/m^3], velocity [m/s], pressure [Pa], and total energy [J] plotted after 1350 time steps with leakage initiated after 300 time steps from inlet to outlet (0-45m) for the leakage model. Inlet pressure: 10 bar, leak diameter: 1 mm, inlet mass flow rate:1.585 g/s. Abel-Noble EOS.

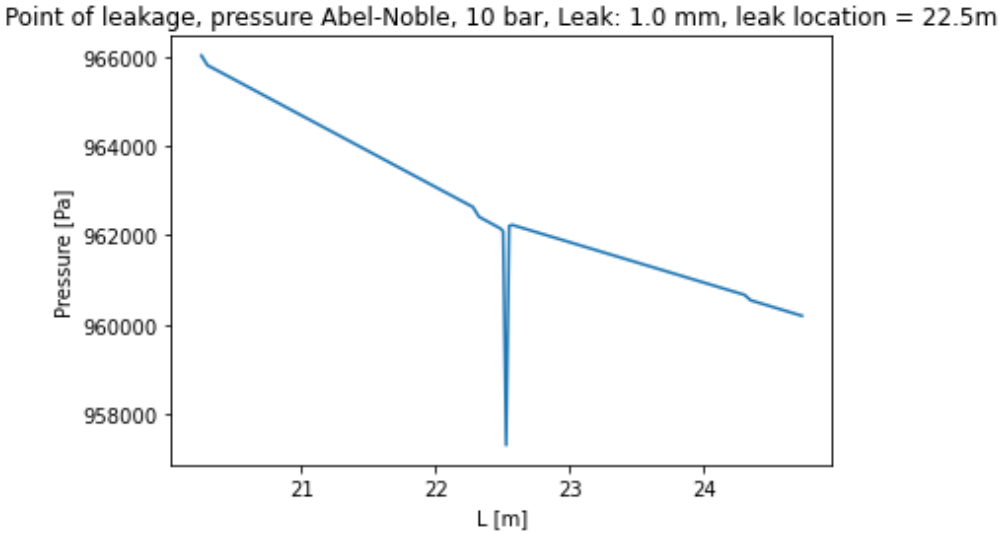

Figure 3.30: Close-up view of the pressure at the point of leakage after 1350 time steps. Abel-Noble EOS.

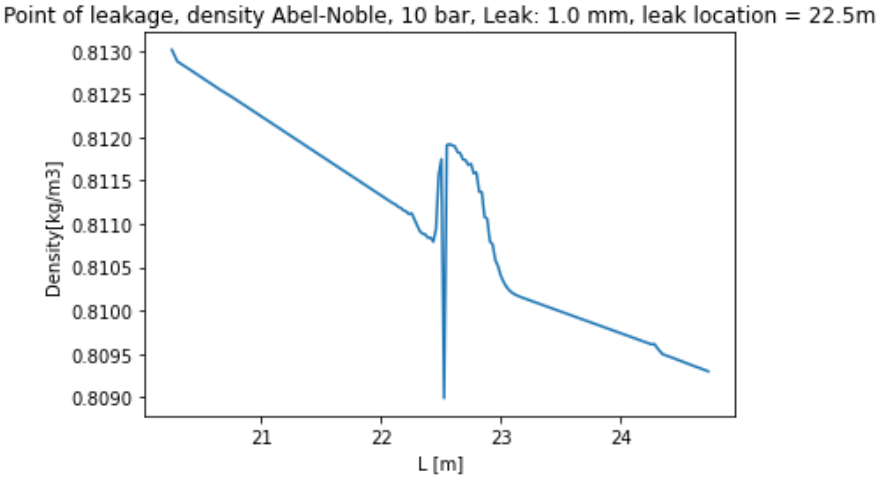

Figure 3.31: Close-up view of the density at the point of leakage after 1350 time steps. Abel-Noble EOS.

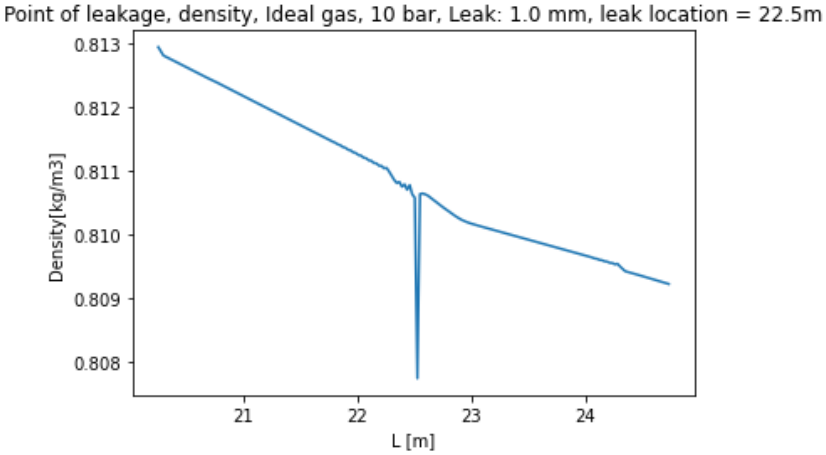

Figure 3.32: Close-up view of the pressure at the point of leakage after 1350 time steps. Ideal gas law.

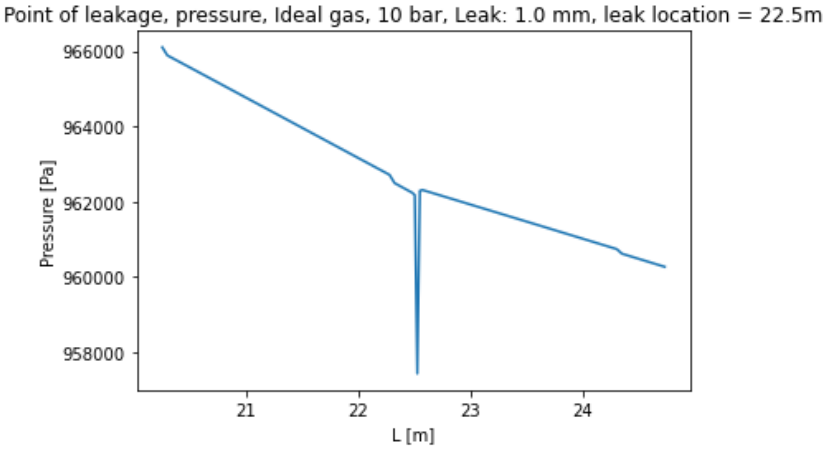

Figure 3.33: Close-up view of the pressure at the point of leakage after 1350 time steps. Ideal gas law.

Figure 3.34 shows the Δp at four different locations due to the rarefaction wave only. Δp_1 = 2880 Pa, Δp_2 = 3887 Pa, Δp_3 = 3901 Pa and Δp_4 = 2955 Pa for sensor location 1-4, respectively. Figure 3.35 shows the simulated Δp due to the rarefaction wave at PS1 with the Abel-Noble EOS with a Δp_1 = 2880 Pa. The simulation is finished after 1350-time steps, and the leak is initiated after 300-time steps.

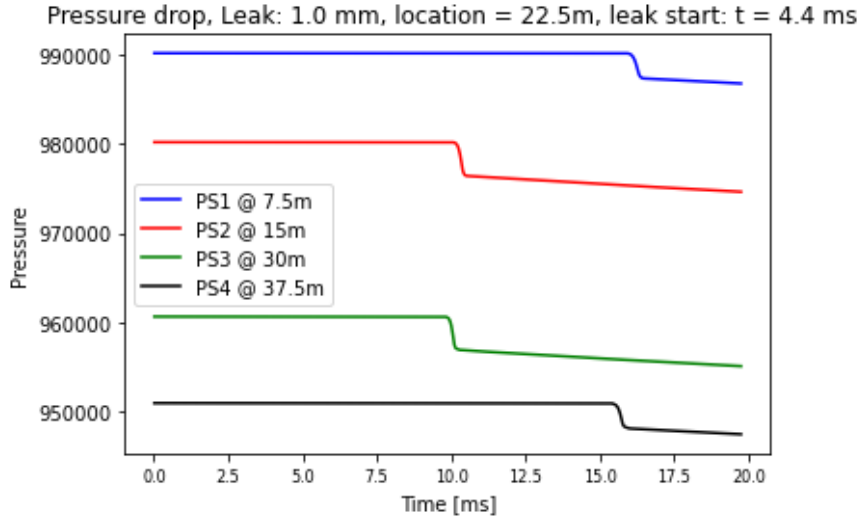

Figure 3.34: Δp [Pa] due to a rarefaction wave from a leak located at 22.5 m and plotted with respect to time. The leak is initiated after 300-time steps. The simulation is finished at 1350 time steps. Inlet pressure 10 bar. Inlet mass flow rate: 1.585 g/s. Abel-Noble EOS

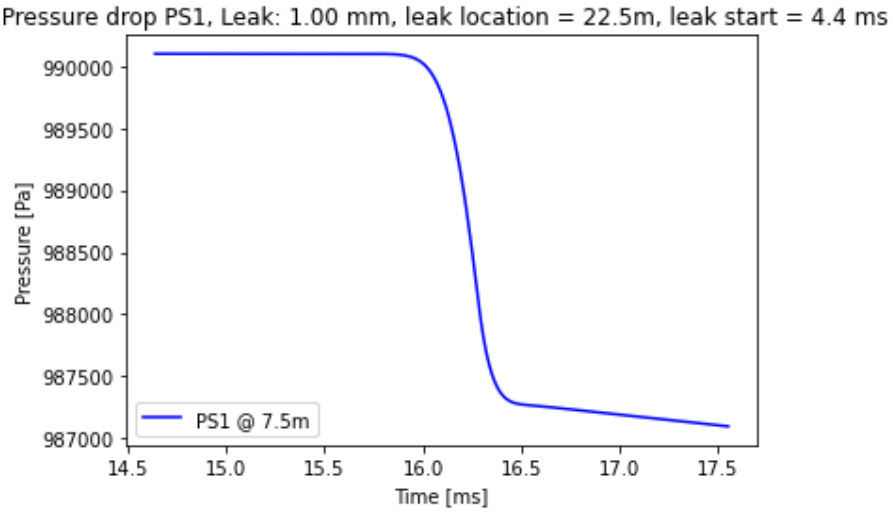

Figure 3.35: Δp at PS1 due to rarefaction wave only, located 7.5m from the pipeline inlet and plotted with respect to time. The leak is initiated after 300 time steps. The simulation is finished at 1350 time steps. Inlet pressure 10 bar. Inlet mass flow rate: 1.585 g/s. Abel-Noble EOS. Pressure drop = 2880 Pa.

Figure 3.36 shows the mass flow rates plotted with respect to time for the four sensor locations. The plot is from the same simulation as shown in figures 3.29-3.35. Sensors 2 & 3 are situated closest to the leakage point. Figure 3.36 indicates that the dynamic leak flow model estimates less change in the mass flow rate at the sensor furthest away from the

leakage point. A similar simulation has been performed with the same parameters as the simulations shown in figure (3.29-3.35), but without implementing source terms. This simulation can be observed in Figures 3.38 and 3.39. Here the change in mass flow rate and the Δp due to the rarefaction wave is constant at each sensor location. The dynamic leak flow model estimated the mass leaving the system to be approximately 0.49 g/s at the leakage point, and the behavior can be observed in figure 3.37. The mass flow in figure 3.37 is defined as negative in the plot to illustrate that the mass is leaving the system. From the start of the simulation, the mass flow rate of the leakage is zero until 300-time steps (4.4 ms), where the leakage is initiated.

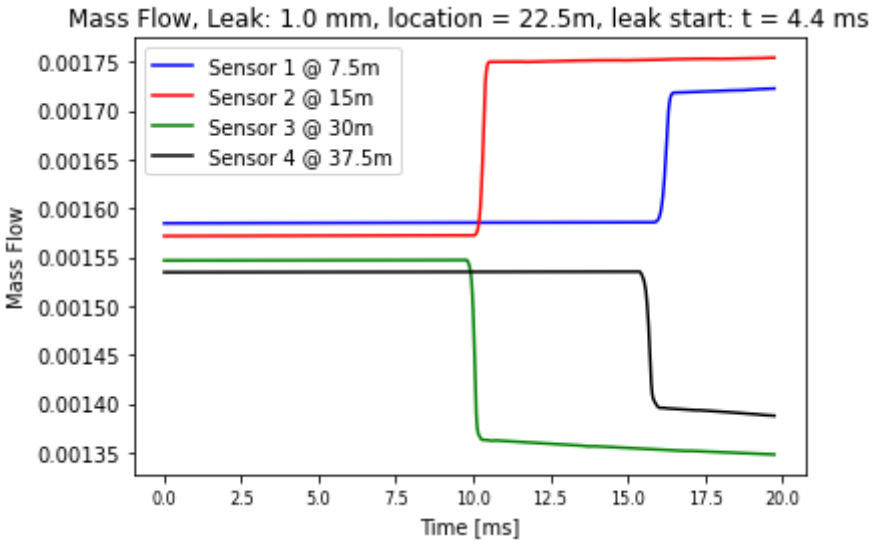

Figure 3.36: Mass flow rate [kg/s] measured at 4 different locations and plotted with respect to time. Inlet pressure 10 bar, Inlet mass flow rate 1.585 g/s.

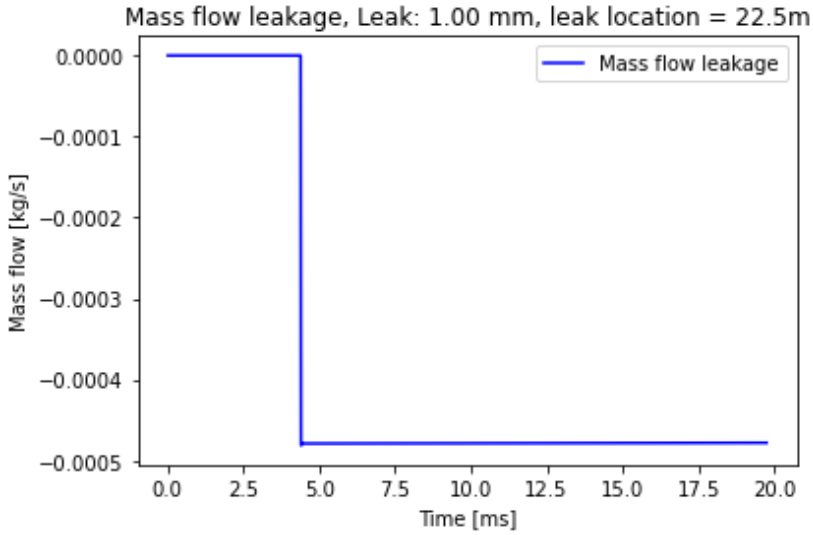

Figure 3.37: The leakage mass flow rate. Point of leakage = 22.5m, corresponding to L/2. Inlet pressure 10 bar, inlet mass flow rate 1.585 g/s. The flow rate is defined as negative in the plot as it leaves the system. Leak flow rate: 0.48 g/s. Abel-Noble EOS

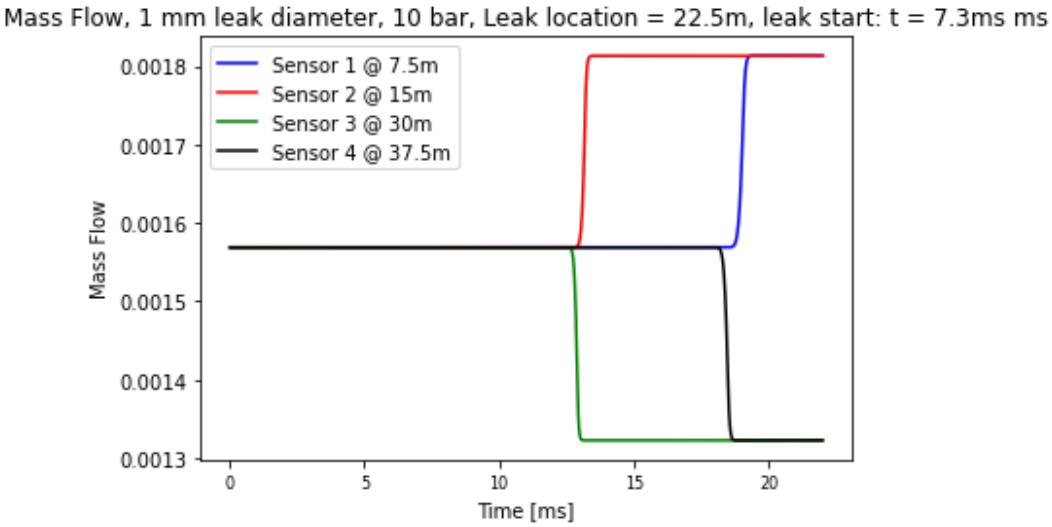

Figure 3.38: Mass flow rate [kg/s] measured at 4 different locations and plotted with respect to time. This simulation is performed without source terms implemented. Inlet pressure 10 bar, Inlet mass flow rate 1.585 g/s. Abel-Noble EOS

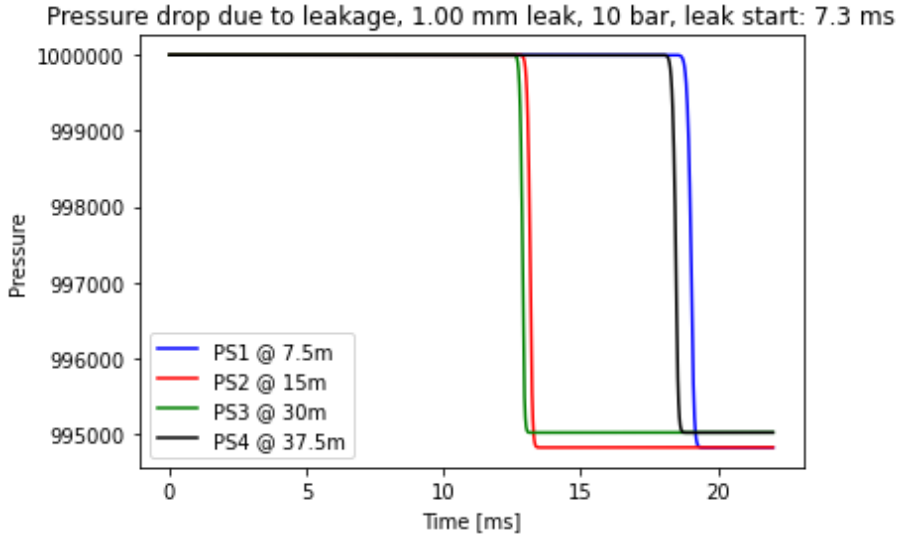

Figure 3.39: Δp measured at 4 different locations and plotted with respect to time. This simulation is performed without source terms implemented. Inlet pressure 10 bar, Inlet mass flow rate 1.585 g/s. Abel-Noble EOS,

3.6.4.2 2.00 mm leak orifice diamater

This simulation has been performed with a leakage diameter orifice of 2.00 mm and the Abel-Noble EOS. When the leakage orifice diameter is increased, the Δp from the leakage itself starts to impact the total Δp. From figure 3.40, it can be observed that the lowest total

pressure obtained after 1350 time steps is the pressure obtained at the leakage point. In addition, there is a significant change in the gas velocity at the leakage point.

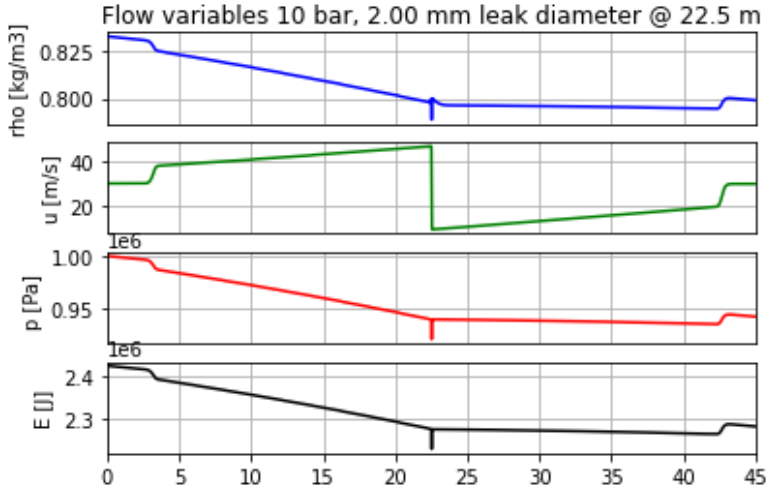

Figure 3.40: The density, velocity, pressure, and total energy plotted after 1350 time steps with leakage initiated after 300 time steps from inlet to outlet (0-45m) for the leakage model. Inlet pressure: 10 bar, leak diameter: 2.00 mm, inlet mass flow rate:1.585 g/s. Abel-Noble EOS.

For the simulation with a 2.00 mm leak orifice diameter, the same parameters as the simulation with a 1.00 mm leak are implemented. The only change in the simulation is the leak diameter orifice which has been doubled. Figure 3.41, 3.42, and 3.43 indicates that an increased leakage diameter from 1.00 mm to 2.00 mm results in larger rarefaction waves at the pressure sensors and a larger change in the mass flow rate. The Δp due to the rarefaction wave as shown in figure 3.41 corresponds to $\Delta p_1 = 10329$ Pa, $\Delta p_2 = 14471$ Pa, $\Delta p_3 = 16427$ Pa, and $\Delta p_4 = 12987$ Pa for the four sensor locations. Comparing the rarefaction wave in figure 3.42 with the rarefaction wave in figure 3.35, it can be observed that an increase from 1.00 mm to 2.00 mm leads to an almost 3.6 times larger Δp due to the rarefaction wave.

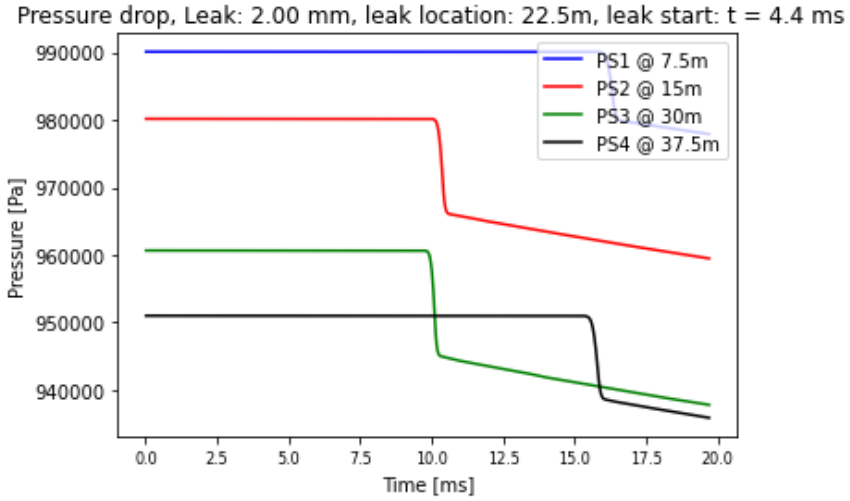

Figure 3.41: Δp due to rarefaction wave measured at four different locations. Inlet pressure: 10 bar. Inlet mass flow rate = 1.585 g/s. 2.00mm leak orifice diameter. The plot considers the state after 1350 time steps with Abel-Noble EOS.

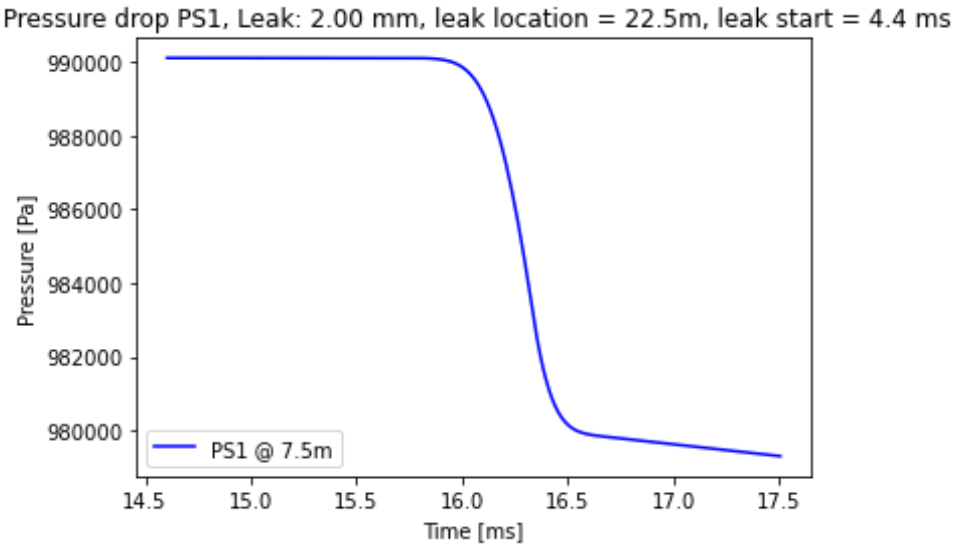

Figure 3.42: Δp at PS1 due to rarefaction wave only, located 7.5m from the pipeline inlet and plotted with respect to time. The leak is initiated after 300 time steps. 2.00 mm leak orifice diameter. The simulation is finished at 1350 time steps. Inlet pressure 10 bar. Inlet mass flow rate: 1.585 g/s. Abel-Noble EOS. Pressure drop = 10329 Pa.

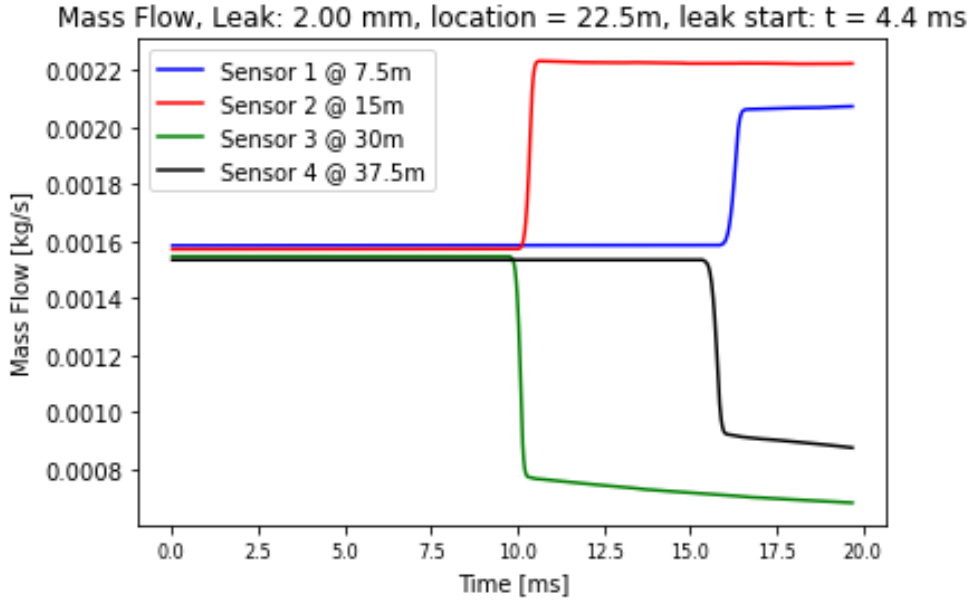

Figure 3.43: Mass flow rate measured at the four sensors 1-4. Inlet pressure: 10 bar. Inlet mass flow rate: 1.585 g/s. The plot considers the state after 1350 time steps. Abel-Noble EOS.

Figure 3.44 presents the mass flow rate at the point of leakage estimated by the dynamic leak flow model, and the obtained results are plotted with time on the x-axis. With a leakage orifice diameter of 2.00 mm, the estimated leakage mass flow rate is approximately equal to the inlet mass flow rate. The estimated leakage mass flow rate is approximately 1.92 g/s, which is higher than the inlet mass flow rate of 1.585 g/s.

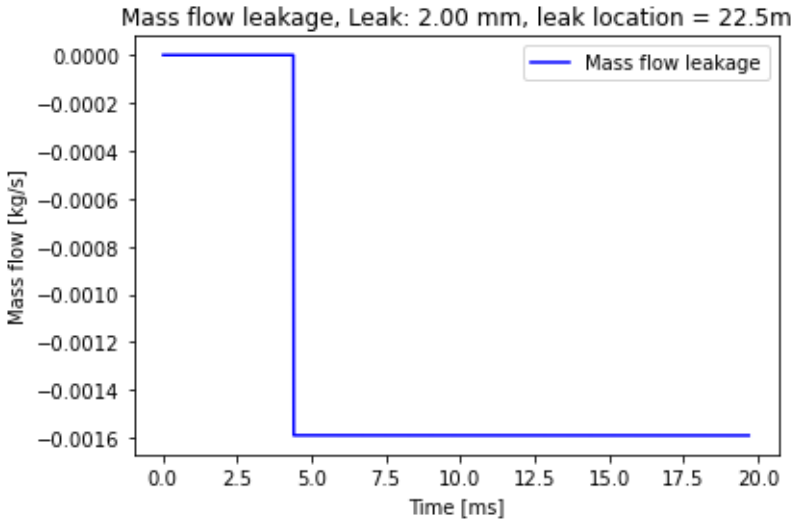

Figure 3.44: Mass flow rate at the leakage point plotted with time. Leak start: 4.4 ms, 10 bar inlet pressure. Inlet mass flow rate: 1.585 g/s. Leak mass flow rate: 1.924 g/s. The plot considers the state after 1350 time steps with Abel-Noble EOS.

3.6.5 Case 3 - Varying pressure, with a leakage orifice diameter of 0.5 mm, 1.0 mm, and 2.5 mm.

This section will present results obtained from simulations with varying inlet pressure and the Abel-Noble EOS. Simulations have been performed with pressures from 2 – 10 bar. The pressure ranges, 2 - 10 bar, have been simulated with three different leak orifice diameters 0.5 mm, 1.0mm, and 2.5 mm. The corresponding inlet density has been calculated with the Abel-Noble EOS, utilizing the actual simulated inlet pressure from 0 – 2 bar and the inlet gas velocity constant at 30 m/s. Other necessary parameters have been kept in accordance with table 3.1. Since the inlet conditions are different from the previous simulations, the stored steady-state files are not applicable. The run-time must be increased to reach a steady state before the leakage is initiated. All the simulations performed in Case 3 are finished after 15150 time steps, and the leakage is initiated after 14000 time steps.

3.6.5.1 0.5 mm leak orifice, varying pressure

With a leak orifice of 0.5mm, the change in pressure due to the rarefaction wave is quite equal for the sensors of equal distance from the point of leakage, as observed in figure 3.44. The Δp seems to have an approximately linear relationship with increasing pressure. A tendency of increased difference in Δp between the equally spaced sensors from the leakage point seems to occur as the pressure increases. This can be observed in figure 3.45 for the simulation with 10 bar, where Δp for PS2 at 10 bar is estimated as higher than its corresponding sensor downstream PS3.

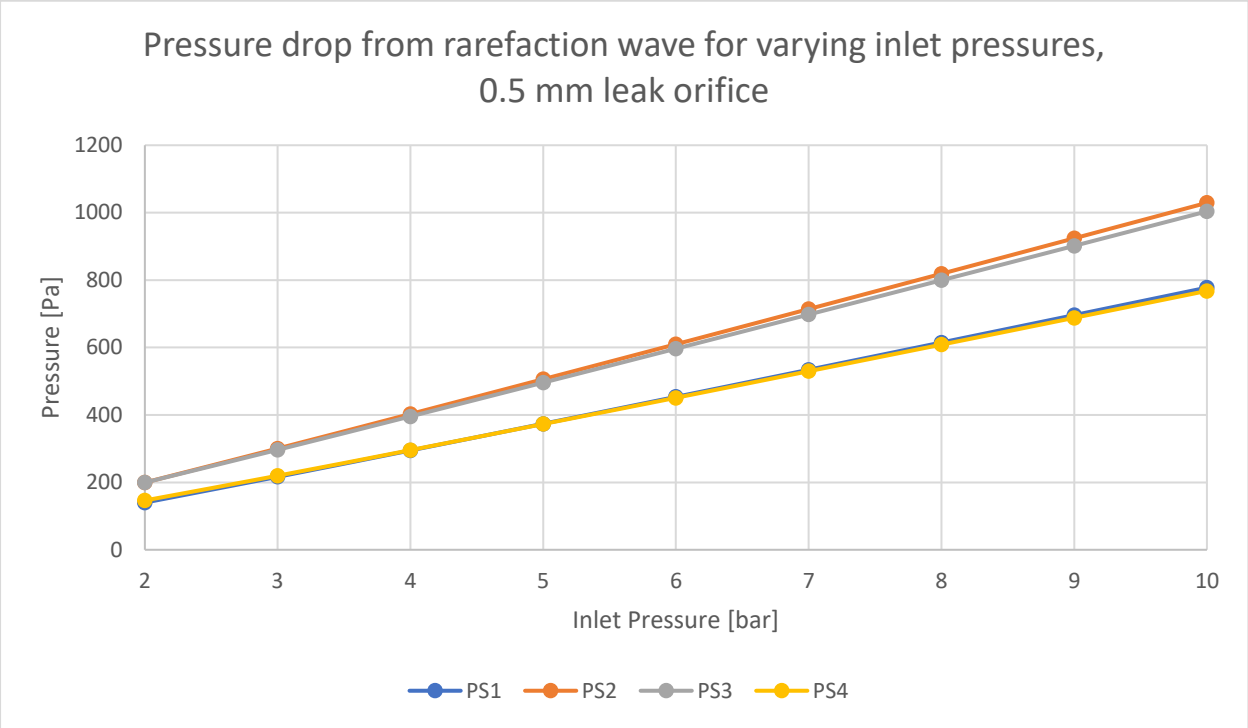

Figure 3.45: Simulations with varying pressure from 2 – 10 bar, Δp due to rarefaction wave only, 2.5 mm leak orifice diameter located 22.5 m from the inlet. The simulation is finished after 15150-time steps, and the leakage is initiated after 14000 time steps. Abel-Noble EOS.

3.6.5.2 1.0 mm leak orifice, varying pressure

The results obtained from the dynamic leak flow model for the 1.0mm leakage orifice diameter are shown in figure 3.46. A similar linear relationship as the simulation with 0.5 mm leakage orifice diameter is obtained. However, the pressures PS1 & PS4 seem to differ, where PS4 has a larger Δp for the whole specter of the simulated pressures. In addition, PS2 and PS3 are estimated by the model to have almost identical Δp due to the rarefaction wave for all the simulated pressure ranges.

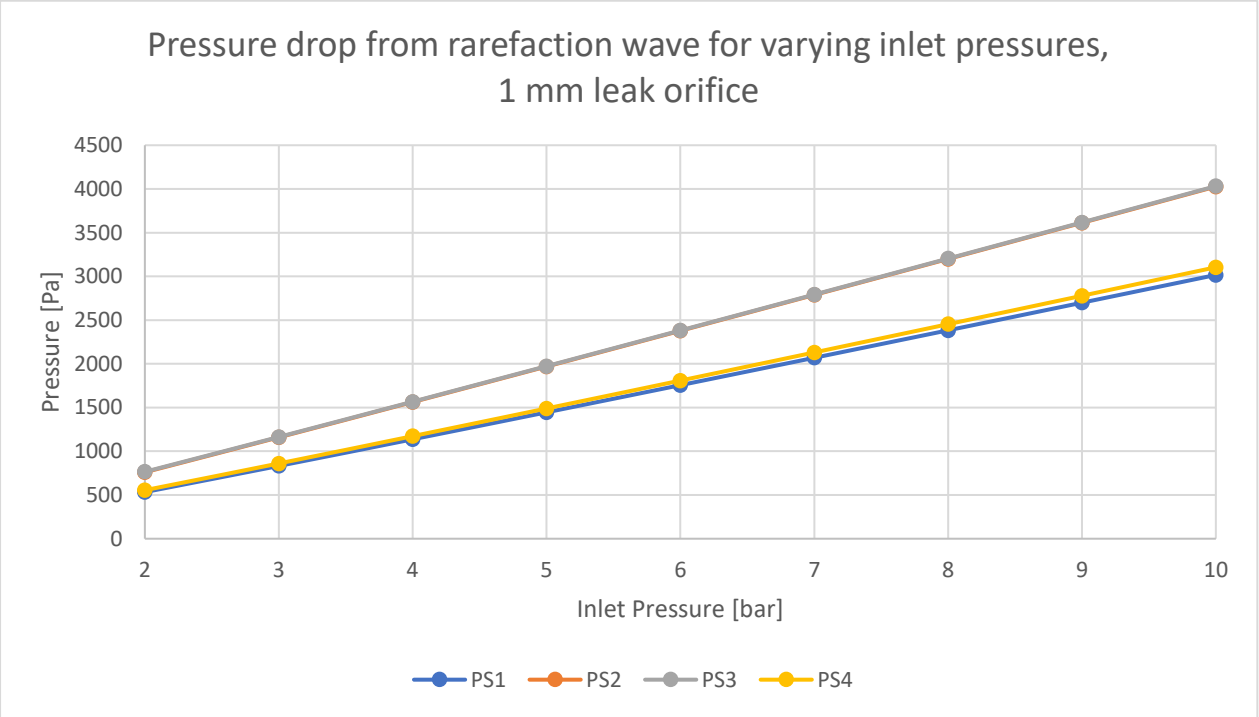

Figure 3.46: Simulations with varying pressure from 2 – 10 bar, Δp due to rarefaction wave only, 1.0 mm leak orifice diameter located 22.5 m from the inlet. The simulation is finished after 15150-time steps, and the leakage is initiated after 14000 time steps. Abel-Noble EOS.

3.6.5.3 2.5 mm leak orifice, varying pressure

The results estimated by the dynamic leak flow model for a leakage orifice diameter of 2.5 mm, seem to differ from the results obtained in Figures 3.45 and 3.46. In figure 3.47, the simulated results can be viewed, and the results indicate a significant difference in the Δp between the sensors located upstream and the sensors located downstream. The difference in the Δp between the equally spaced sensors is larger than in the previous simulations with 0.5 and 1.00 mm. Δp downstream is larger for PS3 & PS4 than upstream for PS1 & PS2, and this relationship seems to follow for all the simulated pressures. The pressure difference between the equally spaced sensors from the leakage point seems to increase with increasing pressure, e.g., the difference in Δp between PS1 and PS4 increases with increasing pressure.

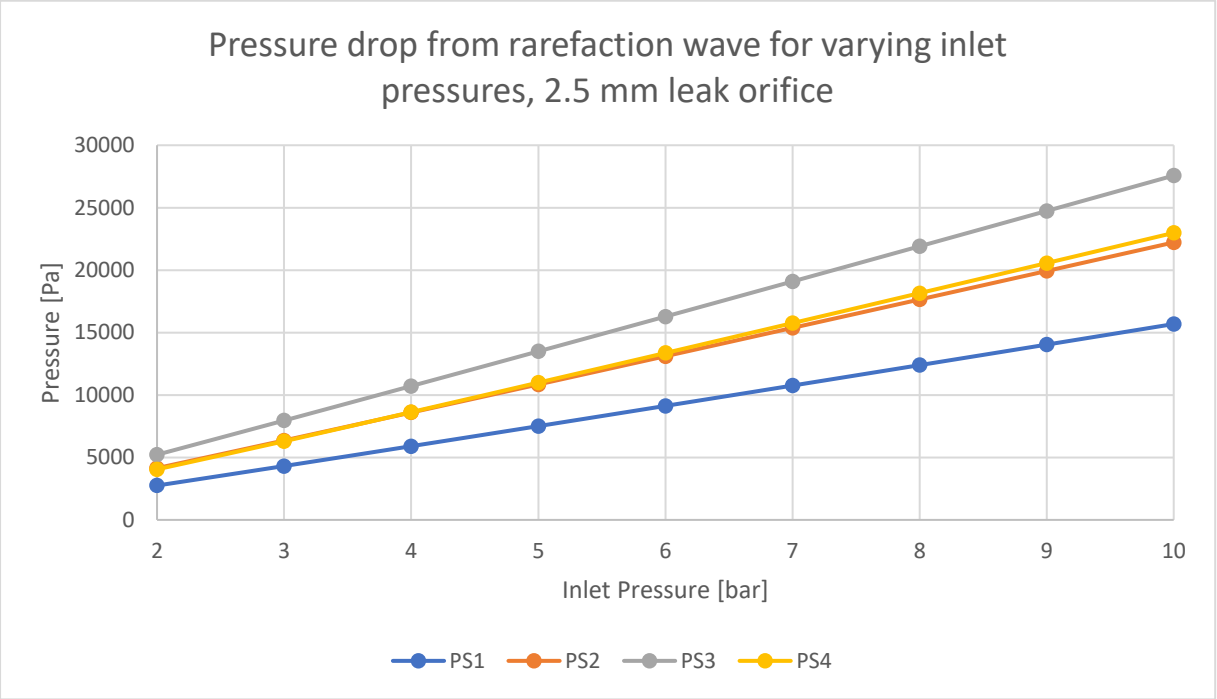

Figure 3.47: Simulations with varying pressure from 2 – 10 bar, Δp due to rarefaction wave only, 2.5 mm leak orifice diameter located 22.5 m from the inlet. The simulation is finished after 15150-time steps, and the leakage is initiated after 14000-time steps. Abel-Noble EOS.

3.7 Discussion

In Part Two of this study, a one-dimensional dynamic leak flow model is implemented with the system of non-linear hyperbolic conservation laws described by equations (3.31, 3.34-3.35). Finite difference methods are well known as good approximations for modeling one-dimensional pipeline flow. A 2nd- order accurate FLIC scheme, in a conservative form, was chosen as a finite difference scheme for approximating the partial derivatives. The FLIC scheme is found by Toro [40] to be less accurate compared to, e.g., an upwind TVD method. But the FLIC scheme is considered more accurate than a regular 1st-order scheme, as it does not overshoot as can happen with an upwind scheme, there is no need to consider the Riemann problem, it is less computationally expensive, simpler to implement, and it is able to capture rarefaction waves. Therefore, the FLIC scheme appeared as a great compromise and was chosen for this study.

From section 3.5.1, which considers validation of the dynamic leak flow model with the use of *test 2*, it can be observed that the implemented model is capable of simulating rarefaction waves. The results from *test 2* also indicate that the model is a bit diffusive. The results from the implemented FLIC scheme indicate that the scheme has a stable behavior and does not obtain spurious oscillations as non-TVD 2nd -order schemes. The grid spacing between the cells has been constant, dx = 0.0225m, for the simulations. This is considered a compromise between computational speed and accuracy.

The developed dynamic leak flow model seems to correctly estimate the equations for the implemented source terms according to the hand calculations. The pressure drop due to friction has a small difference between the models' estimated results and hand calculations. However, during the simulation, new values for the velocity, density, and friction factor, are calculated for each time step. The hand calculations and the simulation are both calculated for the whole domain. Considering that the simulations estimate new values for each time step that can differ from the initial conditions, the small divergence between the simulated and calculated result must be considered reasonable.

In the dynamic leak flow model, the Abel-Noble EOS has been implemented. From the literature review, it is found that a real-gas model should be used for pressures above 10 MPa. Due to the low pressures considered in this study, the ideal gas law would likely have performed just as well as the Abel-Noble and been a sufficient choice. However, implementing a real-gas EOS was believed to make the model more versatile if higher pressures were to be investigated. In figure 3.1, one can observe that the deviations from the ideal gas law start before 10 MPa but are most noticeable for higher pressures. The results from the simulations indicate no significant difference in the calculated results between Abel-Noble and the ideal gas law. Magnitudes of the pressure drop are slightly larger with the Abel-Noble EOS than calculated with the ideal gas assumption. This is as expected because the pressure is divided by $(1 - \rho b)$ during the calculations, which is smaller than one in magnitude.

An overshoot at the point of leakage for the density calculations was identified with the Abel-Noble EOS with a leakage orifice diameter of 1.00 mm, as shown in figure 3.31. When simulations were run for larger leak diameter orifices, D_o > 3.5 mm, the overshoot seems to be less noticeable. This overshoot was not present with simulations performed with the Ideal

gas law, indicating that the Abel-Noble co-volume constant might induce some numerical instabilities at the leakage point. Apart from the leakage point, the density calculations seem reasonable for the rest of the domain. Investigating other values of the Abel-Noble co-volume constant might result in more stable calculations. Another possible uncertainty is the authors' limited experience in writing programming scripts, indicating that there might be discrepancies in the code leading to such numerical instabilities.

Instead of implementing an already established empirical correlation for calculating the viscosity and the thermal conductivity for hydrogen, empirical data from the website [66] have been used to calculate trendlines for the pressures 1, 10, 50, and 100 bar. From this, it follows that there is an uncertainty if the pressures are below 1 bar and above 100 bar. A simplification has been made in the model: if the pressures are below 1 bar, the trendline for 1 bar will be used for calculations. Likewise, if the pressure exceeds 100 bar, the trendline for 100 bar will be used for calculations. For this current study, only pressures up to 10 bar have been considered, and therefore implementing trendlines for pressures higher than 100 bar in the model seemed unnecessary. Comparing the estimated values to the empirical data, the utilization of the trendlines seems to work well. If the work pressure is defined as, e.g., 8 bar, the model will perform a linear interpolation between the trendlines for 1 and 10 bar. The hand calculations for the 8 bar showed some difference between the estimated values. However, one might think that the model's estimated result is more accurate as two linear interpolations were performed for the hand calculations, compared to only one necessary interpolation performed by the model.

Two flux limiters have been implemented in the dynamic leak flow model, where the Superbee flux limiter shows oscillatory behavior for the calculations. This might be due to the multiple source terms implemented, as the Superbee flux limiter seemed stable when simulated with *test 2*. In addition, Vågsæther et al. [70] experienced oscillating behavior with Superbee during their study. Therefore, the Minbee flux limiter has been utilized as the primary flux limiter during the simulations. The Minbee flux limiter is more diffusive than the Superbee would have been. However, it does not obtain oscillations and shows a stable behavior. This is probably due to the nature of the Minbee flux limiter, which obtains a monotone 1st order accurate scheme at sharp gradients, while the Superbee flux limiter is claimed to keep the 2nd order accuracy [65]. The Minbee flux limiter has shown stable behavior for every different simulation case that has been performed during this study.

The modeling of the leakage point has been performed with the use of isentropic relations and the well-known choked flow theory, with the assumption of a sonic flow ($Ma = 1$) at the leak orifice. An assumption of isentropic relations through the leakage orifice is widely used in the literature and well known. At some point, the estimated leakage mass flow rate will become larger than the inlet mass flow rate, and over time such a large leak will become unphysical. Initially, it is possible with a larger leak flow rate than inlet flow rate, as long as there is enough available mass in the pipeline. According to the results obtained from the simulations, the leakage flow rate exceeds the pipeline mass flow rate when the leakage orifice diameter is larger than 1.8 mm with the design parameters from table 3.1. This corresponds to a ratio between the leak orifice diameter and pipe diameter, $\frac{D_o}{D} > 0.2$. This ratio may vary as different parameters are varied, e.g., *Nx* and the pressure.

If the pipeline is completely filled with gas, it consists of 2.35 g H_2 by considering the design parameters. For a leak orifice diameter of 6.00 mm, the model calculates the leak mass flow rate to be 17.31 g/s and the inlet mass flow rate of 1.58 g/s. The run-time of the simulations with the leakage initiated is approximately 15 ms. The leak time of 15 ms corresponds to a lost mass of 0.260 g, which is less than the mass content inside the pipeline. This indicates that such large leaks are physical at an initial phase but will become unphysical with time as the inlet mass flow rate is not large enough in magnitude to keep the pipeline filled with gas. The pressure drop that occurs in the pipeline will likely reduce the leakage mass flow rate with time, but this has not been investigated any further in this study.

In this model, nothing is limiting the gas flow rate at the inlet of the pipeline, leading to an increase in the mass flow rate upstream of the leakage point when leakages occur. The velocity upstream of the leakage will stabilize at a larger magnitude than the initial conditions. However, this is probably not a realistic behavior for a gas fuel supply system, as the flow most likely is controlled by a flow regulator at the inlet of the pipeline, which would have constricted the increase in the pipeline flow considerably. On the other hand, one could think that the flow regulator and the control system of the fuel cells would have noticed the lack of gas flow as a lack of power and might increase the flow to try to keep up with the desired power requirement. Such a scenario shows the importance of a working leak detection system. A regulator that increases the mass flow rate when there is a sudden decrease in the fuel delivery would lead to a larger leakage than necessary and possibly have severe consequences.

Figures 3.23 and 3.24 indicate that for a leak orifice diameter larger than 1.5 mm, the gradient of the pressure drop seems to change and become sharper. This is also where the leakage mass flow rate is about to be equal to the inlet mass flow rate. The reason for this change in the gradient might be that the velocity is increasing significantly in magnitude to fulfill the continuity equation, and an increased pressure drop is obtained due to the increase in velocity.

The simulated results from Case 2 and Case 3 indicate that the pressure drop due to the rarefaction wave and the change in the mass flow rate has a larger change downstream of the point of leakage than upstream. Figure 3.25 and 3.26 indicates that the difference between the pressure drop upstream and downstream is dependent on the leakage orifice diameter. Figures 3.27 and 3.28 show that the difference in pressure drop between upstream and downstream occurs at a leakage orifice between 1.00 - 1.25 mm, but figure 3.44 indicates that this effect is present already with a leak orifice diameter of 0.5mm. A similar simulation was performed without implementing the source terms in the model. This led to a constant change at all four sensors, which can be viewed in figures 3.38 and 3.39, indicating that the difference between the sensors is obtained due to the source terms. These results seem reasonable as the pressure is already lower downstream due to the source terms. The propagating wave must work against a higher pressure upstream of the leakage point, resulting in a “flattening” effect. Another observation from the results is that the ratio of change in flowrate seems to be larger than the ratio of change in the pressure due to the rarefaction wave. Therefore, a leak detection system based on the detection of a change in the flow rate rather than the pressure drop might be advantageous.

3.8 Conclusion

In part two of this study, a literature review on relevant equations of state has been performed, and a dynamic leak flow model considering the effects of a leakage has been developed. In order to develop the model, relevant theory have been presented.

From the literature review in Part Two, it is found that there exist several different equations of state that is relevant and might could have been used in this study. Regarding that the pressures considered in this study are only 10 bar and below, the literature review indicates that the ideal gas law would probably have been sufficient. The Abel-Noble EOS was chosen and implemented as it was believed to make the dynamic leak flow model more versatile. In addition, the Abel-Noble EOS has been selected due to its simplicity in implementation, and it is in the literature review found to predict accurate results for problems that include hydrogen gas. However, considering the results from Case 1 and 2, it is quite clear that the ideal gas law actually would have been sufficient for this case with pressures up to 10 bar.

A 2^{nd} – order accurate FLIC scheme, centered in space and containing a flux limiter, was implemented to compute the governing equations. The FLIC scheme shows a promising behavior when studying the rarefactions waves obtained by *test 2* as described in sections 3.4.2 and 3.5.1 but might be a little more diffusive than the exact result. The simulations showed stable results with the FLIC scheme. Source terms were added to the scheme with source term splitting and the 1^{st}-order accurate Euler method. The model has mainly been validated by comparison with hand calculations, where the results indicate that the source terms seem to be implemented correctly. The model considers the effects due to friction, heat losses, and minor losses due to irregularities in the piping geometry.

Two flux-limiters, Superbee and Minbee, have been implemented in the model. The Superbee flux limiter shows oscillatory behavior when source terms are implemented in the model. With the use of Minbee, stable results have been obtained. Therefore, the Minbee flux limiter has been the preferred flux limiter for the dynamic leak flow model in this study, even though more diffusive results were expected.

Calculations of the thermal conductivity and the viscosity are performed using trendlines obtained from empirical data. This method seems to work well, and the model's estimated results are in accordance with the hand calculations.

For modeling the leakage in the dynamic leak flow model, isentropic relations have been utilized, and leak fluxes have been implemented as source terms to the governing equations. The leakage mass flow rate is estimated to become larger than the pipeline mass flow rate if the ratio between the leak orifice diameter and pipe diameter is greater than 0.2. A larger leakage mass flow rate than the inlet mass flow rate is probably possible at an initial phase when the leak occurs. The pipeline is likely to be completely filled with gas, and the escaping hydrogen can come from both downstream and upstream of the leakage orifice. Only the initial effects of the leakage have been investigated in this study.

Three different cases of simulations have been performed with the dynamic leak flow model. The first case measured the total pressure drop from the inlet to the pipeline outlet with increasing leakage orifice diameter. Results obtained by the model with 10 bar inlet pressure

indicate a significant increase in the pressure drop gradient when the leakage orifice diameter exceeds approximately 1.5 mm.

The second case was performed by investigating the pressure drop due to the rarefaction wave and change in mass flow rate at four different locations with equal spacing from the leakage point. Here the model estimates that the pressure drop is larger downstream than upstream. This effect seems to be present from very small leakage orifice diameters as it was present from a leakage orifice diameter of 0.25mm. The effect of the larger pressure drop downstream than upstream is identified in the model to be caused by the implemented source terms and is found reasonable since the pressure is already lower downstream due to the source terms.

The third case was simulated for three different leakage orifices, 0.5mm, 1.0mm, and 2.5 mm, with varying pressure from 2 – 10 bar. Similar results as with case number two are obtained. The model estimates that the difference in pressure drop due to the rarefaction wave upstream and downstream is dependent on the inlet pressure. For higher pressures, the difference is becoming more noticeable between upstream and downstream.

With that being said, the implemented dynamic leak flow model has been successfully implemented, shown stable simulations and results with the Minbee flux limiter, and seems to estimate reasonable results.

References

[1] United Nations, “Climate Change - Goal 13: Take urgent action to combat climate change and its impacts,” *United Nations Sustainable Development*. https://www.un.org/sustainabledevelopment/climate-change/ (accessed May 10, 2022).

[2] International Energy Agency, “Net Zero by 2050 – Analysis,” *IEA*, May 2021. https://iea.blob.core.windows.net/assets/deebef5d-0c34-4539-9d0c-10b13d840027/NetZeroby2050-ARoadmapfortheGlobalEnergySector_CORR.pdf (accessed May 10, 2022).

[3] DNV, “LNG as marine fuel,” *DNV*. https://www.dnv.com/maritime/insights/topics/lng-as-marine-fuel/technologies.html (accessed May 10, 2022).

[4] T. Bose, *Hydrogen: facing the energy challenges of the 21st century*. United Kingdom: John Libbey Eurotext, 2007.

[5] DNV, “Five lessons to learn on hydrogen as ship fuel,” *DNV*, Jul. 15, 2021. https://www.dnv.com/expert-story/maritime-impact/Five-lessons-to-learn-on-hydrogen-as-ship-fuel.html (accessed Apr. 26, 2022).

[6] DNV, “Handbook for Hydrogen-fuelled Vessels,” *DNV*, Jun. 2021. https://www.dnv.com/maritime/publications/handbook-for-hydrogen-fuelled-vessels-download.html (accessed May 02, 2022).

[7] International Energy Agency, “Global Hydrogen Review 2021,” *IEA*, 2021. https://www.iea.org/reports/global-hydrogen-review-2021 (accessed Apr. 26, 2022).

[8] Hydrogen Central, “LMG Marin: World’s first hydrogen-powered ferry delivered to Norwegian owner Norled,” *Hydrogen Central*, Jul. 29, 2021. https://hydrogen-central.com/lmg-marin-first-hydrogen-powered-ferry-delivered-norwegian-owner-norled/ (accessed Apr. 26, 2022).

[9] Corvus Energy, “H2NOR Fuel Cell,” *Corvus Energy*. https://corvusenergy.com/h2nor-fuel-cell/ (accessed May 11, 2022).

[10] Corvus Energy, “Corvus Energy Inherently gas safe marine fuel cell system awarded Approval in Principle by DNV,” *Corvus Energy*, Apr. 04, 2022. https://corvusenergy.com/corvus-energy-inherently-gas-safe-marine-fuel-cell-system-awarded-approval-in-principle-by-dnv/ (accessed May 19, 2022).

[11] IMO, “International Convention for the Safety of Life at Sea (SOLAS), 1974.” https://www.imo.org/en/About/Conventions/Pages/International-Convention-for-the-Safety-of-Life-at-Sea-(SOLAS),-1974.aspx (accessed May 30, 2022).

[12] HySafe, “Hydrogen Fundamentals,” *HySafe - Safety of Hydrogen as an Energy Carrier*, Jan. 30, 2007. http://www.hysafe.org/download/997/brhs_ch1_fundamentals-version%201_0_1.pdf

[13] Asia Industrial Gases Association, “HYDROGEN PIPELINE SYSTEMS - AIGA 033/14.” 3 HarbourFront Place, #09-04 HarbourFront Tower 2, Singapore 099254, 2014. [Online]. Available: https://www.asiaiga.org/uploaded_docs/AIGA%20033_14%20Hydrogen%20pipeline%20systems.pdf

[14] DNV GL, “Making LPG fuel an option for the shipping industry - DNV,” *DNV GL*, Oct. 30, 2020. https://www.dnv.com/expert-story/maritime-impact/Making-LPG-fuel-an-option-for-the-shipping-industry.html (accessed May 10, 2022).

[15] DNV GL - Maritime, “Assessment of selected alternative fuels and technologies in shipping.” Jun. 2019. Accessed: May 10, 2022. [Online]. Available: https://www.dnv.com/maritime/publications/alternative-fuel-assessment-download.html

[16] X. Gu, G. Jiang, Z. Guo, and S. Ding, “Design and Experiment of Low-Pressure Gas Supply System for Dual Fuel Engine,” *Pol. Marit. Res.*, vol. 27, no. 2, pp. 76–84, Jun. 2020, doi: 10.2478/pomr-2020-0029.

[17] A. R. Nerheim, V. Æsøy, and F. T. Holmeset, “Hydrogen as a Maritime Fuel–Can Experiences with LNG Be Transferred to Hydrogen Systems?,” *J. Mar. Sci. Eng.*, vol. 9, no. 7, p. 743, Jul. 2021, doi: 10.3390/jmse9070743.

[18] M. Chorowski, P. Duda, J. Polinski, and J. Skrzypacz, “LNG systems for natural gas propelled ships,” *IOP Conf. Ser. Mater. Sci. Eng.*, vol. 101, p. 012089, Dec. 2015, doi: 10.1088/1757-899X/101/1/012089.

[19] S. Chakraborty, “Understanding The Design of Liquefied Gas Carriers,” *Marine Insight*, Sep. 21, 2019. https://www.marineinsight.com/naval-architecture/understanding-design-liquefied-gas-carriers/ (accessed May 30, 2022).

[20] I. Makarova, K. Shubenkova, and G. Sadygova, “Compressed natural gas as motor fuel: possibilities, problems and solutions,” *Arch. Motoryz.*, vol. 82, no. 4, pp. 43–62, Dec. 2018, doi: 10.14669/AM.VOL82.ART4.

[21] IEA Technology Collaboration Programme, “Hydrogen as fuel for fuel cell electric vehicles,” *Hydrogen as fuel*. https://www.ieafuelcell.com/index.php?id=33 (accessed May 10, 2022).

[22] Energy Observer, “About Energy Observer,” *Energy Observer*. https://www.energy-observer.org/about/story (accessed May 10, 2022).

[23] H. Xing, C. Stuart, S. Spence, and H. Chen, “Fuel Cell Power Systems for Maritime Applications: Progress and Perspectives,” *Sustainability*, vol. 13, no. 3, p. 1213, Jan. 2021, doi: 10.3390/su13031213.

[24] L. van Biert, M. Godjevac, K. Visser, and P. V. Aravind, “A review of fuel cell systems for maritime applications,” *J. Power Sources*, vol. 327, pp. 345–364, Sep. 2016, doi: 10.1016/j.jpowsour.2016.07.007.

[25] Matmatch, “Yield Strength vs. Tensile Strength - What’s the Difference? - Matmatch.” https://matmatch.com/learn/property/difference-between-yield-strength-tensile-strength (accessed May 03, 2022).

[26] Bureau Veritas, “Gas Fueled Ships - NR529 (IGF - Code).” Bureau Veritas, Jan. 2020. [Online]. Available: https://marine-offshore.bureauveritas.com/rule-notes-and-guidance-notes

[27] Hydrogen Tools, “Hydrogen Embrittlement.” https://h2tools.org/bestpractices/hydrogen-embrittlement (accessed May 24, 2022).

[28] Petrol Plaza, “Double-walled pipe system, double security in your facilities,” Feb. 17, 2021. https://www.petrolplaza.com/news/26627 (accessed May 05, 2022).

[29] The American Society of Mechanical Engineers, “ASME B31.12-2011 - Hydrogen Piping and Pipelines.” ASME International, 2011. [Online]. Available: https://poltar.jlab.org/filedir/Procedures/ASME%20B31.12.pdf

[30] Office of Energy Efficiency & Renewable Energy, “Hydrogen Pipelines,” *Energy.gov*. https://www.energy.gov/eere/fuelcells/hydrogen-pipelines (accessed May 03, 2022).

[31] DNV, “DNV rules and standards,” *Rules and standards*. https://rules.dnv.com/ServiceDocuments/dnv/?_ga=2.179523620.1817100458.1651134014-283718280.1651045993#!/industry/1/Maritime/1/Rules%20for%20classification:%20Ships%20(RU-SHIP) (accessed Apr. 28, 2022).

[32] Engineering ToolBox, “ASME/ANSI B36.10/19 - Carbon, Alloy and Stainless Steel Pipes - Dimensions - Metric Units,” *ASME/ANSI B36.10/19 - Carbon, Alloy and Stainless Steel Pipes - Dimensions - Metric Units*, 2003. https://www.engineeringtoolbox.com/asme-steel-pipes-sizes-d_42.html (accessed May 03, 2022).

[33] Reliable Pipes & Tubes LTD, “Stainless Steel Pipe Bends, SS Long Radius bend, SS Piggable Bend,” *Reliable Pipes & Tubes LTD - Pipe/Tube manufacturer & Exporter*. https://www.reliablepipestubesltd.com/stainless-steel-pipe-bends-long-radius-piggable-bend.html#type13 (accessed May 05, 2022).

[34] Budenberg, “What is a Double Block and Bleed Valve?,” Dec. 15, 2020. https://www.budenberg.co.uk/blog/what-is-a-double-block-and-bleed-valve (accessed May 04, 2022).

[35] J. M. Smith, H. C. Van Ness, M. M. Abott, and M. T. Swihart, *Introduction to chemical engineering thermodynamics.* Place of publication not identified: MCGRAW-HILL, 2017.

[36] R. Khaksarfard, M. R. Kameshki, and M. Paraschivoiu, “Numerical simulation of high pressure release and dispersion of hydrogen into air with real gas model,” *Shock Waves*, vol. 20, no. 3, pp. 205–216, Jun. 2010, doi: 10.1007/s00193-010-0260-4.

[37] R. Smith and P. of P. R. Smith, *Chemical Process: Design and Integration*. Hoboken: John Wiley & Sons, Incorporated, 2005.

[38] J. F. Helgaker, *Modeling Transient Flow in Long Distance Offshore Natural Gas Pipelines*. Norges teknisk-naturvitenskapelige universitet, Fakultet for ingeniørvitenskap og teknologi, Institutt for energi- og prosessteknikk, 2013. Accessed: Jan. 24, 2022. [Online]. Available: https://ntnuopen.ntnu.no/ntnu-xmlui/handle/11250/235408

[39] Q. Zou, Y. Tian, and F. Han, “Prediction of state property during hydrogen leaks from high-pressure hydrogen storage systems,” *Int. J. Hydrog. Energy*, vol. 44, no. 39, pp. 22394–22404, Aug. 2019, doi: 10.1016/j.ijhydene.2019.06.126.

[40] E. F. Toro, *Riemann solvers and numerical methods for fluid dynamics: a practical introduction*, 3rd ed. Dordrecht ; New York: Springer, 2009.

[41] C. S. Marchi, B. P. Somerday, and S. L. Robinson, “Permeability, solubility and diffusivity of hydrogen isotopes in stainless steels at high gas pressures,” *Int. J. Hydrog. Energy*, vol. 32, no. 1, pp. 100–116, Jan. 2007, doi: 10.1016/j.ijhydene.2006.05.008.

[42] M. Chaczykowski, “Transient flow in natural gas pipeline – The effect of pipeline thermal model,” *Appl. Math. Model.*, vol. 34, no. 4, pp. 1051–1067, Apr. 2010, doi: 10.1016/j.apm.2009.07.017.

[43] X. Zhou, K. Li, R. Tu, J. Yi, Q. Xie, and X. Jiang, “A modelling study of the multiphase leakage flow from pressurised CO 2 pipeline,” *J. Hazard. Mater.*, vol. 306, pp. 286–294, Apr. 2016, doi: 10.1016/j.jhazmat.2015.12.026.

[44] S. J. Alesaadi and F. Sabzi, “Hydrogen storage in a series of Zn-based MOFs studied by Sanchez–Lacombe equation of state,” *Int. J. Hydrog. Energy*, vol. 40, no. 4, pp. 1651–1656, Jan. 2015, doi: 10.1016/j.ijhydene.2014.12.008.

[45] S. Bai-gang, Z. Dong-sheng, and L. Fu-shui, “A new equation of state for hydrogen gas,” *Int. J. Hydrog. Energy*, vol. 37, no. 1, pp. 932–935, Jan. 2012, doi: 10.1016/j.ijhydene.2011.03.157.

[46] E. W. Lemmon, M. L. Huber, and J. W. Leachman, “Revised Standardized Equation for Hydrogen Gas Densities for Fuel Consumption Applications,” *J. Res. Natl. Inst. Stand. Technol.*, vol. 113, no. 6, p. 341, Nov. 2008, doi: 10.6028/jres.113.028.

[47] T. Kim, Y. Kim, and S.-K. Kim, “Real-fluid flamelet modeling for gaseous hydrogen/cryogenic liquid oxygen jet flames at supercritical pressure,” *J. Supercrit. Fluids*, vol. 58, no. 2, pp. 254–262, Sep. 2011, doi: 10.1016/j.supflu.2011.05.020.

[48] H. Henrie, *Pipeline leak detection handbook*, 1st edition. Cambridge, MA: Elsevier, 2016.

[49] R. Alamian, M. Behbahani-Nejad, and A. Ghanbarzadeh, “A state space model for transient flow simulation in natural gas pipelines,” *J. Nat. Gas Sci. Eng.*, vol. 9, pp. 51–59, Nov. 2012, doi: 10.1016/j.jngse.2012.05.013.

[50] N. Crawford, “Pressure Losses at Bends and Junctions,” Doctor of Philosophy, Queen’s University, Belfast, 2005. [Online]. Available: https://pure.qub.ac.uk/en/studentTheses/pressure-losses-at-bends-and-junctions

[51] D. Brkić, “Review of explicit approximations to the Colebrook relation for flow friction,” *J. Pet. Sci. Eng.*, vol. 77, no. 1, pp. 34–48, Apr. 2011, doi: 10.1016/j.petrol.2011.02.006.

[52] F. A. Holland, *Fluid flow for chemical engineers*, 2nd ed. London: Edward Arnold, 1995.

[53] M. Olia, *Fe fundamentals of engineering exam*. Boston, Massachsetts: Barrons Educational Series, Inc, 2015.

[54] L. Zeghadnia, J. L. Robert, and B. Achour, “Explicit solutions for turbulent flow friction factor: A review, assessment and approaches classification,” *Ain Shams Eng. J.*, vol. 10, no. 1, pp. 243–252, Mar. 2019, doi: 10.1016/j.asej.2018.10.007.

[55] H. K. Winning and T. Coole, “Explicit Friction Factor Accuracy and Computational Efficiency for Turbulent Flow in Pipes,” *Flow Turbul. Combust.*, vol. 90, no. 1, pp. 1–27, Jan. 2013, doi: 10.1007/s10494-012-9419-7.

[56] Z. Yufeng, Z. Guobing, X. Hui, and C. Jing, “An assessment of friction factor and viscosity correlations for model prediction of refrigerant flow in capillary tubes,” *Int. J. Energy Res.*, vol. 29, no. 3, pp. 233–248, 2005, doi: 10.1002/er.1050.

[57] M. Fowler, “Gas Viscosity,” Jun. 26, 2007. https://galileo.phys.virginia.edu/classes/152.mf1i.spring02/Viscosity.pdf (accessed May 30, 2022).

[58] L. I. Langelandsvik, “Modeling of natural gas transport and friction factor for large-scale pipelines,” p. 209.

[59] A. L. Lee, M. H. Gonzalez, and B. E. Eakin, “The Viscosity of Natural Gases,” *J. Pet. Technol.*, vol. 18, no. 08, pp. 997–1000, Aug. 1966, doi: 10.2118/1340-PA.

[60] T. L. Bergman, A. S. Lavine, F. P. Incropera, and D. P. DeWitt, *Incropera’s principles of heat and mass transfer*, 8th edition, Global edition. Hoboken, NJ: Wiley, 2017.

[61] T. Berstad *et al.*, “CO2 pipeline integrity: A new evaluation methodology,” *Energy Procedia*, vol. 4, pp. 3000–3007, Jan. 2011, doi: 10.1016/j.egypro.2011.02.210.

[62] R. J. LeVeque, *Finite volume methods for hyperbolic problems*. Cambridge; New York: Cambridge University Press, 2002. Accessed: May 11, 2022. [Online]. Available: http://www.vlebooks.com/vleweb/product/openreader?id=Edinburgh&isbn=9780511323638

[63] L. R. Hellevik, “Numerical Methods for Engineers,” Jan. 13, 2020. https://folk.ntnu.no/leifh/teaching/tkt4140/._main072.html (accessed Apr. 24, 2022).

[64] D. Liang, A. G. L. Borthwick, and J. K. Romer-Lee, “Run-Up of Solitary Waves on Twin Conical Islands Using a Boussinesq Model,” *J. Offshore Mech. Arct. Eng.*, vol. 134, no. 1, p. 011102, Feb. 2012, doi: 10.1115/1.4003394.

[65] P. K. W. Welahettige, *Transient drilling fluid flow in Venturi channels: comparing 3D and 1D models to experimental data*. University of South-Eastern Norway, 2019. Accessed: Apr. 25, 2022. [Online]. Available: https://openarchive.usn.no/usn-xmlui/handle/11250/2623108

[66] Hydrogen Tools, “Hydrogen Properties.” https://h2tools.org/hyarc/hydrogen-properties (accessed Mar. 19, 2022).

[67] Engineering ToolBox, “Pipe and Tube System Components - Minor (Dynamic) Loss Coefficients,” 2004. https://www.engineeringtoolbox.com/minor-loss-coefficients-pipes-d_626.html (accessed Mar. 18, 2022).

[68] Engineering ToolBox, “Metals, Metallic Elements and Alloys - Thermal Conductivities,” 2005. https://www.engineeringtoolbox.com/thermal-conductivity-metals-d_858.html (accessed May 12, 2022).

[69] Wikipedia contributors, “Moody chart,” *Wikipedia*. Wikipedia, The Free Encyclopedia., Apr. 16, 2022. Accessed: May 14, 2022. [Online]. Available: https://en.wikipedia.org/w/index.php?title=Moody_chart&oldid=1083014650

[70] K. Vaagsaether, V. Knudsen, and D. Bjerketvedt, “Simulation of flame acceleration and DDT in H2-air mixture with a flux limiter centered method,” *Int. J. Hydrog. Energy*, vol. 32, no. 13, pp. 2186–2191, Sep. 2007, doi: 10.1016/j.ijhydene.2007.04.006.

Appendices

Appendix A - Signed task description

Appendix B - Pipe strength calculations for pipe branches and sub-branches

Appendix C - Trendlines viscosity

Appendix D - Trendlines thermal conductivity

Appendix E - Python code – dynamic leak flow model

Appendix F - Hand calculations for validation of the dynamic leak flow model

Appendix A – Signed task description

University of South-Eastern Norway

Faculty of Technology, Natural Sciences and Maritime Sciences, Campus Porsgrunn

FMH606 Master's Thesis

Title: Modelling and simulation of hydrogen flow in a maritime fuel cell system

USN supervisor: Knut Vågsæther, Andre V. Gaathaug, Prasanna Welahettige

External partner: Corvus Energy, H2NOR

Task background:
There are many initiatives to develop hydrogen for maritime fuel. Maritime hydrogen fuel system will use fuel cells for electricity production to drive electrical motors. In maritime fuel cell systems, the hydrogen storage will be placed at some distance from the fuel cells. Any change in demand from the fuel cell, or due to a leak, will cause a transient response in the hydrogen flow. The understanding of hydrogen behavior due to changes in demand or thermodynamic states are needed for improved pipe layout and for implementation of safety measures for these systems.

Task description:
The objective of this study can be divided into two parts. The first part will cover a literature review regarding maritime fuel gas systems, with a main focus on fuel storage- and supply systems, which can possibly be adopted for a maritime fuel cell system. This part will also include a suggestion of a schematic diagram for a maritime fuel cell system. The fuel cell system will be proposed for a base case vessel under construction and will mainly be limited to the fuel cell supply system.

The second part will cover the development of a one-dimensional model made for hydrogen flow in a fuel cell supply system. The model shall be transient in order to analyze the effects of a sudden change in the mass flow or due to a leak. In addition, the model should consider heat losses through the pipe. The model will be limited to consider pressurized hydrogen flow in the piping between the reduction valve after the high-pressure storage system, and until but not including the fuel cell module. If time, the model will be further developed by either implementing the storage system or the fuel cell module process.
A review of relevant Equations of State (EoS) based on the possible range of states in the system will be performed, and a suitable EoS will be implemented in the model. Simulations of various cases shall be performed, with a change of the mass flow rate or a change in the thermodynamic state.

Student category: EET, PT, IIA

Is the task suitable for online students (not present at the campus)? Yes

Practical arrangements:
A thermodynamic EOS solver for Helmholtz free energy has been developed in Matlab and can be used.
The research group of Process safety, combustion and explosions is arranging the international conference ISFEH10 in May 2022 (isfeh10.org), students may be part of the organizing team during the conference.

Supervision:
As a general rule, the student is entitled to 15-20 hours of supervision. This includes necessary time for the supervisor to prepare for supervision meetings (reading material to be discussed, etc).

Signatures:

Supervisor (date and signature):

23.05.2022

29.05.2022 Prasanna Welahettige,

Student (write clearly in all capitalized letters): STIAN VALAND

Student (date and signature): 30.01.2022

Appendix B – Pipe strength calculations for pipe branches and sub-branches

This appendix shows the calculations performed to the pipe branches and sub-branches for the required inner and outer diameter and minimum wall thickness. In addition, the selected design parameters from ASME B31.12-2011 are tabulated in table B1.2.

Required inner diameter calculations:

Equation (2.7) leads to a mass flow for the branches 1-4:

$$\dot{m}_{b1-4} = \frac{\dot{m}_{main}}{4} = \frac{0.01805\,\frac{kg}{s}}{4} = 0.004513\,\frac{kg}{s}$$

From equation (2.5), the required inner diameter for each branch is calculated:

$$D_{b1-4} = \sqrt{\frac{4 \cdot 0.004513\ kg/s \cdot 4124\ J/kgK \cdot 293.15\ K}{10 \cdot 10^5\ Pa \cdot 30\frac{m}{s} \cdot \pi}} = 0.01522\ m = 15.2\ mm$$

For the last four sub-branches leading from one branch to each fuel cell module, an equivalent procedure as above applies, resulting in:

$$\dot{m}_{sb\ 1-4} = \frac{\dot{m}_{b1-4}}{4} = \frac{0.004513\,\frac{kg}{s}}{4} = 0.001128\,\frac{kg}{s}$$

This leads to a required inner diameter for each branch of:

$$D_{sb1-4} = \sqrt{\frac{4 \cdot 0.001128\ kg/s \cdot 4124\ J/kgK \cdot 293.15\ K}{10 \cdot 10^5\ Pa \cdot 30\frac{m}{s} \cdot \pi}} = 0.007609\ m = \ 7.61\ mm$$

Table B1.1: Inner pipe dimensions for the pipe branches based on ASME/ANSI B 36.10 Welded and Seamless Wrought Steel Pipe and ASME/ANSI B36.19 Stainless Steel Pipe [29].

Section	Calculated Inner diameter (mm)	Corresponding std. pipe dimensions (inches)	Schedule	Wall thickness (mm)	Outer Diameter (mm)	Inner diameter (mm)
Branch 1-4	15.2 mm	½	Std 40	2.769	21.336	15.798
Sub-branch 1-4	7.61	1/8	10S	1.245	10.3	7.811

Table B1.2: Tabulated values from ASME B31.12-2011 [29].

Parameter	Value	Table ASME B31.12-2011
F_e	1.0	IX-3B
F_d	0.5	PL-3.7.1-1
F_M	1.0	IX-5A
F_T	1.0	PL-3.7.1-3

Table B1.3: Outer pipe dimensions for the branches based on ASME/ANSI B 36.10 Welded and Seamless Wrought Steel Pipe and ASME/ANSI B36.19 Stainless Steel Pipe [32].

Section	Outer Diameter (mm) Inner pipe	Outer diameter, outer pipe (mm)	Inner diameter, outer pipe (mm)	Schedule	Wall thickness Outer pipe (mm)	Nominal diameter, Outer pipe (inches)
Branch 1-4	21.336	33.401	30.099	5S	1.651	1
Sub-branch 1-4	10.3	21.336	18.034	5S	1.651	½

Calculations performed for the pipe branches following the ASME B31.12

Inner piping:

Minimum thickness for the inner pipe branches 1-4 (b1-4) and sub-branches 1-4 (sb1-4):

$$t_{w_{b1-4,min}} = \frac{P \cdot OD}{2 \cdot S \cdot F_d \cdot F_e \cdot F_T \cdot F_M} = \frac{1.0\ MPa \cdot 21.336mm}{2 \cdot 195\ MPa \cdot 0.5 \cdot 1.0 \cdot 1.0 \cdot 1.0} = 0.109\ \text{mm}$$

Including corrosion allowance, $t_{w_{b1-4,min}} = 0.609$ mm

$$t_{w_{sb1-4,min}} = \frac{P \cdot OD}{2 \cdot S \cdot F_d \cdot F_e \cdot F_T \cdot F_M} = \frac{1.0\ MPa \cdot 10.3\ mm}{2 \cdot 195\ MPa \cdot 0.5 \cdot 1.0 \cdot 1.0 \cdot 1.0} = 0.053\ \text{mm}$$

Including corrosion allowance, $t_{w_{sb1-4,min}} = 0.553$mm

Outer piping:

Minimum calculated thickness for the outer pipe branches:

$$t_{w_{outer,b1-4,min}} = \frac{P \cdot OD}{2 \cdot S \cdot F_d \cdot F_e \cdot F_T \cdot F_M} = \frac{1.1\ MPa \cdot 33.401\ mm}{2 \cdot 195\ MPa \cdot 0.5 \cdot 1.0 \cdot 1.0 \cdot 1.0} = 0.188\ \text{mm}$$

Including corrosion allowance, $t_{w_{outer,b1-4,min}} =$ 0.688 mm

$$t_{w_{outer,\ sb1-4,min}} = \frac{P \cdot OD}{2 \cdot S \cdot F_d \cdot F_e \cdot F_T \cdot F_M} = \frac{1.1\ MPa \cdot 21.336\ mm}{2 \cdot 195\ MPa \cdot 0.5 \cdot 1.0 \cdot 1.0 \cdot 1.0} = 0.120 \text{ mm}$$

Including corrosion allowance, $t_{w_{outer,\ sb1-4,min}} =$ 0.620 mm

Calculations performed for the pipe branches following the IGF-Code

Inner piping:

The minimum calculated theoretical thickness for the pipe branches:

$$t_{w_{0,b1-4}} = \frac{P \cdot OD}{(2.0 \cdot \sigma_s \cdot F_{eff} + P)} = \frac{1.0\ MPa \cdot 21.336\ mm}{(2.0 \cdot 108.33\ MPa + 1.0\ MPa)} = 0.098\ mm$$

$$t_{0,b1-4} = \frac{PD}{(2.0 \cdot \sigma_s \cdot F_{eff} + P)} = \frac{1.0\ MPa \cdot 10.300\ mm}{(2.0 \cdot 108.33\ MPa + 1.0\ MPa)} = 0.047\ mm$$

Calculated bend radius for the pipe branches:

$$F_{b\,b1-4} = \frac{D \cdot t_{w_0}}{2.5 \cdot r_b} = \frac{21.336\ mm \cdot 0.098\ mm}{2.5 \cdot 2 \cdot 21.336\ mm} = 0.020\ mm$$

$$F_{b\,sb1-4} = \frac{D \cdot t_{w_0}}{2.5 \cdot r_b} = \frac{10.300\ mm \cdot 0.047\ mm}{2.5 \cdot 2 \cdot 10.300\ mm} = 0.009\ mm$$

The minimum calculated thickness for the pipe branches following the IGF-Code:

$$t_{w_{b1-4,min,IGF}} = \frac{(t_{w_0} + F_b + c)}{\left(1 - \frac{F_{tol}}{100}\right)} = \frac{(0.098 + 0.020 + 0.5)}{\left(1 - \frac{12.5}{100}\right)} = 0.706\ mm$$

$$t_{w_{sub1-4,min,IGF}} = \frac{(t_{w_0} + F_b + c)}{\left(1 - \frac{F_{tol}}{100}\right)} = \frac{(0.047 + 0.009 + 0.5)}{\left(1 - \frac{12.5}{100}\right)} = 0.636\ mm$$

Outer piping:

The minimum calculated theoretical thickness for the pipe branches:

$$tw_{0,b1-4,IGF\ outer} = \frac{P \cdot OD}{(2.0 \cdot \sigma_s \cdot F_{eff} + P)} = \frac{1.1\ MPa \cdot 33.401\ mm}{(2.0 \cdot 108.33\ MPa + 1.1\ MPa)} = 0.168\ mm$$

$$tw_{0,sb1-4,IGF\ outer} = \frac{P \cdot OD}{\left(2.0 \cdot \sigma_s \cdot\ F_{eff} + P\right)} = \frac{1.1\ MPa\ \cdot 21.336\ mm}{(2.0\ \cdot 108.33\ MPa + 1.1\ MPa)} = 0.108\ mm$$

Calculated bend radius for the pipe branches:

$$F_{b\,b1-4,IGF,outer} = \frac{D \cdot t_{w0}}{2.5 \cdot r_b} = \frac{33.401\ mm \cdot 0.168\ mm}{2.5\ \cdot 2 \cdot 33.401\ mm} = 0.034\ mm$$

$$F_{b\,sb1-4,IGF,outer} = \frac{D \cdot t_{w0}}{2.5 \cdot r_b} = \frac{21.336\ mm \cdot 0.108\ mm}{2.5\ \cdot 2 \cdot 21.336\ mm} = 0.022\ mm$$

The minimum calculated thickness for the pipe branches following the IGF-Code:

$$t_{w\,b1-4,min,IGF,outer} = \frac{\left(t_{w0} + F_b + c\right)}{\left(1 - \frac{F_{tol}}{100}\right)} = \frac{(0.168 + 0.034 + 0.5)}{\left(1 - \frac{12.5}{100}\right)} = 0.803\ mm$$

$$t_{w\,sb1-4,min,IGF,outer} = \frac{\left(t_{w0} + F_b + c\right)}{\left(1 - \frac{F_{tol}}{100}\right)} = \frac{(0.108 + 0.022 + 0.5)}{\left(1 - \frac{12.5}{100}\right)} = 0.719\ mm$$

Appendix C – Trendlines viscosity

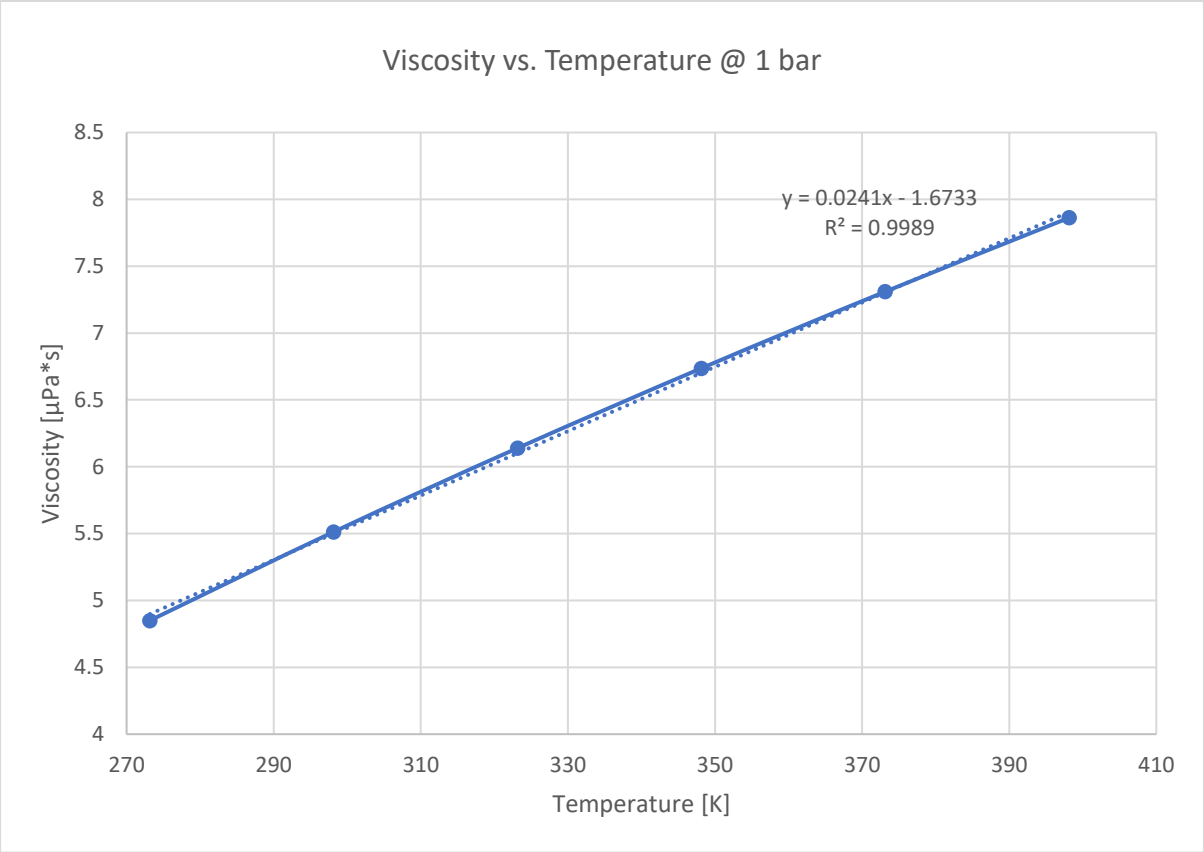

Figure 3.48: Plot of viscosity vs. temperature with trendline, based on empirical data from [64] for 1 bar.

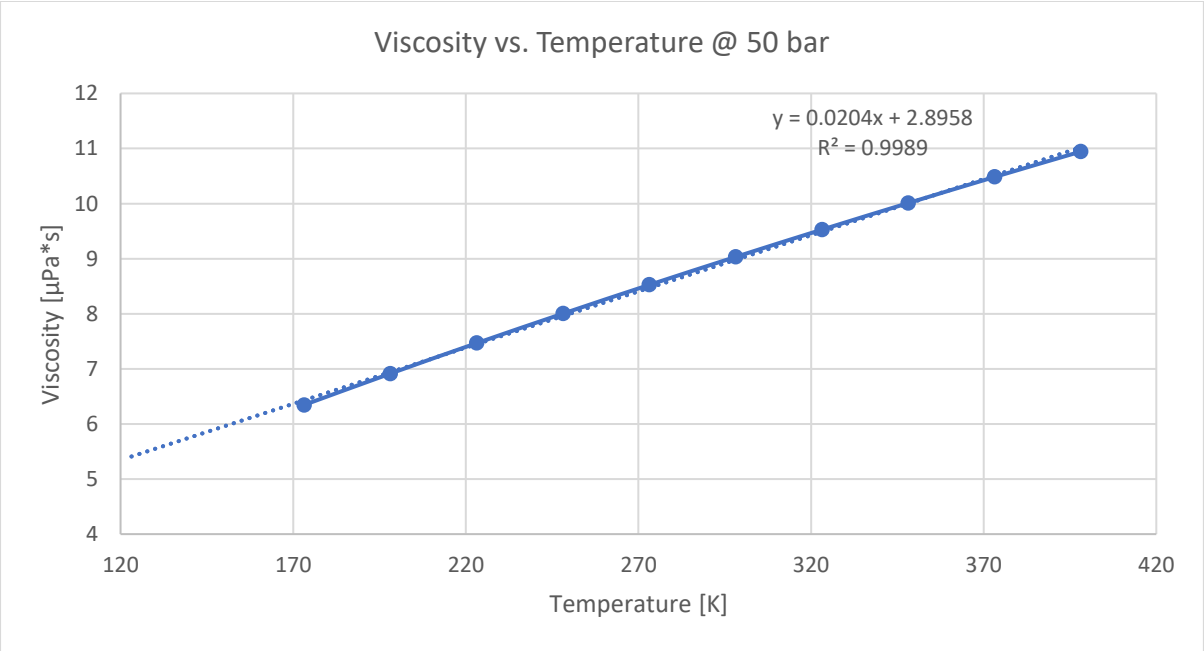

Figure 3.49: Plot of viscosity vs. temperature with trendline, based on empirical data from [64] for 50 bar.

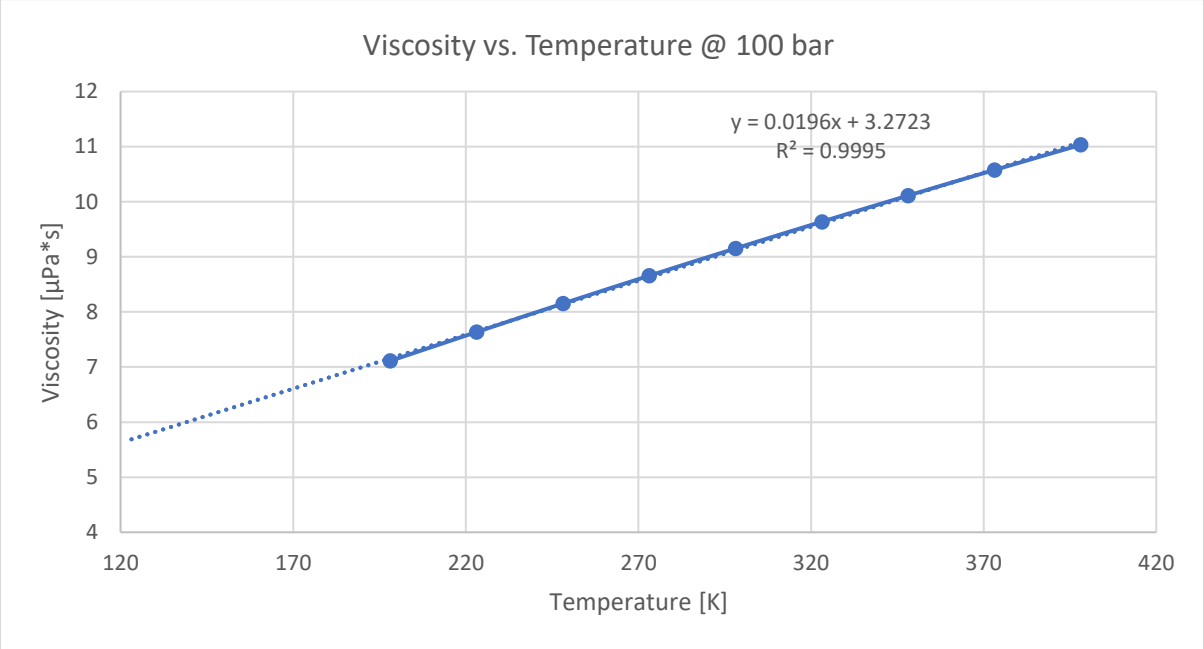

Figure 3.50: Plot of viscosity vs. temperature with trendline, based on empirical data from [64] for 100 bar.

Appendix D Trendlines for thermal conductivity

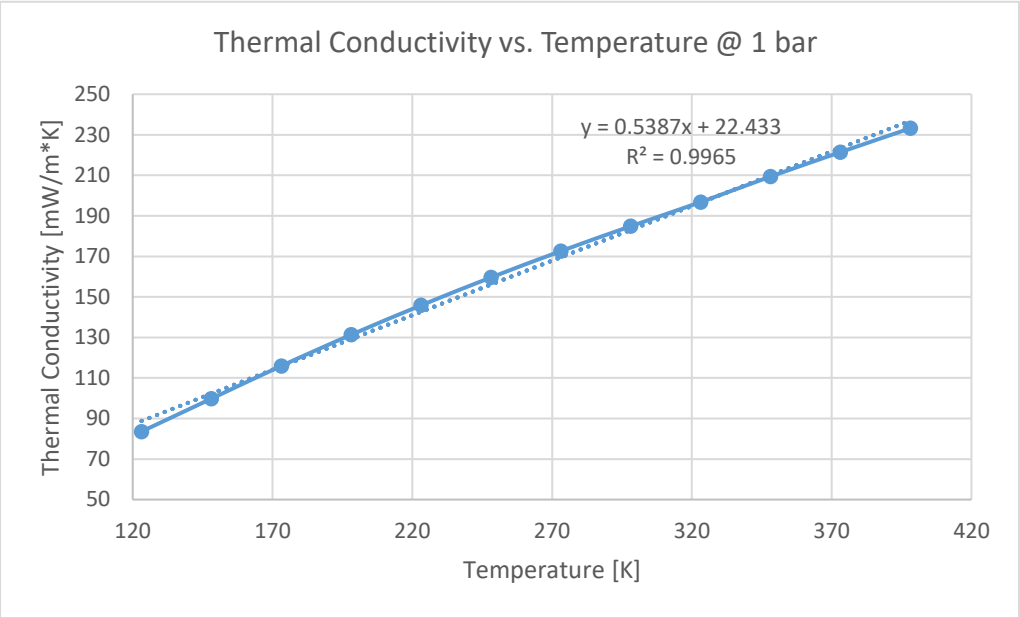

Figure 3.51: Plot of thermal conductivity vs. temperature with trendline, based on empirical data from [66] for 1 bar.

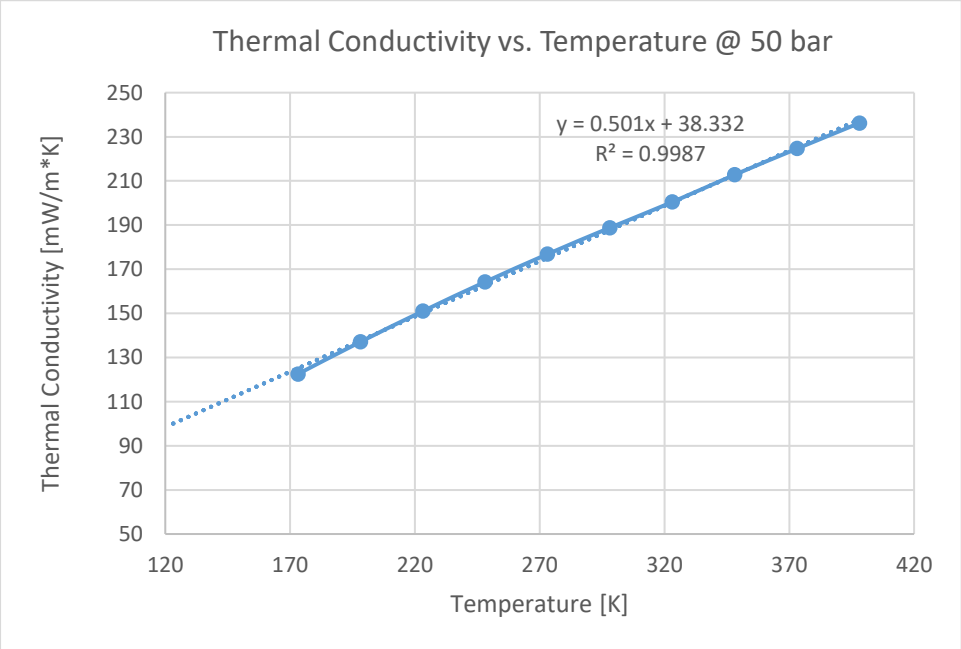

Figure 3.52: Plot of thermal conductivity vs. temperature with trendline, based on empirical data from [64] for 50 bar.

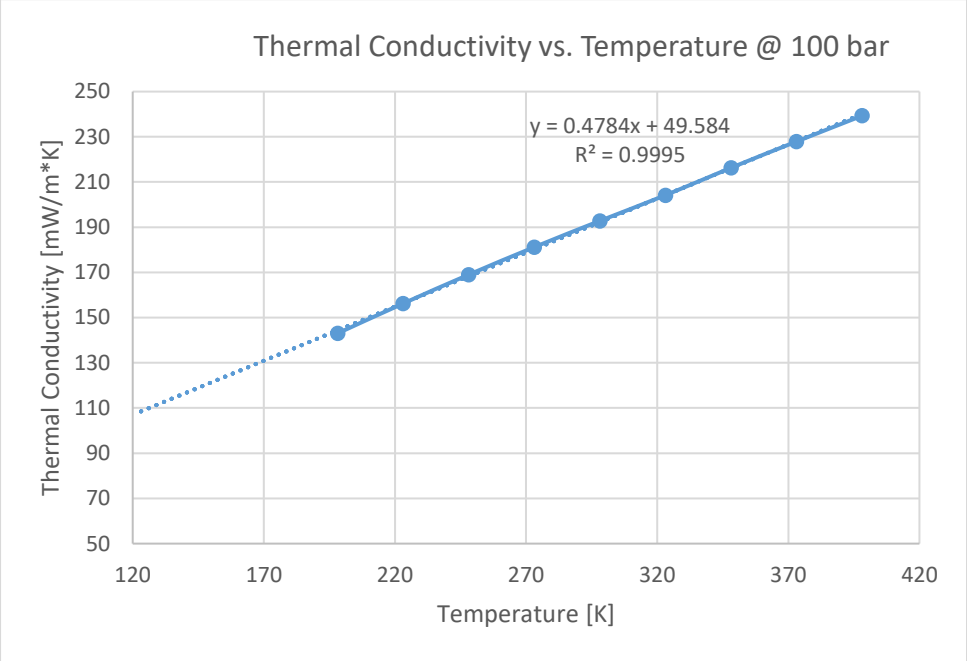

Figure 3.53: Plot of thermal conductivity vs. temperature with trendline, based on empirical data from [64] for 100 bar.

Appendix E – Python code - dynamic leak flow model

The python code is also attached electronically in a compressed file, containing the python script and two files with the steady-state initial condition values with Abel-Noble and ideal gas EOS. The steady-state files must be placed in the same folder as the python script to work and must be used if IC 4 & 5 is selected in the dynamic leak flow model.

Python Code – Dynamic leak flow model:

```
# -*- coding: utf-8 -*-
"""
Created on Mon Mar  7 11:08:29 2022

@author: Stian Valand
"""

import numpy as np
import matplotlib.pyplot as plt
import warnings as wa
import time
import pickle

wa.filterwarnings('ignore')
np.set_printoptions(suppress=True)

#%% Some parameters
x_start = 0; x_end = 45
L = x_end - x_start #Length of domain
t_start = 0; t_end = 0.01
Nx = 2000 # Number of spatial iterations
dx = ((x_end - x_start)/(Nx))  # Spatial step
x = np.linspace(x_start + dx/2, x_end, Nx+1) # For plotting

start_time = time.time()

half_way = int(Nx/2)
Nt = 13500  #Number of time-steps
leak_time = 12450 #300 Onset leakage

#%% Pipe specs.
D = 0.009 #pipe diameter
OD = 0.012 # Outer diameter
ed = (0.025*1e-3)/D #Relative roughness. Steel structural or forged
K = 0.3 # Minor loss coefficient 90deg regular elbow
N_bend = 20 #Number of bends
Kt = K/dx #(N_bend * K) # Total number of bends
A = (np.pi/4.0) * D**2 # Cross-sectional area of the pupe

Bloc = int((Nx-(2*(Nx/N_bend)))/N_bend) #Location of pipe bends.
#%% Leak specs
leak = int(Nx/2) #leak location
Do = 0.001 # Leak orifice diameter
Ao = (np.pi/4.0) * Do**2 # leak orifice area

#%% Parameters
pa = 101325 # Pa, atmospheric pressure
```

```
R = 4124.2 # universal gas constant, Hydrogen
gamma = 1.41 # Cp/Cv
b = 7.691e-3 # Abel-Noble co-volume constant [m3/kg]
CPR = ((gamma+1)/2)**(gamma / (gamma - 1.0)) # Critical pressure ratio,
in/out
k_pipe = 45 # Thermal conductivity pipeline material [W/mK]
h_air = 50 # Convective heat transfer coefficient[W/m^2*K], assumed number.
Cp = 0.0144 # Specific heat capacity [J/kg*K]
#%% Arrays
u = np.zeros(Nx+1)
p = np.zeros(Nx+1)
T = np.zeros(Nx+1)
rho = np.zeros(Nx+1)
E = np.zeros(Nx+1)
C = np.zeros(Nx+1)
Ta = np.ones(Nx+1)*293.15

lostMass = np.zeros(Nx+1)
lostMass1 = np.zeros(Nx+1)
Mdl0 = np.zeros(Nx+1)
Mdl1 = np.zeros(Nx+1)
Mdl2 = np.zeros(Nx+1)

#%% Courant-Friedrich-Lewy number
CFL = 0.87

#%% Flux limitor selector. SUPERBEE = 1, MINBEE = 2
phip = phim = 2

#%% IC selector
ic = 3        #IC 4 & 5 needs to be used together with "steady state" files
#%% Initial Conditions
if ic == 1: # Test 1, Sod's problem

    u[:half_way] = 0.0
    rho[:half_way] = 1.0
    p[:half_way] = 1.0
    u[half_way:] = 0.0
    rho[half_way:] = 0.125
    p[half_way:] = 0.1

elif ic == 2: #Test 2

    u[:half_way] = -2.0
    rho[:half_way] = 1.0
    p[:half_way] = 0.4
    u[half_way:] = 2.0
    rho[half_way:] = 1.0
    p[half_way:] = 0.4

elif ic == 3: # Initial conditions

    u[:] = 30 #[m/s]
    rho[:] = 0.822 #[kg/m3]
    p[:] = 10e5 #[Pa]
```

```
elif ic == 4: # Abel-Noble EOS. Must be used with the file "steady".
    Steady = pickle.load(open('steady', 'rb'))
    u[:] = Steady[0]
    rho[:] = Steady[1]
    p[:] = Steady[2]

elif ic == 5: # Ideal gas EOS. Must be used with the file
"steady_Ideal_Gas".
    Steady_IG = pickle.load(open('steady_Ideal_Gas', 'rb'))
    u[:] = Steady_IG[0]
    rho[:] = Steady_IG[1]
    p[:] = Steady_IG[2]


#%% Some initial conditions
# Total energy
if ic == 4:

    E = Steady[3]

elif ic == 5:
    E = Steady_IG[3]
    b = 0

else:
    E = p*(1-b*rho)/(gamma-1) + 0.5 * u**2 * rho

# Temperature

T = (p*(1-(b*rho)))/(R * rho)

#Speed of sound
C = ((gamma * p) / ((1.0 - b*rho)*rho))**0.5

# Mass flow rate [kg/s]
m_dot = rho * u * A

#%% Some isentropic relations
# Sonic Relations

rhoe = rho * (2.0/(gamma +1)) ** (1.0/(gamma - 1.0))
pe = p * (2.0 / (gamma + 1.0))**(gamma / (gamma - 1.0))
ue = C * ((2.0 / (gamma + 1))**0.5)
Ee = pe/(gamma-1) + 0.5 * (ue**2) * rhoe

massLeak1 =  ( rhoe * ue * (Do/D)**2)/dx

impLeak1 = ( u * massLeak1)

enerLeak1 = ( Ee + pe) * massLeak1 /rhoe
massOut1 = rhoe * ue * Ao

# Subsonic relations
rhoSub = ((pa/p)**(1.0/gamma)) * rho
```

```
uSub = C * ( (2.0 / (gamma - 1.0) ) * \
            (((pa / p)**((gamma - 1) / gamma))-1))**0.5

ESub = (pa/(gamma - 1)) + 0.5 * rhoSub * uSub**2


massLeak2 =  (( rhoSub * uSub )*(Do/D)**2)/dx

impLeak2 = (u * massLeak2)

enerLeak2 = (ESub + pa) * massLeak2/rhoSub
massOut2 = rhoSub * uSub * Ao

#%% Timestep
dt = (CFL*dx)/(max(abs(u)+C))


#%% Linear interpolation for the viscosity calculation
def lin_interpol(y1, y2, x_r, x1, x2):
    y = np.zeros(Nx+1)
    y = ((y2-y1)/((x2-x1))*(x_r-x1))+y1

    return y

#%% Friction factor, viscosity and Reynoldsnumber calculation:
def friction(eD, rho, u, D, T, p):

    #Churchills correlation for friction factor. Valid for all numbers of
Re.
    #Dynamic viscosity (Mu) from empirical data, @ 1, 10, 50 and 100 bar.
    #Linear interpolation between the pressures.

    Mu1 = ((0.0217 * T) + 2.2396)*1e-6 # 1 bar
    Mu10 = ((0.0216 * T) + 2.4289)*1e-6 # 10 bar
    Mu50 = ((0.0204 * T) + 2.8958)*1e-6 # 50 bar
    Mu100 = ((0.0196 * T) + 3.2723)*1e-6 # 100 bar


    p1 = np.select([(p >= 1e5) & (p < 10e5) , (p >= 10e5) & (p < 50e5),\
                    (p >= 50e5) & (p < 100e5)], [1e5, 10e5, 50e5])

    p2 = np.select([(p >= 1e5) & (p < 10e5) , (p >= 10e5) & (p < 50e5),\
                    (p >= 50e5) & (p < 100e5)], [10e5, 50e5, 100e5])

    Mu11 = np.select([(p >= 1e5) & (p < 10e5) , (p >= 10e5) & (p < 50e5),\
                      (p >= 50e5) & (p < 100e5)], [Mu1, Mu10, Mu50])

    Mu22 = np.select([(p >= 1e5) & (p < 10e5) , (p >= 10e5) & (p < 50e5),\
                      (p >= 50e5) & (p < 100e5)], [Mu10, Mu50, Mu100])

    Mu = np.select([p < 1e5, p >= 100e5], [Mu1, Mu100],\
                   default = lin_interpol(Mu11, Mu22, p, p1, p2))

    #Reynolds number
    Re = (rho*abs(u)*D)/(Mu)
```

```
    #Churchills correlation:

    Ac = (2.457 * np.log(1.0/((ed*0.27)  + (7.0/Re)**0.9)))**16.0

    Bc = (37530.0 / Re)**16.0

    f = 8.0*(((8.0/Re)**12.0) +(Ac + Bc)**(-1.5))**(1.0/12.0)

    f[Re <= 100.0] = 0.6

    return(f, Re, Mu) #Darcy friction factor, Reynolds number,Dynamic
Viscosity

#%% Thermal conductivity of Hydrogen
def thermalcondH2(T, p):
    k1 = ((0.5387 * T) + 22.433)*1e-3 # 1 bar
    k10 = ((0.5352 * T) + 24.298)*1e-3 # 10 bar
    k50 = ((0.501 * T) + 38.332)*1e-3 # 50 bar
    k100 = ((0.4784 * T) + 49.584)*1e-3 # 100 bar

    p1 = np.select([(p >= 1e5) & (p < 10e5) , (p >= 10e5) & (p < 50e5),\
                    (p >= 50e5) & (p < 100e5)], [1e5, 10e5, 50e5])

    p2 = np.select([(p >= 1e5) & (p < 10e5) , (p >= 10e5) & (p < 50e5),\
                    (p >= 50e5) & (p < 100e5)], [10e5, 50e5, 100e5])

    k11 = np.select([(p >= 1e5) & (p < 10e5) , (p >= 10e5) & (p < 50e5), \
                     (p >= 50e5) & (p < 100e5)], [k1, k10, k50])

    k22 = np.select([(p >= 1e5) & (p < 10e5) , (p >= 10e5) & (p < 50e5),\
                     (p >= 50e5) & (p < 100e5)], [k10, k50, k100])

    k = np.select([p < 1e5, p >= 100e5], [k1, k100], \
                  default = lin_interpol(k11, k22, p, p1, p2))

    return(k)

#%% Heat transfer
def heatSource(Re, T, p, Ta, L, k_pipe, h_air, Cp, Mu, D, OD):
    r1 = D / 2
    r2 = OD / 2

    kH2 = thermalcondH2(T , p)

    n = np.select([T <= Ta, T > Ta], [0.3, 0.4])
    Pr = Mu * Cp / kH2
    Nu = 0.023 * (Re**0.8) * Pr**n #Dittus - Boelter correlation

    h_gw = Nu * kH2/L

    U = ((1.0 / h_gw) + (r1 * (np.log(r2 / r1)) / k_pipe)\
         + ((r1 /(r2 * h_air)) ))**-1

    q = (U * (T - Ta))
```

```
    return(q)

#%% LAX Wendroff finite difference scheme

def LaxFlux(dt, dx, rho, u,E, p, CFL, f, gamma, C1_fric,\
            C1_minor, C2_heat, C2_fricWork,\
            b, T, phip, phim, Mdl0, Mdl1, Mdl2, \
            massLeak1, enerLeak1, impLeak1, massLeak2,\
                enerLeak2, impLeak2, Do, A, pe, pa, rhoe,\
                Ee, R, ue, m_dot, Ao, massOut1, massOut2, rhoSub, uSub,
ESub):

    A0 = (rho)
    A1 = (rho*u)
    A2 = (E)

    #Fluxes, plus(p) and minus(m)

    B0 = (rho*u)
    B1 = (p + (rho*u**2))
    B2 = ((E + p)*u)

 #%% Richtmeyer
    # Half step Richtmeyer
    A0_RI_plus = 0.5*(A0[2:] + A0[1:-1]) - 0.5*(dt/dx)*(B0[2:] - B0[1:-1])
    A1_RI_plus = 0.5*(A1[2:] + A1[1:-1]) - 0.5*(dt/dx)*(B1[2:] - B1[1:-1])
    A2_RI_plus = 0.5*(A2[2:] + A2[1:-1]) - 0.5*(dt/dx)*(B2[2:] - B2[1:-1])

    A0_RI_minus = 0.5*(A0[1:-1] + A0[:-2]) - 0.5*(dt/dx)*(B0[1:-1] - B0[:-
2])
    A1_RI_minus = 0.5*(A1[1:-1] + A1[:-2]) - 0.5*(dt/dx)*(B1[1:-1] - B1[:-
2])
    A2_RI_minus = 0.5*(A2[1:-1] + A2[:-2]) - 0.5*(dt/dx)*(B2[1:-1] - B2[:-
2])

    # Compute variables for next step

    # PLus variables Richtmeyer

    rho_pR = A0_RI_plus
    u_pR = A1_RI_plus/rho_pR
    E_pR = A2_RI_plus
    p_pR = ((gamma - 1) * (E_pR - (0.5 * rho_pR * u_pR**2)))/(1-b*rho_pR)

    #Minus variables Richtmeyer
    rho_mR = A0_RI_minus
    u_mR = A1_RI_minus/rho_mR
    E_mR = A2_RI_minus
    p_mR = ((gamma - 1) * (E_mR - (0.5 * rho_mR * u_mR**2)))/(1-b*rho_mR)

    # Compute 1/2 step Richtmeyer fluxes
    B0_RI_plus = (rho_pR * u_pR)
    B1_RI_plus = (p_pR + (rho_pR * u_pR**2))
    B2_RI_plus = ((E_pR + p_pR) * u_pR)
```

```
    B0_RI_minus = (rho_mR* u_mR)
    B1_RI_minus = (p_mR + (rho_mR * u_mR**2))
    B2_RI_minus = ((E_mR + p_mR) * u_mR)

    #%% Lax-Friedrich (LF) Fluxes

    # Compute LF fluxes
    B0_LF_plus = 0.5*(B0[2:] + B0[1:-1]) - 0.5*(dx/dt)*(A0[2:] - A0[1:-1])
    B1_LF_plus = 0.5*(B1[2:] + B1[1:-1]) - 0.5*(dx/dt)*(A1[2:] - A1[1:-1])
    B2_LF_plus = 0.5*(B2[2:] + B2[1:-1]) - 0.5*(dx/dt)*(A2[2:] - A2[1:-1])

    B0_LF_minus = 0.5*(B0[1:-1] + B0[:-2]) - 0.5*(dx/dt)*(A0[1:-1] - A0[:-
2])
    B1_LF_minus = 0.5*(B1[1:-1] + B1[:-2]) - 0.5*(dx/dt)*(A1[1:-1] - A1[:-
2])
    B2_LF_minus = 0.5*(B2[1:-1] + B2[:-2]) - 0.5*(dx/dt)*(A2[1:-1] - A2[:-
2])

    #%% Force fluxes

    #Force Plus
    B0_FORCE_plus = 0.5 * (B0_RI_plus + B0_LF_plus)
    B1_FORCE_plus = 0.5 * (B1_RI_plus + B1_LF_plus)
    B2_FORCE_plus = 0.5 * (B2_RI_plus + B2_LF_plus)

    #Force minus
    B0_FORCE_minus = 0.5 * (B0_RI_minus + B0_LF_minus)
    B1_FORCE_minus = 0.5 * (B1_RI_minus + B1_LF_minus)
    B2_FORCE_minus = 0.5 * (B2_RI_minus + B2_LF_minus)

    #%% Flux limiter. B_LO = B_Force. B_HI = B_RI. Using q = total energy
(E)

    q = E[1:-1]

    q_plus_1 = np.roll(q, -1)
    q_plus_2 = np.roll(q_plus_1, -1)
    q_minus_1 = np.roll(q, 1)
    q_minus_2 = np.roll(q_minus_1, 1)


    np.seterr(divide='ignore', invalid = 'ignore')

    #%% rR Plus
    rRp = (q_plus_2 - q_plus_1) / (q_plus_1 - q)
    rRp = np.nan_to_num(rRp)
    #%% rL plus
    rLp = (q - q_minus_1) / (q_plus_1 - q)
    rLp = np.nan_to_num(rLp)
    #print(rRp)
    #%% Phi LR plus
    phiLRp = np.minimum(rRp, rLp)
```

```
    phiGp = (1.0-CFL)/(1.0+CFL)

    #%% rR minus
    rRm = (q_plus_1 - q) / (q - q_minus_1)
    rRm = np.nan_to_num(rRm)

    #%% rL minus
    rLm = (q_minus_1 - q_minus_2) / (q - q_minus_1)
    rLm = np.nan_to_num(rLm)

    #%% Phi LR minus
    phiLRm = np.minimum(rRm, rLm)


    phiGm = (1.0-CFL)/(1.0+CFL)


    #%% Super-Bee

    GpS = (phiGp + (1.0-phiGp) * phiLRp )
    phiSBp = np.select([phiLRp <= 0, phiLRp <= 0.5, phiLRp<=1.0,
phiLRp>1.0],\
                        [0, 2.0*phiLRp, 1.0, np.minimum(2.0, GpS) ])


    GmS = (phiGm + (1.0-phiGm) * phiLRm )
    phiSBm = np.select([phiLRm <= 0, phiLRm <=0.5, phiLRm <=1.0, phiLRm >
1.0],\
                        [0, 2.0*phiLRm, 1.0, np.minimum(2.0, GmS)])

    #%% MINBEE
    phiMBp = np.select([phiLRp <= 0, phiLRp <= 1.0, phiLRp>1], [0, phiLRp,
1.0])

    phiMBm = np.select([phiLRm <= 0, phiLRm <= 1.0, phiLRm>1], [0, phiLRm,
1.0])

    #%% Flux limitor selection
    phiP = np.select([ phip == 1, phip == 2], [phiSBp, phiMBp])
    phiM = np.select([ phim == 1, phim == 2], [phiSBm, phiMBm])

    #%% Flux i+1/2
    B0_half_plus = B0_FORCE_plus +  phiP*(B0_RI_plus - B0_FORCE_plus)
    B1_half_plus = B1_FORCE_plus +  phiP*(B1_RI_plus - B1_FORCE_plus)
    B2_half_plus = B2_FORCE_plus + phiP*(B2_RI_plus - B2_FORCE_plus)

    #%% Flux i-1/2
    B0_half_minus = B0_FORCE_minus + phiM*(B0_RI_minus - B0_FORCE_minus)
    B1_half_minus = B1_FORCE_minus + phiM*(B1_RI_minus - B1_FORCE_minus)
    B2_half_minus = B2_FORCE_minus + phiM*(B2_RI_minus - B2_FORCE_minus)

    #%% Move one time step

    A0_new = A0[1:-1] - (dt/dx)*(B0_half_plus - B0_half_minus)
    A1_new = A1[1:-1] - (dt/dx)*(B1_half_plus - B1_half_minus)
```

```
    A2_new = A2[1:-1] - (dt/dx)*(B2_half_plus - B2_half_minus)

    #%% Source terms

    A1_new[1:-1] = A1_new[1:-1] + (dt*C1_fric[1:-1])
    A2_new[1:-1] = A2_new[1:-1] + (dt * C2_heat[1:-1]) + (dt *
C2_fricWork[1:-1])

    A1_new[[Bloc, 2*Bloc, 3*Bloc, 4*Bloc, 5*Bloc, 6*Bloc, 7*Bloc, 8*Bloc,
9*Bloc,\
            10*Bloc, 11*Bloc, 12*Bloc, 13*Bloc, 14*Bloc, 15*Bloc, 16*Bloc,
17*Bloc,\
                18*Bloc, 19*Bloc, 20*Bloc]] = \
       A1_new[[Bloc, 2*Bloc, 3*Bloc, 4*Bloc, 5*Bloc, 6*Bloc, 7*Bloc,
8*Bloc, 9*Bloc,\
               10*Bloc, 11*Bloc, 12*Bloc,\
                   13*Bloc, 14*Bloc, 15*Bloc, 16*Bloc, 17*Bloc,\
                   18*Bloc, 19*Bloc, 20*Bloc]] +\
             (dt * C1_minor)


   #%% Leakage
    A0_new[leak] = A0_new[leak] + (dt * Mdl0[leak])
    A1_new[leak] = A1_new[leak] + (dt * Mdl1[leak])
    A2_new[leak] = A2_new[leak] + (dt * Mdl2[leak])
    #%% Calculate new variables

    rho_new = A0_new
    u_new = A1_new/rho_new
    E_new = A2_new
    p_new = ((gamma - 1) * (E_new - (0.5 * rho_new * u_new**2)))/(1-
b*rho_new)
    T_new = (p_new*(1-(b*rho_new)))/(R * rho_new)

    C_new = ((gamma * p_new) / ((1.0 - b*rho_new)*rho_new))**0.5

    m_dot_new = rho_new * u_new * A

    #%% Sonic relations

    pe_new = p_new * (2.0 / (gamma + 1.0))**(gamma / (gamma - 1.0))
    rhoe_new = rho_new * (2.0/(gamma +1)) ** (1.0/(gamma - 1))

    ue_new = C_new * ((2.0 / (gamma +1))**0.5)

    Ee_new = (pe_new / (gamma -1.0)) + 0.5 * (ue_new**2) * rhoe_new

    massLeak1_new =  (( rhoe_new * ue_new )*(Do/D)**2)/dx

    impLeak1_new = (u_new * massLeak1_new)

    enerLeak1_new = ( Ee_new + pe_new) * massLeak1_new/rhoe_new

    massOut1_new = rhoe_new * ue_new * Ao
```

```
    #%% Subsonic relations
    rhoSub_new = (pa/p_new)**(1.0/gamma) * rho_new

    uSub_new = C_new * (( (2.0 / (gamma - 1.0) ) *\
                         (((pa / p_new)**((gamma - 1) / gamma))-1))**0.5)

    ESub_new = (pa/(gamma - 1)) + 0.5 * rhoSub_new * uSub_new**2

    massLeak2_new =  ( rhoSub_new * uSub_new )*((Do/D)**2)/dx

    impLeak2_new = (u_new * massLeak2_new)

    enerLeak2_new = ( ESub_new + pa) * massLeak2_new/rhoSub_new

    massOut2_new = rhoSub_new * uSub_new * Ao



    return(rho_new, u_new, E_new, p_new, C_new, T_new, m_dot_new,
massLeak1_new,\
           enerLeak1_new, impLeak1_new,\
          massLeak2_new, enerLeak2_new, impLeak2_new, pe_new, rhoe_new,
ue_new,\
              Ee_new, uSub_new, rhoSub_new, ESub_new, massOut1_new,
massOut2_new)


#%% Arrays for pressure sensors and mass flow plotting
ps1 = []
ps2 = []
ps3 = []
ps4 = []

mass1 = []
mass2 = []
mass3 = []
mass4 = []
massLekk = []
tid = []
t = 0


#%% Time loop
it = 0
for n in range(0, Nt):


    # Friction term
    (f, Re, Mu) = friction(ed, rho[1:-1], u[1:-1], D, T[1:-1], p[1:-1])

    # Determine sonic or subsonic flow at leakage point
    if  p[leak]/pa >= CPR:
        massLeak = massLeak1
        impLeak = impLeak1
        enerLeak = enerLeak1
```

```
        massOut = massOut1
    else:
        massLeak = massLeak2
        impLeak = impLeak2
        enerLeak = enerLeak2
        massOut = massOut2

    # Initiate leakage
    if n < leak_time:
        Mdl0[leak] = 0
        Mdl1[leak] = 0
        Mdl2[leak] = 0
        lostMass[leak] = 0
    else:
        Mdl0[leak] = -massLeak[leak]
        Mdl1[leak] = -impLeak[leak]
        Mdl2[leak] = -enerLeak[leak]
        lostMass[leak] = - massOut[leak]


    #print(massOut)
    #Source terms:
    C1_fric = - ((f*rho[1:-1]*abs(u[1:-1])*u[1:-1])/(2*D)) # Friction
Source term

    C1_minor = - (Kt * rho[[Bloc, 2*Bloc, 3*Bloc, 4*Bloc, 5*Bloc, 6*Bloc,\
                            7*Bloc, 8*Bloc, 9*Bloc, 10*Bloc, 11*Bloc,\
                               12*Bloc, 13*Bloc, 14*Bloc, 15*Bloc,
16*Bloc,\
                                    17*Bloc, 18*Bloc, 19*Bloc, 20*Bloc]] *
\
                  u[[Bloc, 2*Bloc, 3*Bloc, 4*Bloc, 5*Bloc, 6*Bloc, 7*Bloc,\
                     8*Bloc, 9*Bloc, 10*Bloc, 11*Bloc, 12*Bloc, 13*Bloc,\
                         14*Bloc, 15*Bloc, 16*Bloc, 17*Bloc, 18*Bloc,\
                             19*Bloc, 20*Bloc]]**2)/2.0 # Source term due
to bend

    C2_heat =  - 4*heatSource(Re, T[1:-1], p[1:-1], Ta[1:-1],\
                              L, k_pipe, h_air, Cp, Mu, D, OD)/D # Heat
transfer term

    C2_fricWork = - (2.0 * f * rho[1:-1] * abs(u[1:-1])**3) / D # Friction
work term


    # Initiate Richtmeyer/Friedrich FLIC scheme for computation of
variables
    (rho_new, u_new, E_new, p_new, C_new, T_new,\
     m_dot_new, massLeak1_new, enerLeak1_new, impLeak1_new,\
     massLeak2_new, enerLeak2_new, impLeak2_new, pe_new, rhoe_new, ue_new,
\
          Ee_new, uSub_new, rhoSub_new, ESub_new, massOut1_new, massOut2_new
)\
        = LaxFlux(dt, dx, rho, u, E, p, CFL, f, gamma, C1_fric,\
```

```
                    C1_minor, C2_heat, C2_fricWork, b, T, phip, phim, Mdl0,
Mdl1, Mdl2,\
                        massLeak1, enerLeak1,\
                            impLeak1, massLeak2, enerLeak2, impLeak2, Do, A,
pe, pa,\
                                rhoe, Ee, R, ue,\
                                    m_dot, Ao, massOut1, massOut2, rhoSub,
uSub, ESub)

    p_new[0] = p[0] # Fixed Value
    u_new[0] = u_new[1] # ZeroGradient
    rho_new[0] = rho_new[1] # ZeroGradient
    E_new[0] = E_new[1] # ZeroGradient
    T_new[0] = T[0] #Zero Gradient


    p_new[-1] = p_new[-2] #Zero Gradient
    rho_new[-1] = rho_new[-2] #ZeroGradient
    E_new[-1] = E_new[-2] #Zero Gradient
    T_new[-1] = T_new[-2] #Zero Gradient
    u_new[-1] = u[-1]  # Fixed Value


    #Update variables
    u[1:-1] = u_new
    rho[1:-1] = rho_new
    E[1:-1] = E_new
    p[1:-1] = p_new
    T[1:-1] = T_new
    C[1:-1] = C_new
    pe[1:-1] = pe_new
    rhoe[1:-1] = rhoe_new
    uSub[1:-1] = uSub_new
    Ee[1:-1] = Ee_new
    rhoSub[1:-1] = rhoSub_new
    ue[1:-1] = ue_new
    ESub[1:-1] = ESub_new
    m_dot[1:-1] = m_dot_new

    massLeak1[1:-1] = massLeak1_new
    impLeak1[1:-1] = impLeak1_new
    enerLeak1[1:-1] = enerLeak1_new
    massOut1[1:-1] = massOut1_new
    massLeak2[1:-1] = massLeak2_new
    impLeak2[1:-1] = impLeak2_new
    enerLeak2[1:-1] = enerLeak2_new
    massOut2[1:-1] = massOut2_new

    dt = (CFL*dx)/(max((abs(u[1:-1])+C[1:-1]))) #Update time step

    ps1.append(p[333])
    ps2.append(p[667])
    ps3.append(p[1334])
    ps4.append(p[1667])
```

```
    mass1.append(m_dot[333])
    mass2.append(m_dot[667])
    mass3.append(m_dot[1334])
    mass4.append(m_dot[1667])

    massLekk.append(lostMass[leak])



    if it%50 == 0:
        print (it)
       # fig,axes = plt.subplots(nrows=4, ncols=1)
       # plt.subplot(4, 1, 1)
       # plt.plot(x[1:-1], rho[1:-1], 'k-')
       # plt.ylabel('$rho$',fontsize=16)
       # plt.xlim(x_start,x_end)
       # plt.tick_params(axis='x',bottom=False,labelbottom=False)
       # plt.grid(True)

       # plt.subplot(4, 1, 2)
       # plt.plot(x[1:-1], u[1:-1], 'r-')
       # plt.ylabel('$U$',fontsize=16)
       # plt.xlim(x_start,x_end)
       # plt.tick_params(axis='x',bottom=False,labelbottom=False)
       # plt.grid(True)

       # plt.subplot(4, 1, 3)
       # plt.plot(x[1:-1], p[1:-1], 'b-')
       # plt.ylabel('$p$',fontsize=16)
       # plt.xlim(x_start,x_end)
       # plt.tick_params(axis='x',bottom=False,labelbottom=False)
       # plt.grid(True)

        #plt.subplot(4, 1, 4)
        #plt.plot(x[1:-1], E[1:-1], 'g-')
        #plt.ylabel('$E$',fontsize=16)
        #plt.grid(True)
        #plt.xlim(x_start,x_end)
        #plt.xlabel('x',fontsize=16)
        #plt.subplots_adjust(left=0.2)
        #plt.subplots_adjust(bottom=0.15)
        #plt.subplots_adjust(top=0.95)
        #plt.show()
    it = it + 1
    t = t + dt
    tid.append((t*1e3))


print('Start Leak:', tid[leak_time],'ms, and after:', leak_time,
'timesteps')
print('The simulation is finished after:',\
      tid[n], 'ms which corresponds to', n+1, 'time steps')
end_time = time.time()

plt.subplot(4, 1, 1)
```

```
plt.plot(x[1:-1], rho[1:-1], 'b-')
plt.ylabel('Density [kg/m3]')
plt.title('Flow variables 10 bar, 1.00 mm leak diameter @ 22.5 m')
plt.grid(True)
plt.tick_params(axis='x',bottom=False,labelbottom=False)
plt.xlim(x_start,x_end)

plt.subplot(4, 1, 2)
plt.plot(x[1:-1], u[1:-1], 'g-')
plt.ylabel('Velocity [m/s]')
plt.grid(True)
plt.xlim(x_start,x_end)
plt.tick_params(axis='x',bottom=False,labelbottom=False)

plt.subplot(4, 1, 3)
plt.plot(x[1:-1], p[1:-1], 'r-')
plt.ylabel('Pressure [Pa]')
plt.grid(True)
plt.xlim(x_start,x_end)
plt.tick_params(axis='x',bottom=False,labelbottom=False)

plt.subplot(4, 1, 4)
plt.plot(x[1:-1], E[1:-1], 'k-')
plt.ylabel('Total Energy [J]')
plt.grid(True)
plt.xlim(x_start,x_end)
plt.show()

#plt.xaxis.set_major_formatter(FormatStrFormatter('%.2f'))
plt.plot(tid, ps1, 'b', label = "PS1 @ 7.5m")
plt.plot(tid, ps2, 'r', label = "PS2 @ 15m")
plt.plot(tid, ps3, 'g', label = "PS3 @ 30m")
plt.plot(tid, ps4, 'k',label = "PS4 @ 37.5m")
plt.ylabel('Pressure [Pa]')
plt.xlabel('Time [ms]')
plt.legend(loc = "lower left")
plt.title(' Pressure drop, Leak: 1.00 mm,' \
          'leak location: 22.5m, leak start: t = 4.4 ms')
plt.tick_params(axis='x', which='major', labelsize=8)
plt.ticklabel_format( style = 'plain')
plt.show()

plt.plot(tid, mass1, 'b', label = "Sensor 1 @ 7.5m")
plt.plot(tid, mass2, 'r', label = "Sensor 2 @ 15m")
plt.plot(tid, mass3, 'g', label = "Sensor 3 @ 30m")
plt.plot(tid, mass4, 'k',label = "Sensor 4 @ 37.5m")
#plt.plot(tid, massLekk, 'm', label = 'Mass flow leakage')
plt.ylabel('Mass Flow [kg/s]')
plt.xlabel('Time [ms]')
plt.legend(loc = "best")
plt.title('Mass Flow, Leak: 1.00 mm, location = 22.5m, leak start: t = 4.4
ms')
plt.tick_params(axis='x', which='major', labelsize=8)
plt.ticklabel_format( style = 'plain')
plt.show()
```

```
plt.plot(tid, massLekk, 'b', label = 'Mass flow leakage')
plt.title('Mass flow leakage, Leak: 1.00 mm, leak location = 22.5m')
plt.ylabel('Mass flow [kg/s]')
plt.legend(loc = "best")
plt.xlabel('Time [ms]')
plt.ticklabel_format(style = 'plain')
plt.show()

plt.plot(tid, mass1, 'r', label = 'Mass flow @ PS1')
plt.title('Mass flow Sensor 1: 1.00 mm, leak location = 22.5m')
plt.ylabel('Mass flow [kg/s]')
plt.legend(loc = "best")
plt.xlabel('Time [ms]')
plt.ticklabel_format(style = 'plain')
plt.show()

plt.plot(tid[13000:13450], ps1[13000:13450], 'b',label = "PS1 @ 7.5m")
plt.ylabel('Pressure [Pa]')
plt.xlabel('Time [ms]')
plt.legend(loc = "lower left")
plt.title(' Pressure drop PS1, Leak: 1.00 mm,'\
          'leak location = 22.5m, leak start = 4.4 ms')
plt.ticklabel_format(style = 'plain')
plt.show()

plt.plot(tid[12750:13000], ps2[12750:13000], 'r',label = "PS2 @ 15m")
plt.ylabel('Pressure [Pa]')
plt.xlabel('Time [ms]')
plt.legend(loc = "lower left")
plt.title(' Pressure drop PS2, Leak: 1.00 mm, '\
          'leak location = 22.5m, leak start = 4.4 ms')
plt.ticklabel_format(style = 'plain')
plt.show()


plt.plot(tid[12750:13000], ps3[12750:13000], 'g',label = "PS3 @ 30m")
plt.ylabel('Pressure [Pa]')
plt.xlabel('Time [ms]')
plt.legend(loc = "lower left")
plt.title(' Pressure drop PS3, Leak: 1.00 mm,'\
          'leak location = 22.5m, leak start = 4.4 ms')
plt.ticklabel_format(style = 'plain')
plt.show()

plt.plot(tid[13000:13450], ps4[13000:13450], 'k',label = "PS4 @ 37.5m")
plt.ylabel('Pressure [Pa]')
plt.xlabel('Time [ms]')
plt.legend(loc = "lower left")
plt.title(' Pressure PS4, Leak: 1.00 mm,'\
          'leak location = 22.5m, leak start = 4.4 ms')
plt.ticklabel_format(style = 'plain')
plt.show()
```

```
print('Mass flow inlet =', mass1[1])
print('LekkasjeFlow=', (max((massLekk))- min((massLekk))))
print('Change in Mass1 =', (max(mass1[13000:13450]) -
min(mass1[13000:13450])))

print('Change in Mass2 =', (max(mass2[12750:13000]) -
min(mass2[12750:13000])))

print('Change in Mass3 =', (max(mass3[12750:13000]) -
min(mass3[12750:13000])))

print('Change in Mass4 =', (max(mass4[13000:13450]) -
min(mass4[13000:13450])))

print('Delta P, PS1 =', (max(ps1[13000:13450]) - min(ps1[13000:13450])))

print('Delta P, PS2 =', (max(ps2[12750:13000]) - min(ps2[12750:13000])))

print('Delta P, PS3 =', (max(ps3[12750:13000]) - min(ps3[12750:13000])))

print('Delta P, PS4 =', (max(ps4[13000:13450]) - min(ps4[13000:13450])))

print('Total pressure drop, inlet to outlet', (max(p) - min(p)))


#np.savetxt('leak_1mm.csv', [u, p, rho, E], delimiter=',', fmt='%s')
```

Appendices

Appendix F - Hand calculations for validation of the dynamic leak flow model

Attached electronically in a separate MS excel file.